Simulation of primary and secondary aerosols of the Mt. Pinatubo eruption 1991 and their radiative effects

Simulation von primären und sekundären Partikeln des Mt. Pinatubo Ausbruches 1991 und deren Strahlungswechselwirkung

Masterarbeit in Fach Meteorologie
von

Lisa Janina Muth

Dezember 2019

INSTITUT FÜR METEOROLOGIE UND KLIMAFORSCHUNG
KARLSRUHER INSTITUT FÜR TECHNOLOGIE (KIT)

Referent:	Prof. Dr. Kottmeier
Korreferent:	Prof. Dr. Hoose
Betreuer:	Dr. Vogel

Abstract

Major volcanic eruptions, like the Mt. Pinatubo eruption in 1991, are known to influence the Earth's atmosphere from a local to a global scale (Timmreck, 2012). This thesis analyses ash as a directly emitted aerosol, as well as secondary particle formations in terms sulfur aerosol nucleation and the aggregation of ash with the numerical model ICON-ART for a ten-day simulation of the Mt. Pinatubo eruption.

In this model setup, ash as a direct aerosol and SO_2 as a gaseous tracer are emitted. The simulation results show, that the insoluble ash falls out within 24 hours and therefore limits the time in which the mixed ash particles (ash core with sulfur cover) can form. The simulations further outline, that nucleation of sulfuric acid is dominant if there are no pre-existing particles.

Furthermore, the radiative effects of volcanic aerosols are implemented in ICON-ART. The SO_4 aerosol absorbs the terrestrial long wave and solar near infrared radiation, which causes a warming of eruption plume in the simulation. Shortwave radiation is scattered efficiently causing an increase in diffuse radiation and a reduction in the surface temperature below the eruption plume. In total, the decrease in the shortwave net flux exceeds the decrease in long wave net flux. The radiative feedback of the aerosols causes an increase of the mass weighted height of the eruption plume from up to 6 km. In higher altitudes the photolysis rate of ozone is higher, due to an increased photon flux. The increased photolysis of ozone produces more OH, which accelerates the H_2SO_4 formation and further the sulfur particle formation.

Zusammenfassung

Starke Vulkanausbrüche, wie der Mt. Pinatubo Ausbruch von 1991, beeinflussen die Erdatmosphäre von einer lokalen bis hin zu einer globalen Skala (Timmreck, 2012). In dieser Arbeit werden primäre und sekundäre Partikel des Mt. Pinatubo Ausbruches mit dem numerischen Model ICON-ART untersucht. Dazu wird eine zehntägige Simulation durchgeführt.

In der Simulation wird SO_2 als Gas und unlösliche Asche als direktes Aerosol emittiert. Die Simulation zeigt, dass die Asche innerhalb 24 Stunden nach der Eruption sedimentiert. Dies begrenzt die Bildung von gealterter Asche (Asche mit Schwefelsäurehülle). Des Weiteren wird gezeigt, dass wenn keine Asche vorhanden ist, auf der Schwefelsäure kondensieren kann, diese nukleiert und Sulfataerosle bildet.

Darüber hinaus wurde der Stahlungseffekt der vulkanischen Aerosole untersucht, dazu wurden die Strahlungseffekte der vulkanischen Aerosole in das ICON-ART Model eingebaut. Sulfataerosole absorbieren langwellige terrestrische und solare nahe Infrarot Strahlung, dies sorgt für eine Erwärmung der simulierten Eruptionsfahne. Kurzwellige Strahlung wird effektiv von den Partikeln gestreut, dies führt zu einen Temperaturrückgang am Boden. Insgesamt überwiegt der kurzwellige Effekt. Die Strahlungswechselwirkung der Eruptionsfahne führt zu einem Ansteigen der massengewichteten Höhe von bis zu 6 km. Mit der Höhe steigt die Photolyserate von Ozon, aufgrund des erhöhten Photonenfluss. Dies bedeutet, dass mehr OH produziert wird. Höhere OH Konzentrationen können mehr Schwefelsäure produzieren, die dann wiederum nukleieren kann und zu einer erhöhten Sulfatbildung führt.

Contents

List of Figures

1 Introduction

This thesis focuses on volcanic aerosols, which can cause large episodic increases of the aerosol content compared to the aerosol background concentration. More precisely, this thesis focuses at major volcanic eruptions, which are an example for natural short term climate variability. Volcanic aerosols have an impact on the atmospheric chemistry, particle formation and therefore the Earth's radiation budget, which furthermore affects the temperature and the atmosphere's dynamics (Timmreck, 2012). Besides the climate effects the emissions of volcanic ash have a more regional effect. One important aspect of volcanic ash emissions are the influence on the air traffic. One example is the eruption of Eyjafjallajökull on Iceland in April 2010, which disturbed the European air traffic and cost the aviation industry about $ 250 million per day (Gudmundsson et al., 2010). Therefore it is of great interest to have a good understanding of the particle formation, distribution and lifetime of volcanic aerosols and their radiative effects. The key aerosols of volcanic eruptions are sulfur particles, formed from the emitted sulfur dioxide and volcanic ash. Both aerosols, due to their composition and size, have very different lifetimes, dynamic and radiative effects.

The extent of the eruption also conditions the distribution and lifetime of the aerosols. The explosivity of an eruption is measured by the Volcanic Explosivity Index (VEI). The VEI takes the volume of products emitted, eruption plume height, and qualitative observations into account (Newhall and Self, 1982). The atmospheric impact of an eruption further depends on the eruption height. If SO_2 gets emitted up to the lower stratosphere the sulfur particles can form and have a lifetime of up to two years. Another important factor is the location of the volcano. The spreading of high latitude volcanic eruption plumes is in most cases limited to one hemisphere, whereas the eruption plume of a tropical volcano can spread around the entire globe. Large eruptions like the Tambora eruption in 1815, located in Indonesia (8°S, 117°O), Krakatau 1883, also located in Indonesia (7°S, 105°O) (Rampino and Self, 1982) and the Mt. Pinatubo eruption in 1991, located in the Philippines (15°S, 121°O) are famous examples for eruptions, in which the aerosol plume spread around the globe in a few weeks and affected the climate for up to two years.

The Mt. Pinatubo eruption is of particular scientific interest, since it is the first major eruption, causing climate effects, that are captured with modern instruments. First satellite evaluations of the Total Ozone Mapping Spectrometer (TOMS) where published by Bluth et al. (1992), determine 20 million tons of SO_2 emission, encircling the Earth in approximately 22 days.

Guo et al. (2004b) used satellite-based infrared remote sensing, to further show the role of ash and sulfur formation. The Advanced Very High Resolution Radiometer (AVHRR) and TIROS Operational Vertical Sounder/High Resolution Infrared Radiation Sounder/2

(TOVS/HIRS/2) sensors captured images of the first days after the eruption. These images indicate peaking ash and ice masses of 80 Mt - 50 Mt, with similar decrease rate. This further suggests that the ash and ice aggregate, which accelerates the fallout. Additionally Guo et al. (2004b) showed a correlation of the SO_4 formation and the SO_2 decrease.
The effect of the Mt. Pinatubo eruption could be measured all over the world, as shown by DeFoor et al. (1992), who published lidar observations of the Mauna Loa Observatory in Hawaii. The observations first detected the eruption plume on July first 1991, with increasing magnitude until the end of August.
The measured climate effect of the eruption also made it an interesting study for climate simulations, as done by Kirchner et al. (1999), performing a 2-year simulation ensemble with the ECHAM4 general circulation model (GCM). This study showed an increase of the lower stratosphere temperature of 4 K induced by the aerosol radiative effect, due to terrestrial and near infrared absorption. Further it shows a summer cooling of the surface air temperature as a direct effect and a winter cooling as an indirect effect caused by changes in the dynamics.
Further model studies by Niemeier et al. (2009) analysed the interaction of sulfur and fine ash and the radiative aerosol effect for different strengths and locations. This showed that there is a strong local dependency but a minor influence of the sulfur formation after a month.
The model studies accurately reflect the measurements of the Mt. Pinatubo eruption on a climate scale, which shows that the Mt. Pinatubo eruption is well studied and understood. Nevertheless, this work will focus once more on the volcanic aerosols of the eruption in 1991, since it is the largest eruption tracked with modern instruments.
With the numerical model ICON-ART it is possible to calculate secondary particles such as sulfur aerosols and aggregation of particles such as the aging of ash. This enables the analyses and comparison of simulation results the existing literature.
In this thesis, the development of the eruption plume will be analysed in a ten-day simulation to study the eruption on a more regional scale, which is something, that has not been done before in this detail.
The key questions of this thesis are:
How does radiation affect the height and temperature of the aerosol plume?
Does radiation influence the secondary particle formation and aerosol aggregation?

2 Theoretical background

2.1 Aerosol processes

Aerosols play an important role in the environmental processes, affecting the atmosphere in mainly three ways, firstly by influencing the radiative balance directly through scattering and absorbing solar and terrestrial radiation and indirectly by influencing cloud properties and formation. Secondly, aerosols effect the atmospheric chemistry by gas-particle conversion and heterogeneous chemical reactions. The third aspect is the emission and transport. This plays an important role for example with minerals like iron, that are transported to the oceans and influence marine organisms. Also, the human health is influenced by aerosols like pollen or fine particulate pollution (Orlando et al., 1999). Atmospheric

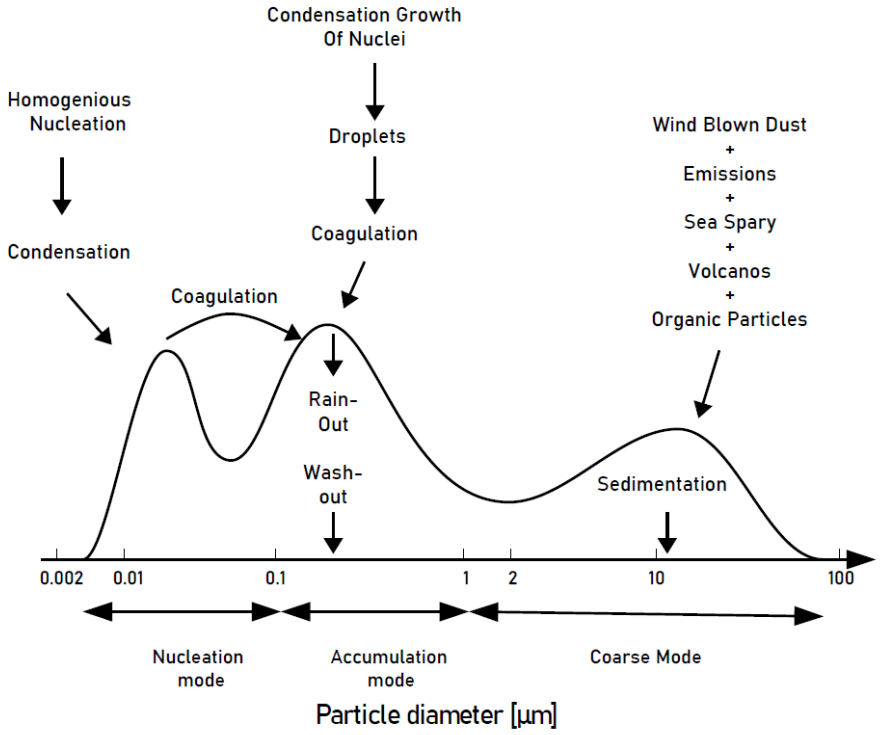

Figure 2.1: Schematic depiction of the aerosol size distribution and relevant processes. According to Orlando et al. (1999)

aerosols are characterized by different parameters such as the chemical composition, the size distribution, the morphology, as well as the phase and mixing of different phase components. All these aspects are necessary to understand the chemical and physical behavior. In general aerosols are divided in two major groups, primary and secondary aerosols. Primary aerosols are directly emitted into the atmosphere and include natural emitted

particles like sea salt, soot, pollen, mineral dust and volcanic ash. There are also anthropogenic primary emitted aerosols caused by burning processes. Secondary aerosols form in the gas phase, where nucleation, condensation, heterogeneous and multiphase chemical reactions play an important role.
Due to the different origins of the aerosols there is a wide spectrum of size distributions, which can mainly be divided in three modes as displayed in figure 2.1. The Aitken or nucleation mode describes the smallest particles formed by gas-particle conversion. Particles of the larger modes, the accumulation and coarse mode can either grow by condensation and coagulation or be primary emitted. Relevant processes in the physical description of aerosols are nucleation, condensation and evaporation, coagulation, sedimentation, wet and dry deposition, atmospheric transport and emission (Riemer, 2002), which will be discussed in the following section.
The classical homogeneous nucleation describes the formation of a cluster of molecules that must reach a certain size in order to be stable. This can occur in a supersaturated environment, the spontaneous particle formation is called homo-molecular if the particle consist of one pure substance and hetero-molecular if the particle consists of a solution. The most common example for hetero-molecular nucleation are sulfuric acid-water particles (Orlando et al., 1999).
The transition from gaseous to liquid phase on an existing particle is called condensation. A gaseous component, for example water vapor can only condensate on an existing particle if the air is supersaturated. Saturated air can reach supersaturation if there is either evaporation or sublimation of existing particles or adiabatic cooling. Different gases have different saturation pressures, H_2SO_4 is an example for a gas with a very low saturation pressure and therefore condensates fast (Orlando et al., 1999).
Coagulation labels the process of colliding particles. These collisions can be turbulent due to thermal chaotic movements or gravitational due to different sedimentation velocities. The rate of coagulation rises with the concentration, because the collisions probability is higher. Also, particles of the same size scale coagulate at smaller rates than particles of different size scales (Lee and Chen, 1984). This can be explained with the thermal coagulation function.

$$K_C = \pi(d_{p1} + d_{p2})(D_1 + D_2) \tag{2.1}$$

Where K_C is the coagulation coefficient, d_{p1}, d_{p2} are the diameter of two particles and D_1, D_2 the according diffusion coefficient. The diffusion coefficient is depending on the particle radius, with rising particle radius the diffusion coefficient declines. Therefore the particle radius and the diffusion coefficient have a negative correlation, so that the product of two different sized particles and the according diffusion coefficients will be larger than the product of a same sized particles. This also means that there is a loss of very small particles that hardly contributes to the diameter of the bigger particles, which causes a narrowing size distribution. Coagulation of particles consisting of different chemicals or phases leads to internal mixing. The change in chemistry and phase can influence the hygroscopic behavior and the optical properties (Roedel, 2013).

The removal of aerosols is divided in dry and wet deposition. Causes for dry deposition are sedimentation, due to gravitation and turbulent transport to the molecular surface layer. Wet deposition includes rain-out and wash-out. If an aerosol functions as a cloud condensation nuclei and get removed it is called rain-out. Wash-out labels the removal of the particle as it gets collected by a hydrometeor (Roedel, 2013).
Due to the different properties of the atmospheric layers, it can be divided into tropospheric and stratospheric aerosols. The troposphere reaches from the surface to about 9 km at the poles and 17 km in the tropics. It is characterized by well mixed air masses, a negative vertical temperature gradient and contains almost all atmospheric water vapor. Here the aerosols act as cloud condensation nuclei. The stratosphere reaches up to a height of about 50 km. Different to the troposphere, the stratosphere has a positive vertical temperature gradient, due to the absorption of UV light by ozone. The positive temperature gradient causes a stable layering and therefore is not well mixed. Furthermore, the stratosphere is dry. Stratospheric aerosols are mostly sulfate aerosols, built from substances emitted at the surface and transported up in the stratosphere due to long lifetimes. These aerosols form a persistent global, vertical layer, called the Junge layer.

2.2 Global sulfur cycle

Sulfur is an essential element in the Earth's chemistry and has next to numerous natural also anthropogenic sources. For the atmospheric chemistry the most important sulfur gases include dimethyl sulfide (DMS), carbonyl sulfide (OCS), hydrogen sulfide (H_2S), dimethyl disulfide (DMDS), carbon disulfide (CS_2) and sulfur dioxide (SO_2). Natural sources for DMS, OCS, H_2S, CS_2 are mainly oceans, terrestrial plants and soils and biomass burning, the biosphere and hydrosphere are also the major sinks for sulfur components. The main anthropogenic emissions are OCS due to biomass burning and SO_2 (Orlando et al., 1999).
The atmospheric sulfur chemistry is driven by oxidation of sulfur components that then form S-O bonds. The sulfur gas with the longest lifetime of about 10 years is OCS. Its reaction with OH is comparably slow, so that OCS is transported up in the stratosphere. In the stratosphere OCS further reacts to H_2SO_4 and forms sulfate aerosols and maintains the Junge layer (Orlando et al., 1999).
In the troposphere SO_2 is a common intermediate reduced sulfur component but is also emitted directly. Its oxidation can take place in the liquid and in the gas phase (reaction 2.2).

$$OH + SO_2 + M \rightarrow HOSO_2 + M \tag{2.2}$$

$$HOSO_2 + O_2 \rightarrow HO_2 + SO_3 \tag{2.3}$$

$$SO_3 + H_2O \rightarrow H_2SO_4 \tag{2.4}$$

Sulfur trioxide reacts with water either in the gas phase or in the liquid phase by uptake into a droplet (reaction 2.3). Sulfuric acid has a fairly low vapor pressure over aqueous solutions and is therefore able to condensate on existing aerosol particles or form new aerosol particles by nucleation (Orlando et al., 1999).

Compared to the troposphere the stratospheric chemistry is much more simplified, because most of the reduced gases are already removed. As mentioned only OCS is able to be transported into the stratosphere in significant amounts. In the stratosphere OCS photolysed and oxidised as followed:

$$\mathrm{OCS} + h\nu \rightarrow \mathrm{CS} + \mathrm{S} \tag{2.5}$$

$$\mathrm{O} + \mathrm{OCS} \rightarrow \mathrm{CO} + \mathrm{SO} \tag{2.6}$$

$$\mathrm{S} + \mathrm{O_2} \rightarrow \mathrm{SO} + \mathrm{O} \tag{2.7}$$

$$\mathrm{SO} + \mathrm{O_2} \rightarrow \mathrm{SO_2} + \mathrm{O} \tag{2.8}$$

$$\mathrm{SO} + \mathrm{NO_2} \rightarrow \mathrm{SO_2} + \mathrm{NO} \tag{2.9}$$

SO_2 oxidises to SO_3 and H_2SO_4 analogous to the mechanism displayed in the reactions 2.2 to 2.4 (Orlando et al., 1999) .
The vertical distribution of the H_2SO_4 concentration is determined by its rate of production and its condensation on liquid sulfate aerosols. Below around 40 km the temperatures are low enough for the H_2SO_4 to stay in the liquid phase, above 40 km the temperatures rise and H_2SO_4 is released into the gas phase. In these altitudes the oxidation of OCS decreases, which results in a peak for H_2SO_4 and therefore sulfate aerosols between 20 km and 30 km. This peak in the lower stratosphere was first discovered by Junge et al. (1961) in the 1960's and is as already mentioned named after him, the Junge layer.
Large volcanic eruptions like most recent the El Chichon (1982) and Mt. Pinatubo (1991) eruptions inject large amounts of SO_2 in the stratosphere and cause perturbations in the Junge layer, that can last for up to two years and influence the Earth's climate on a global scale due to their aerosol radiative effects, which will be discussed further on.

2.3 Volcanic aerosols

Major volcanic eruptions which are classified with the Volcanic Explosivity Index (VEI) larger than five, like the Mt. Pinatubo eruption in June 1991, inject large amounts of various gases and aerosols into the atmosphere. Important volcanic gases like sulfur dioxide (SO_2) and hydrogen sulfite (H_2S) are injected in the stratosphere, these gases oxidize as discussed, to sulfuric acid and then form sulfate aerosols. This process has and e-folding time of about a month. Other gases like carbon dioxide (CO_2) and water vapor (H_2O) play a minor role compared to their background concentrations. The amount of halogens emitted into the stratosphere is highly uncertain, but could be critical for the fate of the ozone layer after major eruptions.
Beside gases volcanic ash is emitted, that dependent on its size is removed rather quickly. Even fine ashes in general have lifetimes of a couple of weeks and therefore the effect is more regional. As displayed in figure 2.2 volcanic eruptions impact the atmosphere in different ways. There are direct effects like changes in background concentrations of gases and particles that influence chemistry, dynamic and radiative fluxes and indirect effects like Cirrus modifications and changes in precipitation.

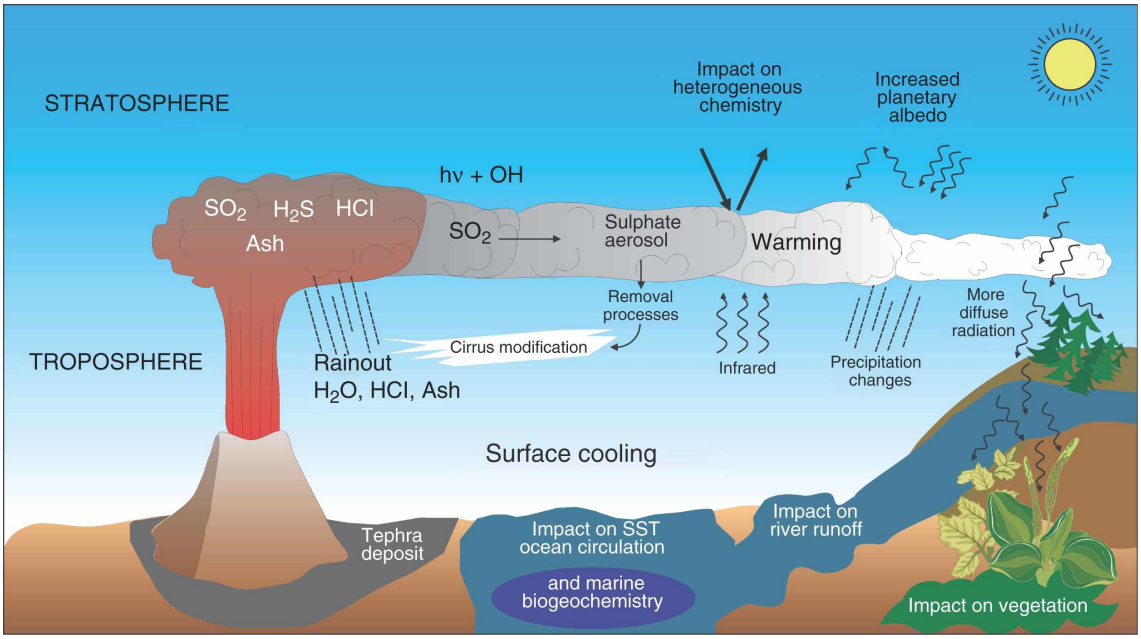

Figure 2.2: Schematic overview of the volcanic aerosol effect Timmreck (2012).

Gaseous tracers and fine ash can get injected up to the stratosphere. In the troposphere the lifetime of volcanic erupt is shorter, due to wash out. The dry and stable conditions in the stratosphere allow the formation of sulfate aerosols according to section 2.2. The perturbations in the stratospheric aerosol layer cause changes in the heterogeneous chemistry, for example, the destruction of ozone, that occurs on the surface of sulfate aerosols, similar to heterogeneous reactions taking place within polar stratospheric clouds.

2.4 Atmospheric radiation

The atmospheric radiation budget is defined by the incoming solar radiation versus the outgoing radiation. A schematic display is given in figure 2.3. Nearly one fifth of the incoming solar radiation is absorbed by the atmosphere (aerosols, gases and clouds). About one half of the solar radiation is absorbed by the Earth's surface. About a fourth of the radiation is reflected in the atmosphere and about one tenth of the radiation is reflected at the surface. In terms of long wave radiation, the terrestrial radiation from the Earth's surface is mainly absorbed and re-emitted by the atmosphere. Latent and sensible heat contribute to the Earth's energy budget as displayed in figure 2.3.

2.4.1 Aerosol interaction with radiation

Radiation can interact with the atmosphere's constituents in two ways: reflection and absorption. The fraction of reflected radiation is described by the reflectivity of the layer. The reflectivity can take values between zero (no radiation is reflected) and one (all radiation is reflected). The absorptivity is defined analogously. Transmission labels the radiation that is nigher reflected nor absorbed. The transmissivity can also take values between zero and one. The sum of reflectivity, absorptivity and transmissivity equals one.

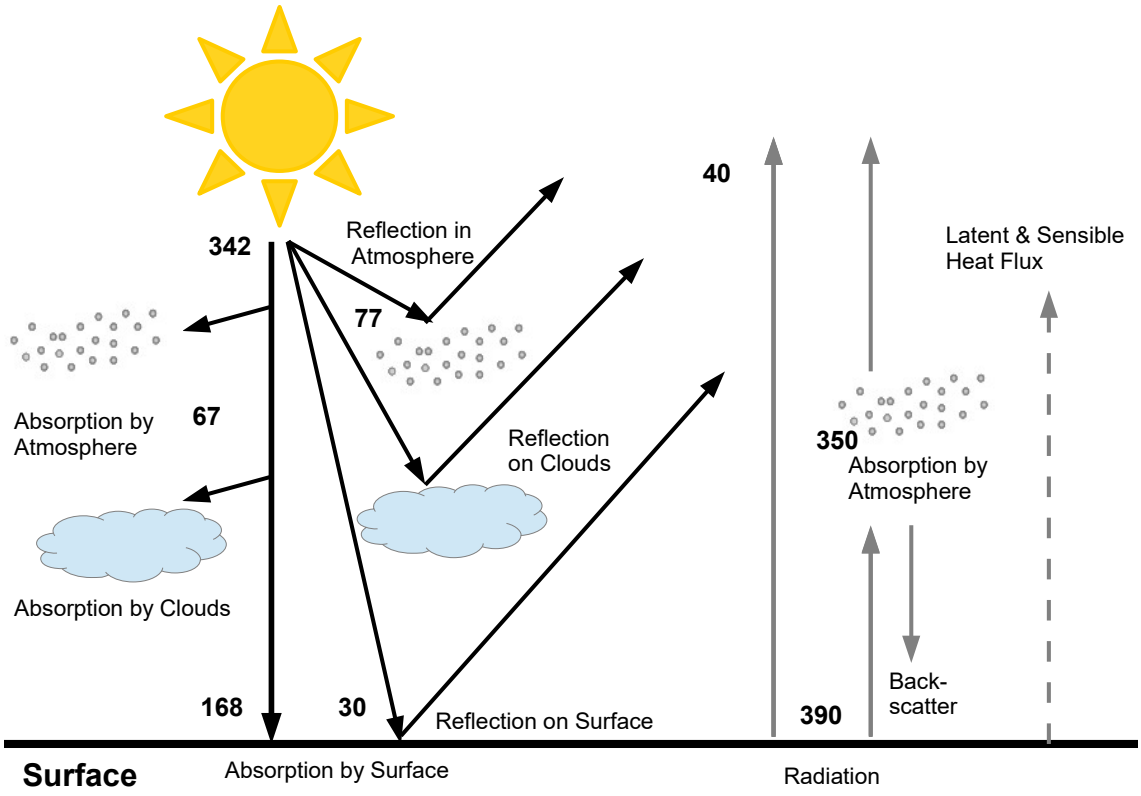

Figure 2.3: Schematic overview of the Earth's radiation budget in [W m^{-2}]. According to Kiehl and Trenberth (1997)

To describe the permeability of the atmosphere the transmittance T_ν is used (Accetta and Shumaker, 2004).

$$T_\nu = exp(-\tau(s)) \tag{2.10}$$

$\tau(s)$ is the optical depth of a layer for a given wavelength, depending on its pathway s and defined as the integral of the extinction coefficient α_{ext} with the unit m^{-1}. α_{ext} is the sum of the absorption coefficient and the scattering coefficient and therefore a measurement for the radiation that is either scattered or absorbed within the layer.

$$\tau(s) = \int_0^s \alpha_{ext}(s')ds' \tag{2.11}$$

2.4.2 Scattering

Scattering changes the direction of radiation. Regarding the radiance in a given direction scattering can lead to a reduction by scattering out, but also to intensification by incoming scattering from other directions. To describe the scattering in a so-called phase function

P is used. P defines the probability for scattering in a given direction and depends on the angle between the incoming and scattered light Ω.

$$\left(\frac{\partial I}{\partial s}\right)_{\text{scattering out}} = -\alpha_s \cdot I \tag{2.12}$$

$$\left(\frac{\partial I}{\partial s}\right)_{\text{scattering in}} = +\alpha_s \cdot \frac{1}{4\pi} \int_0^{4\pi} I(\Omega') P(\Omega'\Omega) d\Omega' \tag{2.13}$$

I displays the radiance, s is the pathway and α_s the scattering coefficient. There are different scattering regimes characterized by the size of the scattering particles and the wavelength of the radiation (Accetta and Shumaker, 2004). The regimes are displayed in figure 2.4. To distinguish the different regimes the size parameter x is given by:

$$x = \frac{2\pi r}{\lambda} \tag{2.14}$$

where r is the particle radius and λ the wavelength. The according regimes are defined as followed:
For $x \ll 1 \rightarrow$ Rayleigh scattering
For $x > 1 \rightarrow$ Mie scattering (only for spherical particles)
For $x \gg 1 \rightarrow$ Geometric optics.
For aerosols the main scattering takes place in the Mie regime as displayed in figure 2.4. Therefore, the Mie scattering plays an important role in this work and will be discussed in more detail in the following section.

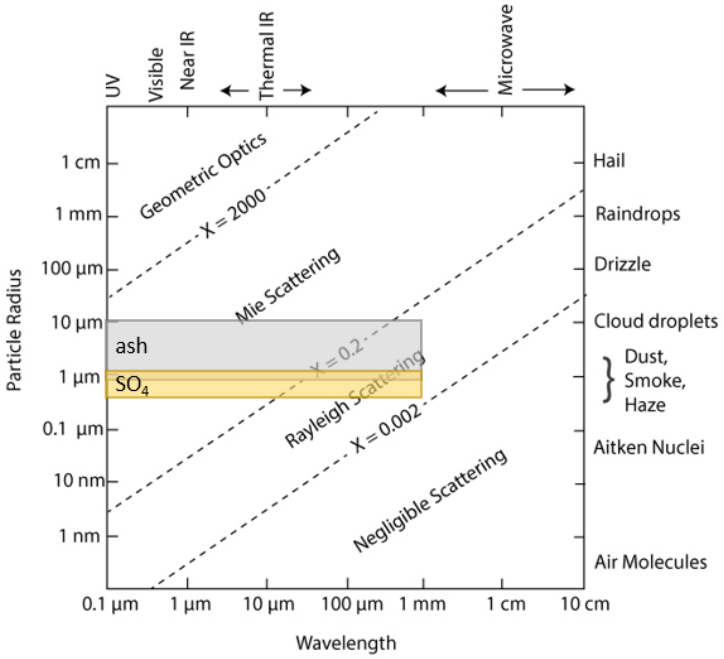

Figure 2.4: Scattering regimes displayed depending on particle radius and wavelength. The grey box displays the size range of ash and the yellow box the size range of sulfur aerosols for the atmospheric radiation. Adapted from Petty (2006)

Mie scattering

The Mie theory only applies to spherical particles in the atmosphere that are mainly aerosols and cloud droplets. For these particles it provides a scattering cross section and phase function depending on the refractive index n, the size parameter α and the scattering angle Θ. The typical cross section for aerosols is only slightly dependent on the wavelength. The phase function shows a strong forward peak for larger particles (Goody and Yung, 1995). The ratio of forward and backward scattered light is defined by the asymmetry parameter g.

$$g = \int_{-1}^{+1} p(\Theta)\cos\Theta d\Theta \tag{2.15}$$

Where values of g describe the following:
$g = +1$ for pure forward scattering
$g = -1$ for pure backward scattering and
$g = 0$ for Rayleigh scattering (symmetric scattering).

To calculate the radiative feedback of aerosols three parameters are essential and can be obtained by using Mie calculations. The parameters are the optical depth $\tau(s)$, that is as explained in section 2.4.1 dependent on the extinction coefficient, the asymmetry parameter g, given in equation 2.15 and the single scattering albedo. The single scattering albedo ω is the ratio of scattering efficiency to total extinction efficiency and can reach values between zero (all radiation is absorbed) and one (all radiation is scattered) (Randles et al., 2004).

2.4.3 Radiative effects of volcanic aerosols

Stratospheric sulfur aerosols, that build as a result of major volcanic eruptions, scatter solar visible (VIS) and ultraviolet (UV) radiation, efficiently (Mie scattering). This causes a reduction of the solar radiation, that reaches the troposphere and therefore cools the system. The backscattering of UV radiation by the sulfur aerosols can cause an enhanced absorption of radiation by O_3 and O_2 and therefore a warming in the stratosphere. The scattering also increases the diffuse radiation (Ramachandran et al., 2000). The solar near-infrared (IR) radiation is partly scattered but also partly absorbed by sulfur aerosols. This means that the solar near-IR contributes to the stratospheric heating. This reduction of solar radiation induces a further cooling of the troposphere. Sulfur aerosols absorb terrestrial long wave radiation efficiently and therefore causes a heating of the lower stratosphere due to the absorbing aerosol layer. The total long wave forcing is small because a lot of long wave radiation is absorbed by water vapor, clouds and other trace gases in the troposphere (Ramachandran et al., 2000).
Volcanic ash has due to its different composition different optical properties than the sulfur aerosols. The optical properties of volcanic ash also depend on the rock type, as the Mie calculations in Walter (2019) show. Compared to the sulfur aerosols, ash absorbs relatively strong in the shortwave regime (Derimian et al., 2012). This absorption can

cause disturbance in the temperature field and the wind pattern, dependent on the ash concentration, as Walter (2019) shows.

3 Mt. Pinatubo eruption 1991

The Mt. Pinatubo is located on the island Luzon in the Republic of the Philippines (15° N, 121° E) and classified as stratovolcano with a caldera and lava domes. It erupted on June 15th in 1991 and it was one of the major eruptions in the twentieth-century and the largest eruption detected with modern instruments. Before that its last major eruption goes back approximately 635 years, although there are probably many undocumented smaller eruptions, since the volcano was not studied in detail before 1991.
The eruption period began with felt earthquakes and increasing SO_2 emissions starting in May 1991. In the second week of June 1991 the dome began to grow and there was an increasing emission of ash and escalating seismic-energy release. In the time from June 12th to 14th there were four vertical eruptions recorded with minor pyroclastic flows. The dome growth and ash emission continued. On the 14th surge-producing eruptions started and continued till the main eruption phase, that began on the 15th of June at approximately 2 PM local time consisting of a large vertical eruption reaching maximum heights up to 40 km and emitting 20 Tg SO_2 and 5.3 km^3 dense rock equivalent (DRE) of ash. Pyroclastic flows traveled up to 16 km from the vent in all directions covering a total area over 400 km^2. The climatic phase lasted for six to nine hours and injected volcanic aerosols up to the stratosphere. Up to late June there where continuous gas emissions and small ash eruptions continued until early September 1991 (Hoblitt, 1996).
Due to the eruption more than 200 000 people had to be evacuated, but still more than 300 people died as an immediate cause of the eruption, mostly due to collapsing homes under heavy ash and rain fall. The rain was strengthened by the 75 km western passing typhoon Tunya. Over 50 000 people had to be displaced, because their homes were destroyed

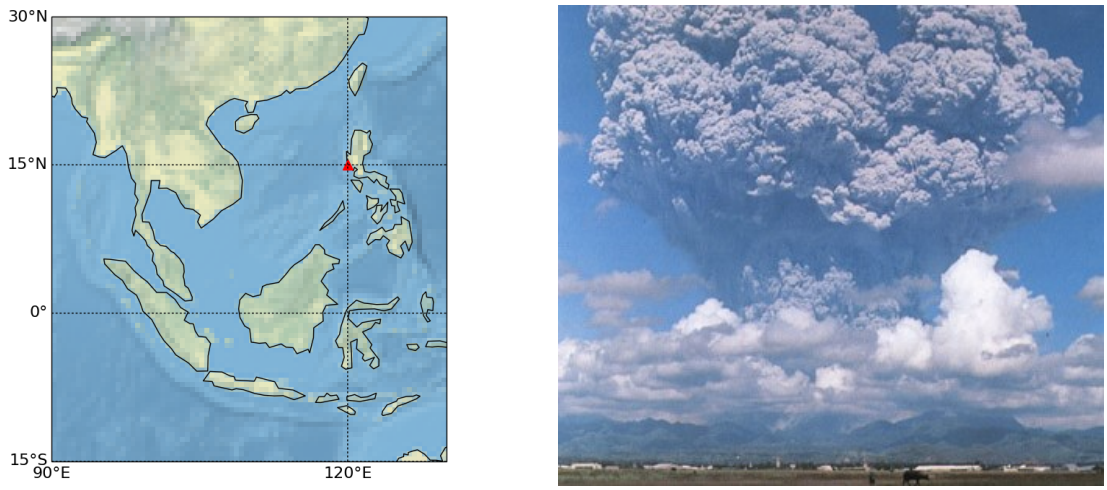

Figure 3.1: Location of the Mt. Pinatubo, the red tingle marks the volcano (left) and the Mt. Pinatubo eruption plume (right), (Newhall and Punongbayan, 1996).

(Bautista, 1996), (McCormick et al., 1995).
After the first signs of activity of the Mt. Pinatubo in April 1991 after an approximately 500 year slumber the Philippine Institute of Volcanology and Seismology (PHIVOLCS) and the U.S. Geological Survey (USGS) started on-site monitoring and a 10 km radius danger zone around the volcano was declared. Further portable instruments were set up to establish a monitoring network around Mt. Pinatubo. Combined with intensive studies of the eruption history the Philippine-American team forecasted a major eruption and urgent warnings were sent out, saving 5000 to 20000 lives.

Atmospheric impact

The Mt. Pinatubo eruption 1991 had a strong impact on the Earth's atmosphere for up to two years. The climatic eruption created a giant umbrella plume reaching up to 500 km in diameter. This plume is classified as a co-ignimbrite plume.
Such plumes can form if very hot, dense material is ejected upwards with up to 300 m s^{-1}, entraining ambient air heats up and expends and results in a buoyant plume. But if the eruption rate is too high or the exit velocity is to low the plume collapses, resulting in pyroclastic flows of hot and dense material. In this flows the pyroclast sediment out, overlaying air entrains, expends and lowers the density of the outflows. If sufficient air is entrained and material peels the top of the current, the development of an coherent, buoyant plume is possible. In this case the thermal energy of the collapsing fountain transfers into the buoyant plume penetrating high into the atmosphere (Woods and Wohletz, 1991). Model studies by Herzog and Graf (2010) have shown, that these plumes are characterized by an overshooting top that can be higher than 10 km of the neutral level of buoyancy on which the plume spreads radially and forms the characteristic umbrella shape.
The Mt. Pinatubo eruption injected volcanic gases and aerosols up to the middle and lower stratosphere, although reaching plume top heights up to 40 km (Bluth et al., 1992), the main height of the umbrella was between 17 km and 30 km (Sheng et al., 2013).
The released 20 Mt SO_2 formed approximately 40 Mt to 50 Mt sulfates, which caused the largest chemical and dynamical perturbation in the stratospheric aerosol layer since the eruption of Krakatau in 1883 (Graft et al., 1993).
The volcanic plume encircled the Earth in 22 days and reached a global coverage after one year. The e-folding time of the SO_2 was observed to be between 23 and 35 days (Read et al., 1993).
These perturbations affected the global radiative processes, leading to a warming in the stratosphere due to long wave absorption by the stratospheric aerosols, mainly SO_4, and a corresponding cooling of the troposphere due to backscattering of these aerosols in the shorter wavelength regime.
The optical depth peaked late in 1992 with values up to 0.4. Global average values for the optical depth was between 0.1 and 0.15 for two years after the eruption and therefore the aerosol plume had a strong impact on the net radiation reaching the Earth's surface and the radiative forcing. In the northern hemisphere the observed cooling effects were up to 0.5 °C, which corresponds to a net radiative reduction of 4 W m^{-2} in 1992 and 1993.

The emission of volcanic aerosols in the stratosphere and the global spreading also had an impact on the atmospheric chemistry, especially on ozone. In the mid-latitudes the ozone concentrations reached the lowest values recorded in 1992 and 1993 and the southern hemisphere ozone hole increased to a new maximum. The destruction of the stratospheric ozone occurs due to heterogeneous reactions on the sulfate aerosol surfaces as well as through circulation changes, caused by the eruption (Self et al., 1993).

4 Model description

The idea of forecasting the weather based on the laws of physics goes back more than hundred years ago, in particular to Abbe (1901) and Bjerknes (1904). In this calculation setup the current state of the atmosphere is seen as an initial value problem and the future weather can be predicted by integrating the according physical differential equations. The first attempts of numerical weather prediction were done by the British scientist Lewis Fry Richardson in the 1920's, but without success, due to rare observations and the lack of technological capacities. The first electronic simulations were hindcasts done in Princeton in 1950 (Charney et al., 1990), whereas the first real-time forecasts were performed in Stockholm in 1954 (Bolin, 1955). The improvement of the meteorological observation and the development of digital computing makes it possible to solve nonlinear differential equations for millions of grid points per time step looking weeks ahead of the initial time and predicting dynamic, thermodynamic, radiative and chemical processes as it is done today.
Based on the Navier-Stokes equation, mass continuity equation, the first law of thermodynamics and the ideal gas law, prognostic equations are established to deliver the changes of meteorological variables. Temporal and special numerical discretion of these equations divides the processes into unresolved and resolved processes. The so called unresolved processes enter the model through parametrizations.
The numeric model used for simulations analysed in this thesis is ICON-ART developed by IMK at the Karlsruhe Institute of Technology in cooperation with German weather service (DWD) as an add-on to the numerical weather prediction (NWP) model ICON, which runs operationally since 2015 (Reinert et al., 2019).

4.1 The ICOsahedral Nonhydrostatic model ICON

ICON (ICOsahedral Nonhydrostatic) is a numeric weather and climate model used and developed by the DWD and the Max-Plank-Institution for Meteorology (MPI-M) (Zängl et al., 2015).
The model has an icosahedral-triangular grid on which it operates and the physical equations are discretized. Compared to a latitude-longitude approach the triangular grid provides a nearly homogeneous coverage of the globe. Another advantage is that transport can only happen through five grid surfaces compared to six surfaces for a latitude-longitude grid.
The global ICON domain is a 20-area spherical icosahedron, which is redefined by root division steps, dividing each edge into n equal sections. Furthermore the sections are redefined by k bisection steps, dividing each edge by two and so creates four triangles within

the previous ones. This procedure results in a so called RnBk grid. The number of cells n_{cell} is then given by

$$n_{cell} = 20n^2 \cdot 4^k \tag{4.1}$$

To calculate the effective grid spacing $\overline{\triangle x}$ the average triangular area of the cells is used.

$$\overline{\triangle x} = \sqrt{\overline{A_{cell}}} = \sqrt{\frac{\pi}{5}} \frac{r_e}{n2^k} \tag{4.2}$$

Where r_e is the Earth's radius.

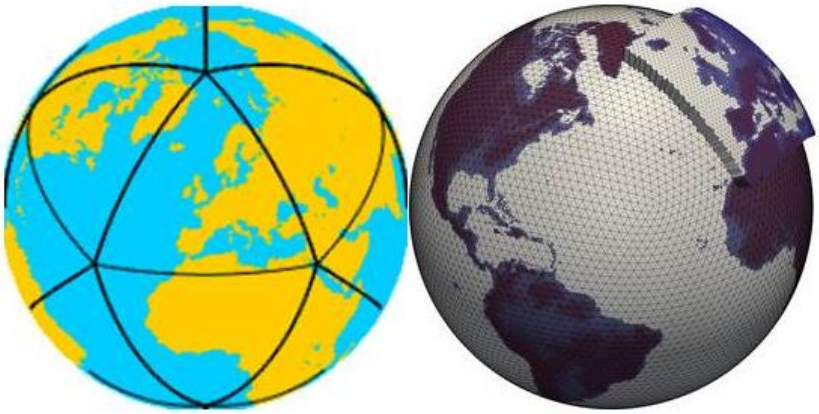

Figure 4.1: Left: Schematic depiction of the icosahedral grid structure of ICON Right: Example of an ICON grid with refinement area over Europe (DWD)

The model solves compressible nonhydrostatic atmospheric equations according to Gassmann and Herzog (2007)

$$\frac{\partial \widehat{v_n}}{\partial t} + \frac{\partial \widehat{K_h}}{\partial n} + (\widehat{\zeta} + f)\widehat{v_t} + \widehat{w}\frac{\partial \widehat{v_n}}{\partial z} = -c_{pd}\widehat{\Theta_v}\frac{\partial \overline{\pi}}{\partial n} - F(v_n) \tag{4.3}$$

$$\frac{\partial \widehat{w}}{\partial t} + \widehat{\overrightarrow{v_h}} \cdot \nabla \widehat{w} + \widehat{w}\frac{\partial \widehat{w}}{\partial z} = -c_{pd}\widehat{\Theta_v}\frac{\partial \overline{\pi}}{\partial z} - g \tag{4.4}$$

$$\frac{\partial \overline{\rho}\widehat{\Theta_v}}{\partial t} + \nabla \cdot (\overline{\rho}\,\widehat{\overrightarrow{v}}\,\widehat{\Theta_v}) = \overline{Q} \tag{4.5}$$

$$\frac{\partial \overline{\rho}}{\partial t} + \nabla \cdot (\overline{\rho}\,\widehat{\overrightarrow{v}}) = 0 \tag{4.6}$$

$$\frac{\partial \widehat{\rho q_k}}{\partial t} + \nabla \cdot (\overline{\rho}\widehat{q_k}\,\widehat{\overrightarrow{v}}) = -\nabla \cdot (\overrightarrow{J_k} + \overline{\rho q_k'' \overrightarrow{v}''}) + \overline{\sigma_k} \tag{4.7}$$

In ICON the prognostic variables are the horizontal wind velocity component normal to the triangle edges v_n, the vertical wind component w, the density ρ and the virtual potential temperature Θ_v. To calculate the wind components the three dimensional wind vector $\overrightarrow{v}$ is used consisting of the normal wind component v_n, the tangential wind component v_t and the vertical wind component w. Further the time t, height h, vertical vorticity component ζ, Coriolis parameter f, horizontal component of the kinetic energy $\widehat{K_h} = \frac{1}{2}(\widehat{v_n}^2 + \widehat{v_t}^2)$, Exner function π, specific heat capacity of air for a specific pressure c_{pd} and a constant volume c_{vd}, the gas constant of dry air R_d, gravitational acceleration g and the reference pressure p_{00} at 1000 hPa are needed. Last $\frac{\partial}{\partial n}$ is the horizontal edge-normal derivative, $F(v_n)$ is a source term for horizontal momentum and $\overline{Q}$ is the diabatic heat source term. As explained, ICON solves a prognostic equation for the density, therefore exact mass conservation is achieved. The used averages are the Hesselberg average, which uses the barycentric mean and the according fluctuation and the Raynolds average. Both will be discussed in the following section in more detail.
To calculate physical processes ICON makes use of a time splitting approach. This approach divides the dynamical core and the tracer advection and physical parametrizations due to different numerical stability criteria. The maximum allowed time step for the air continuity equation solved in the dynamical core is limited to the speed of sound for non-hydrostatic models, whereas the maximum time step for the tracer continuity equation is limited by the wind speed. This conditions that longer time steps are used for tracer transport and physical parametrizations than the dynamical core and therefore mass-consistent tracer transport is achieved by transporting time-averaged mass fluxes. Slow physical parametrizations like convection, cloud cover, radiation, non-orographic wave drag and sub-grid scale orographic drag can be assigned to a third even longer time step, which then passes tendencies to the dynamical core rather than updating the atmospheric state directly.

4.2 The ICON model with its ART-extension for Aerosols and Radiative Trace gases

ART stands for Aerosol and Radiative Trace gases and is an extension of ICON. The ART sub module is developed at the Karlsruhe Institute of Technology and its interfaces are part of the official ICON code. The ART module makes it possible to calculate reactive trace substances and their interaction with the atmosphere online. A more detailed description is given by Rieger et al. (2015).
In ART several different aerosols e.g. mineral dust, volcanic ash, sea salt, pollen and radioactive substances can be simulated. To simulate the atmospheric chemistry three mechanisms are provided. The first is reduced to stratospheric short-lived Bromocarbon cycles, the second calculates a simplified OH chemistry and takes photolysis rates into account and the third calculates the full gas phase chemistry.
As explained the tracer transport in ICON-ART is based on a time-split method that separates the horizontal and vertical wind component, but keeps the tracer and air mass consistent. Temporal averaged mass fluxes then enter the transport scheme in the dynam-

ical core and are diagnostically re-integrated on the mass continuity.
To describe the treatment of aerosol and gas tracers the barycentric mean in respect to the air density is used and indicated with a hat (equation (4.8)). Ψ thereby is a mass-specific variable. Variables with a bar respond to the Raynolds average and two apostrophes indicate the fluctuation.

$$\widehat{\Psi} = \frac{\overline{\rho\Psi}}{\overline{\rho}} \tag{4.8}$$

$$\Psi'' = \Psi - \widehat{\Psi} \tag{4.9}$$

$$\widehat{\frac{\mathrm{d}}{\mathrm{d}t}} = \frac{\partial}{\partial t} + \widehat{\mathbf{v}} \cdot \nabla \tag{4.10}$$

$$\widehat{\frac{\mathrm{d}\overline{\rho}}{\mathrm{d}t}} = -\overline{\rho}\nabla \cdot \widehat{\mathbf{v}} \tag{4.11}$$

4.2.1 Gaseous tracers

Equation (4.10) displays the barycentric mean of the total derivative and equation (4.11) the continuity equation. ICON-ART considers gaseous tracers as its barycentric-averaged mass mixing ratio $\widehat{\Psi_{g,l}}$, the ratio of the partial gas density l and the total density (4.12), according to Rieger et al. (2015).

$$\widehat{\Psi_{g,l}} = \frac{\overline{\rho_l}}{\overline{\rho}} \tag{4.12}$$

The spatial-temporal evolution of a gaseous tracer is given in equation (4.13) in flux form and depends on the flux divergence term that contains the horizontal and vertical advection of the gas tracer, the changes through turbulent fluxes, the chemical production and loss rate as well as the emissions.

$$\underbrace{\frac{\partial(\overline{\rho}\widehat{\Psi_{g,l}})}{\partial t}}_{\substack{\text{spatiotemporal evolution} \\ \text{of gas tracer}}} = -\underbrace{\nabla \cdot (\widehat{\mathbf{v}}\overline{\rho}\widehat{\Psi_{g,l}})}_{\text{flux divergence}} - \underbrace{\nabla \cdot \overline{\rho\mathbf{v}''\Psi''_{g,l}}}_{\substack{\text{turbulent} \\ \text{flux}}} + \underbrace{P_l}_{\substack{\text{chemical} \\ \text{production}}} - \underbrace{L_l}_{\substack{\text{chemical} \\ \text{loss}}} + \underbrace{E_l}_{\text{emission flux}} \tag{4.13}$$

4.2.2 Monodisperse aerosols

Monodisperse aerosols are described, according to Rieger et al. (2015), with the barycentric mean in equation (4.14) where M_l represents the mass concentration of the aerosol. The balance equation in flux form of the monodisperse aerosol is given in equation (4.15), v_{sed} represents the sedimentation velocity and λ_l the wash out coefficient.

$$\widehat{\Psi_l} = \frac{\overline{M_l}}{\overline{\rho}} \tag{4.14}$$

$$\underbrace{\frac{\partial(\overline{\rho}\widehat{\Psi_l})}{\partial t}}_{\substack{\text{spatiotemporal evolution}\\ \text{of aerosol}}} = -\underbrace{\nabla\cdot(\widehat{\mathbf{v}}\overline{\rho}\widehat{\Psi_l})}_{\text{flux divergence}} - \underbrace{\nabla\cdot\overline{\rho\mathbf{v}''\Psi_l''}}_{\substack{\text{turbulent}\\ \text{flux}}} - \underbrace{\frac{\partial}{\partial z}(v_{sed,l}\overline{\rho}\widehat{\Psi_l})}_{\text{sedimentation flux}} - \underbrace{\lambda_l\overline{\rho}\widehat{\Psi_l}}_{\text{wash out}} + \underbrace{E_l}_{\text{emission flux}} \tag{4.15}$$

4.2.3 Polydisperse aerosols

The treatment of polydisperse aerosols in ICON-ART is based on the MADEsoot model (Modal Aerosol Dynamics Model for Europe, extended by soot, Vogel et al. (2009)), as described in Rieger et al. (2015) in more detail. The participles are represented by several log normal distributions, thereby the mass mixing ratio and the specific number are considered prognostic variables, whereas the median diameter is considered a diagnostic variable. The standard deviation is kept constant. During a simulation several processes influence the median diameter of the particle distribution. Because the number as well as the mass are prognostic, both barycentric averages are needed and given in equations (4.16) and (4.17). The indices 0 and 3 indicate the moment of the distribution (mass specific number and mass mixing ratio).

$$\widehat{\Psi_{0,l}} = \frac{\overline{N_l}}{\overline{\rho}} \tag{4.16}$$

$$\widehat{\Psi_{3,l}} = \frac{\overline{M_l}}{\overline{\rho}} \tag{4.17}$$

Analogous to the monodisperse spatial-temporal evolution the prognostic equations for $\widehat{\Psi_{0,l}}$ and $\widehat{\Psi_{3,l}}$ are established in equations (4.18) and (4.19). v_{sed} stands for the sedimentation velocity, W_l denotes the loss of particles due to wet below-cloud scavenging and E_l for the number or mass emission flux.

$$\underbrace{\frac{\partial(\overline{\rho}\widehat{\Psi_{0,l}})}{\partial t}}_{\substack{\text{spatiotemporal evolution}\\ \text{of aerosol}}} = -\underbrace{\nabla\cdot(\widehat{\mathbf{v}}\overline{\rho}\widehat{\Psi_{0,l}})}_{\text{flux divergence}} - \underbrace{\nabla\cdot\overline{\rho\mathbf{v}''\Psi_{0,l}''}}_{\substack{\text{turbulent}\\ \text{flux}}} - \underbrace{\frac{\partial}{\partial z}(v_{sed,0,l}\overline{\rho}\widehat{\Psi_{0,l}})}_{\text{sedimentation flux}} - \underbrace{W_{0,l}}_{\substack{\text{wet below-cloud}\\ \text{scavenging}}} + \underbrace{E_{0,l}}_{\substack{\text{number}\\ \text{emission flux}}} \tag{4.18}$$

$$\underbrace{\frac{\partial(\overline{\rho}\widehat{\Psi_{3,l}})}{\partial t}}_{\substack{\text{spatiotemporal evolution}\\ \text{of aerosol}}} = -\underbrace{\nabla\cdot(\widehat{\mathbf{v}}\overline{\rho}\widehat{\Psi_{3,l}})}_{\text{flux divergence}} - \underbrace{\nabla\cdot\overline{\rho\mathbf{v}''\Psi_{3,l}''}}_{\substack{\text{turbulent}\\ \text{flux}}} - \underbrace{\frac{\partial}{\partial z}(v_{sed,3,l}\overline{\rho}\widehat{\Psi_{3,l}})}_{\text{sedimentation flux}} - \underbrace{W_{3,l}}_{\substack{\text{wet below-cloud}\\ \text{scavenging}}} + \underbrace{E_{3,l}}_{\substack{\text{number}\\ \text{emission flux}}} \tag{4.19}$$

As visible in the previous equations emission plays an essential role for primary and secondary aerosols as well as gaseous components and must be parametrized. Sedimentation also is an important loss for the tracer and is treated as an additional downward directed vertical advection. Turbulence and dry deposition are calculated with an one dimensional TKE turbulence scheme according to Raschendorfer (2001). Different parametrizations are used for wash out according to the aerosol properties (monodisperse/polydisperse).

4.3 The aerosol module AERODYN

The aerosol module AERODYN (AEROsol DYNamics) is currently developed at the KIT. This module does not consider several modes for an aerosol spices but divides all species into four modes. The smallest being the Aitken mode, followed by the accumulation mode, the coarse mode and the giant mode. As displayed in figure 4.2 the different modes can

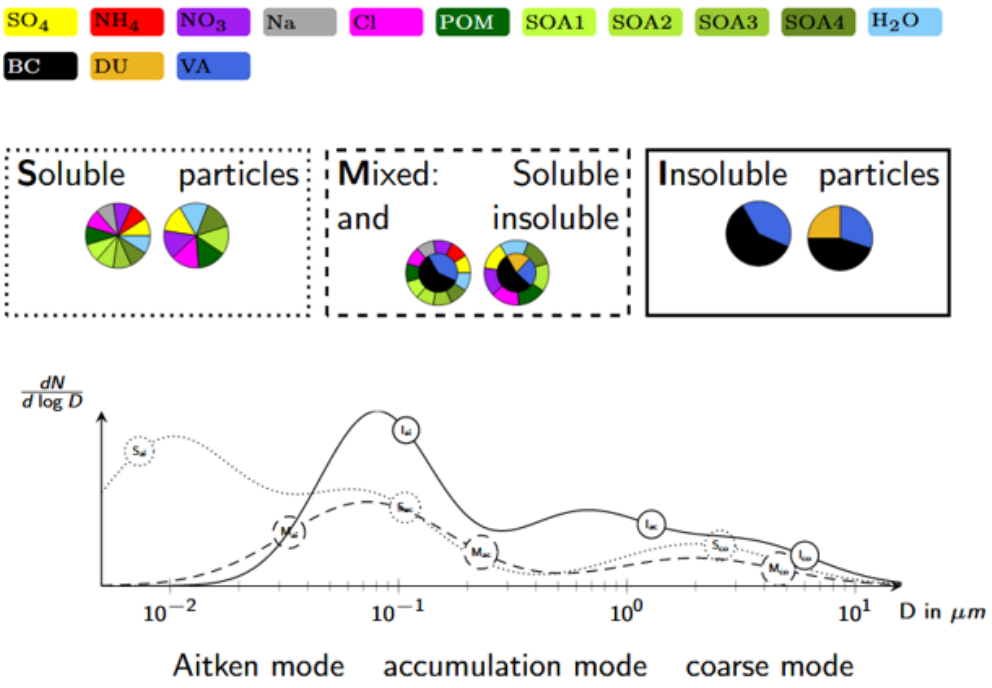

Figure 4.2: Schematic description of the AERODYN aerosol treatment (Working group)

be divided into a soluble, insoluble and mixed modes. The species considered in this thesis are sulfate (SO_4), ammonia (NH_4), nitrate (NO_3), sodium (Na), chlorine (Cl), water (H_2O) in the soluble phase and black carbon, soot and volcanic ash in the insoluble phase. The mixed phase is defined for an aerosol consisting of an insoluble core with at least five mass percent of a soluble species.

AERODYN can to calculate the nucleation of particles. The implemented nucleation scheme calculates a critical concentration c_{crit} according to Kerminen and Wexler (1994). If the calculated H_2SO_4 concentration is higher (after subtracting the H_2SO_4, that con-

densates on existing particles) than the critical concentration the difference is the H_2SO_4 available for nucleation.

$$c_{crit} = 0.16 \times exp(0.1 \cdot T - 3.5RH - 27.7) \tag{4.20}$$

The critical concentration is defined according to the numerical value equation (4.20) with the unit μg m^{-3} and depends on the temperature T in Kevin and the relative humidity RH in a scale 0.01.
Gases can condensate on particles in the soluble, insoluble and mixed mode and causes the particles to grow and can lead to changes in their composition. This can result in shifts into different size and phase modes.
Implemented is a mode shift from the Aitken to the accumulation mode, if the diameter exceeds 0.3 μm through condensational growth. Another mode shift takes place from the insoluble mode to the mixed mode, if the condensed material on the particle is larger more than five mass percent and therefore the particle consists of soluble and insoluble species.
Another aerosol dynamic effect in AERODYN is coagulation. The coagulation coefficients are calculated for every mode with every other mode. Coagulation of different modes in size and phase can also lead to mode shifts. In terms of phase, there are no changes of modes if same phase modes coagulate. For example, if two particles in the soluble mode coagulate, the new formed particle will also be in the soluble mode (analogously for the insoluble and mixed mode). If either insoluble or soluble particle coagulate with a mixed phase particle it will result in a mixed particle. If an insoluble particle collides with a soluble particle it will also result in the mixed mode. Regarding size shifts, these are only taking place if two different sized particles coagulate. So, if two Aitken mode particles collide the new particle will still be in the Aitken mode (the same for accumulation and coarse mode). The collusion of two different sized particles always results in a larger particle mode. For example, the coagulation of an Aitken mode or an accumulation mode particle with a coarse particle will always result in a coarse mode particle.

4.4 Radiative transfer scheme in ICON

ICON uses the Rapid Radiative Transfer Model (RRTM) by Mlawer et al. (1997) to calculate long wave fluxes, shortwave fluxes and heating rates in the atmosphere for 30 spectral bands between 200 nm up to 1000 μm.
The RRTM is a broadband correlated k-distributed radiation model. The physical basis relies on the conversion of the absorption coefficient $k(\nu)$ into a cumulative probability function $k(g)$ for each spectral band j. This is done to get a representative evaluation of the spectral highly variable absorption coefficient due to singular absorption lines by gases. The conversion is done by reordering the absorption coefficients $k(\nu)$ with the number of occurrences. $k(g)$ is referred to as k-distribution. In the reordering process the highly resolved spectral information is lost, which does not affect the radiative transfer calculations carried out and still provides the main absorption characteristics.

The radiative transfer calculations can be conducted in a monochromatic way in each spectral band for every layer in the model. This is done using a two-stream method, so that radiation can only propagate in two discrete directions, assuming a linearly varying Plank emission function along the absorption path and a homogeneous layer with respect to pressure, temperature and species distribution. A characteristic value for the absorption coefficient $k_j = k(g)_j$ is calculated for every spectral band. To include the effect of atmospheric variables k_j is parametrized as a function of atmospheric conditions, a detailed description can be found in Mlawer et al. (1997). The calculated outgoing radiance is used as the incoming radiance for the bordering layer, which makes the k distributions fully correlated.

4.5 Radiative effect of aerosols in ICON-ART

The ART aerosol radiation routine is part of the ICON radiation routine and therefore called at every time step the ICON radiation routine is called. The ART routine calculates the optical depth τ_j^*, the single scattering albedo ω_j^* and the asymmetry parameter g_j^* as introduced in section 2.4.1 for 30 wavebands j and every model layer (denoted with asterisk). These parameters are determined for the local ART aerosol concentration. To derive the local radiative transfer parameters the mass extinction coefficient $k_{l,j}$, the single scattering albedo $\omega_{l,j}$ and the asymmetry parameter $g_{l,j}$ are necessary for every mode l and every wave band j which are obtained using Mie calculations. The volume specific optical parameters are calculated as followed:

$$\beta_{e\ l,j} = k_{l,j}\rho_a\Psi_{3,l} \times 10^{-6} \tag{4.21}$$

$$\beta_{s\ l,j} = \omega_{l,j}\beta_{e\ l,j} \tag{4.22}$$

$$\chi_{l,j} = \beta_{s\ l,j}g_{l,j} \tag{4.23}$$

where ρ_a is the air density and $\Psi_{3,l}$ is the local aerosol mass mixing ratio.
To be able to introduce the aerosol radiative properties in the ICON RRTM scheme it is necessary to sum the optical properties over the single modes l and convert the volume specific values into values per model layer. This is done by multiplying with the according layer height Δz for every grid box, assuming that the volume extinction coefficient is homogeneous throughout the layer. A further summation over all layers gives the aerosol optical depth of the ART aerosols at a specific waveband.

4.6 Implementing the radiative effects for volcanic aerosols in ICON-ART

The implementation of the aerosol radiative effects in the new aerosol module AERODYN are done analogue to Walter (2019). Besides the radiative effects of the volcanic ash, the radiative effects of secondary particles (sulfate aerosols and aged ash) can now be calculated in the model.

As mentioned in section 4.5, to calculate the radiative effect of aerosols in ICON-ART the mass extinction coefficient $k_{l,j}$, the single scattering albedo $\omega_{l,j}$ and the asymmetry parameter $g_{l,j}$ for every mode l and every waveband j are necessary and obtained by Mie calculations. The Mie calculations are done offline and the results are implemented in ICON-ART in so called look-up tables, that contain mass extinction coefficient, the single scattering albedo and the asymmetry parameter for the according mode and waveband.

The Mie calculation for this thesis are done by Gholamali Hoshyaripour for SO_4 in the Aitken and accumulation mode, for volcanic ash in the accumulation and coarse mode, separating between insoluble ash and ash in the mixed phase (containing a soluble cover) and also, for volcanic ash in the giant mode. For all aerosols a spherical shape is assumed.

Table 4.1: Diameter and standard deviation of according mode

Species	Phase	Mode	Median diameter [μm] ICON-ART	Median diameter [μm] Mie calculations	Standard deviation [μm]
SO_4	soluble	Aitken	0.01	0.03	1.7
SO_4	soluble	accumulation	0.07	0.12	1.7
ash	insoluble	accumulation	0.6445	0.6445	1.7
ash	insoluble	coarse	3.454	3.454	2.0
ash	insoluble	giant	12.0	12.0	1.7
ash	mixed	accumulation	0.08	0.08	2.0
ash	mixed	coarse	2.0	2.0	2.0

For the soluble SO_4 particles a 75% -H_2SO_4 -25% -H_2O solution is assumed. According to Russell et al. (1996) the mass fraction of the H_2SO_4-H_2O post Mt. Pinatubo aerosols was between 65-80%, which is consistent with theoretical calculations for stratospheric conditions of about -50°C and a water vapor mixing ratio of 3-5 ppmv, and therefore agrees with the assumptions made in this thesis.

Table 4.1 displays the median diameter implemented in ICON-ART and used for the Mie calculations for the specific modes. The ICON-ART initial values for the modes other than the soluble have been used for the Mie calculations. To get more accurate values for the soluble SO_4 particles due to new particle formation and growth, a statistical analysis of the diameter has been done for a four day test simulation of an eruption comparable

with the Mt. Pinatubo eruption. The frequency distribution for the median diameter of the according mode is calculated in the area from 0° - 130° E and 35° N - 25° S, between 4 km and 30 km. This is the area in which the eruption spreads during the four day test simulation. To calculate the frequency distribution 80 bins between 0.5 nm and 0.04 μm for the soluble Aiken mode and between 5 nm and 0.4 μm for the accumulation mode are chosen. The result is displayed in figure 4.3 for different time steps: 24 h, 48 h, 72 h and 96 h after the eruption. For the Aitken mode there are three peaks visible, one at 0.01 μm,

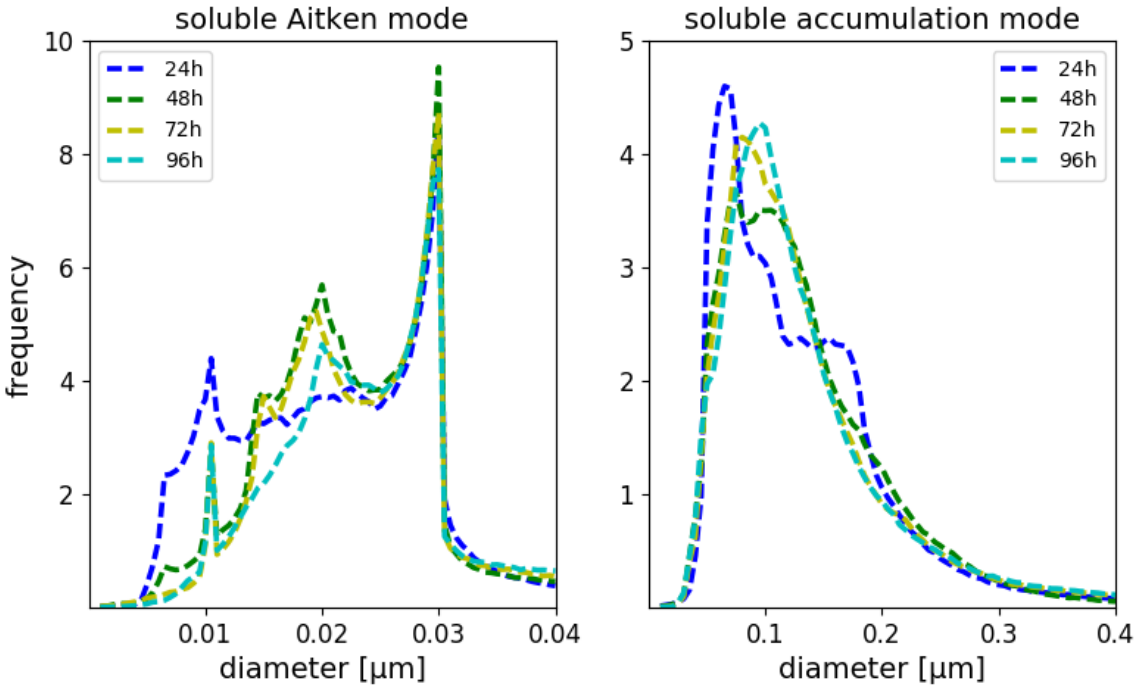

Figure 4.3: Frequency distribution of the soluble Aitken mode median diameter (left) and the soluble accumulation mode median diameter (right) in the area of the eruption plume (0 ° - 130° E, 35 ° N - 25 ° S, between 4 km and 30 km) at different time steps after the eruption

one at 0.02 μm and one at 0.03 μm. The soluble Aitken mode is initialized with 0.01 μm, which is an explanation for the first peak. The third peak, has a steep decrease, due to the mode shift at 0.03 μm to the accumulation mode. A median diameter for the soluble Aitken mode of 0.03 μm is chosen and used for the Mie calculations.

Towards the end of the simulation a peak outlines for the soluble accumulation mode, which is around 0.1 μm. For the Mie calculations a mean median diameter of 0.12 μm is assumed.

For the mixed particles an insoluble core is assumed, covered by a fixed soluble shell, that makes 20% of the particle radius. The soluble shell consists of a 50% -H_2SO_4 -50% -H_2O solution.

All calculations assume a temperature of 215 K. The exact results of the Mie calculations are enclosed in the appendix A. In this thesis only the radiative effects of the SO_4 in the soluble Aitken and accumulation mode and ash insoluble and mixed in the coarse mode are regarded and displayed in figure 4.4. The extinction is highest for SO_4 particles in

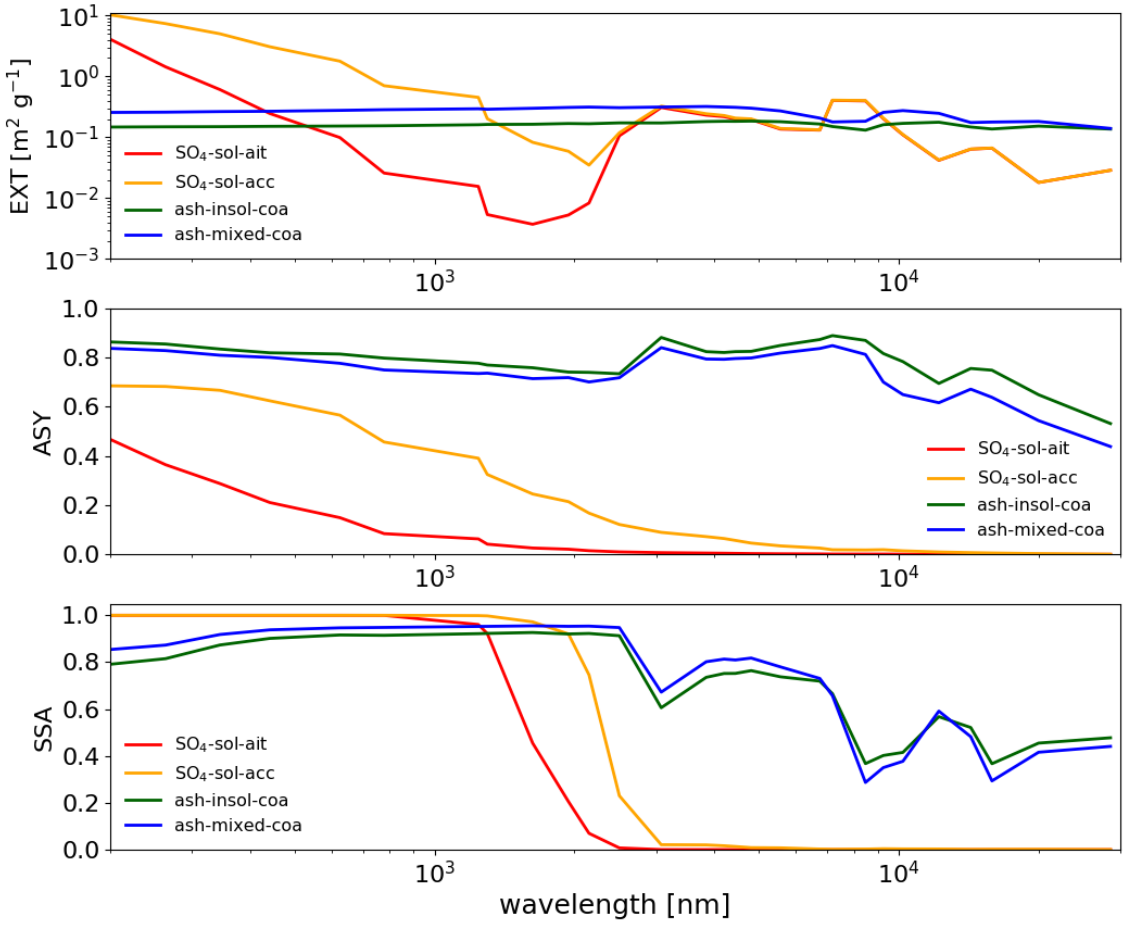

Figure 4.4: Extinction coefficient, asymmetry parameter and single scattering albedo for SO_4 in the soluble Aitken and accumulation mode, ash in the insoluble and mixed coarse mode depending on the wavelength, generated by Mie calculations.

the accumulation mode with values up to 10.3 m ^{2} g^{-1} for the smallest wavelength band and decreasing with growing wavelengths until reaching the long wave spectrum. The SO_4 particles in the Aitken mode have a similar trend, but lower extinction in the shortwave to near infrared with a maximum of 4.1 m^2 g^{-1}. The extinction for both types is due to scattering in the shortwave and absorption in the long wave. This is outlined by the single scattering albedo (SSA) figure 4.4 in the lower plot. The extinction of the ash particles is comparably steady. The insoluble ash has in mean the lowest extinction between 0.13 m^2 g^{-1} to 0.18 m^2 g^{-1}. Ash in the mixed mode is in mean 0.1 m^2 g^{-1} higher. The ash mainly scatters in the shortwave regime although not as efficiently as the sulfate particles and scatters as wall as it absorbs in the long wave. The asymmetry parameter measures the scatter symmetry, as explained in section 2.4.2. Zero denotes symmetric scattering and one forward scattering. The SO_4 particles absorb in the long wave regime, therefore the asymmetry parameter is zero and scatter forwards in the shortwave. The ash particles scatter mainly forward over all wavelengths.

4.7 Model setup

For this thesis a set of global simulations are done on a R2B6 grid, which corresponds to a 40 km resolution. Reanalysis data from ERA-Interim is used as meteorological input to start the simulation. To calculate the chemistry a simplified OH mechanism is used, that was developed to simulate the tropospheric OH chemistry but can be adapted for the lower stratosphere, as explained in Weimer et al. (2017).
The OH production is thereby given through the photolysis of ozone, producing an oxygen atom in exited state $O(^1D)$ which can then react with nitrogen (N_2), oxygen (O_2) or H_2O. Last leads to the production of two OH radicals. The sinks for OH in this simplified model are only methane (CH_4) and carbon monoxide (CO).
The OH is also the limiting factor for H_2SO_4 production, since it reacts with SO_2, as shown

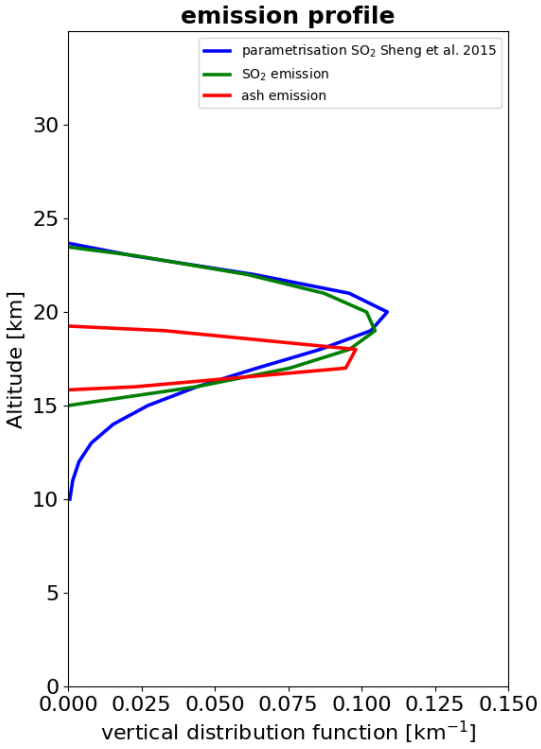

Figure 4.5: Emission profiles for SO_2 as given in Sheng et al. (2015) (blue) and used in the simulation (green) and the ash emission (red)

in equation (4.24) and SO_2 is in case of the Mt. Pinatubo eruption highly concentrated.

$$SO_2 + OH \; + \; (+ \; ...) \rightarrow H_2SO_4 + \text{products} \tag{4.24}$$

The initialization of the eruption is based on Sheng et al. (2015) and Niemeier et al. (2009). Sheng et al. (2015) did a comparison of different SO_2 emission profiles of the Mt. Pinatubo eruption evaluating a best fit emission profile given in figure 4.5 in blue.
A total mass of 18 Tg SO_2 is emitted over 6 hours starting at the 15th of June 1991 at

6:00 UTC, following the implemented emission profile in green (figure 4.5).
For the ash emission the setup is initialized according to Niemeier et al. (2009). The ash particles have a median diameter of 2.4 μm and are emitted between 50 hPa and 100 hPa, which corresponds to a height between 15.8 km and 19.3 km. For this simulation a total mass of 100 Tg of insoluble ash in the coarse mode (2.4μm diameter with a standard deviation of 1.8 μm) is emitted at the same time as the SO_2. Figure 4.5 displays the according emission profiles.
To analyse the aerosol distribution, new particle formation and radiative effects two sets of simulations are done. One simulation regarding the new implemented radiative effects of the volcanic aerosols, onward also referred to as case RAD and a second reference simulation is done, without calculation the radiative aerosol effects, onward referred to as case REF. In both cases ten days are simulated.

5 Results

5.1 Comparison of the model results with existing literature

In the following sections the ICON-ART simulations of the Mt. Pinatubo eruption done for this thesis, will be compared to satellite data published by Guo et al. (2004a) and previous simulations of the eruption (Aquila et al., 2012), (Ramachandran et al., 2000).

5.1.1 Distribution of the SO_2 plume

In the first days after the eruption are only limited measurements available to compare the simulation results, but satellite data from the Total Ozone Mapping Spectrometer (TOMS) and NOAA's TIROS Operational Vertical Sounder (TOVS) is published by Guo

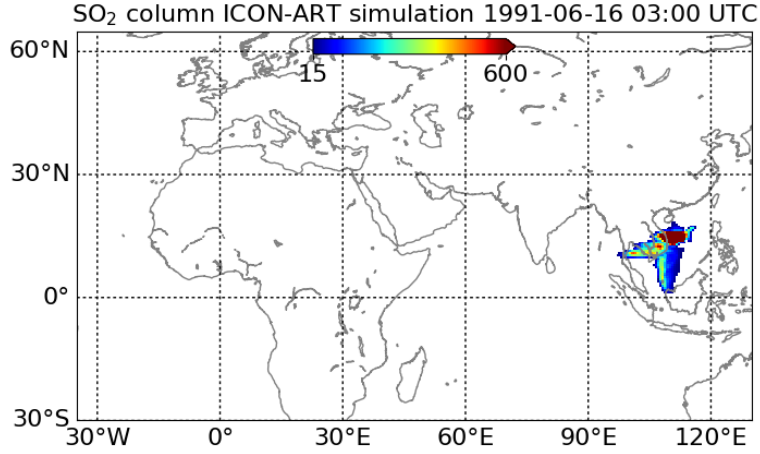

Figure 5.1: TOMS SO_2 column in DU, June 16 1991, 03:44 UTC and 02:01 UTC (top) (Guo et al., 2004a). Simulated SO_2 column in DU with ICON-ART, June 16 1991, 03:00 UTC (bottom)

et al. (2004a). In the following section the results of the ICON-ART simulation will be compared with the results of Guo et al. (2004a), who did a re-evaluation of SO_2 release of the June 15th, 1991 Mt. Pinatubo eruption using ultraviolet and infrared satellite sensors. The result is that the TOVS (infrared) SO_2 mass estimation is in general about 5% to 30% higher than the SO_2 mass retrieved by the TOMS measurements in the ultraviolet. But similar shapes and spreadings of the plume have been detected by both. The interference of ash and ice with the SO_2 plume of the imaging is unbiased. The blue lines in the satellite images figures 5.1, 5.3 and 5.4 top plots, indicate the orbital swath's central scan position. Figure 5.1 shows the TOMS images and the ICON-ART simulation of the SO_2 column on the 16th of June 1991. Regarding the distribution and location of the maximum concentration both are in good agreement, but the simulations show a southern branch at around 110°E, that is not detected by the TOMS instrument. Further analysis of the simulation show that the branch develops though northern winds between 13 km and 16 km. This simulated wind pattern agrees with ERA-Interim data as figure 5.2 shows. The wind pattern transporting the volcanic erupt southwards agrees with the

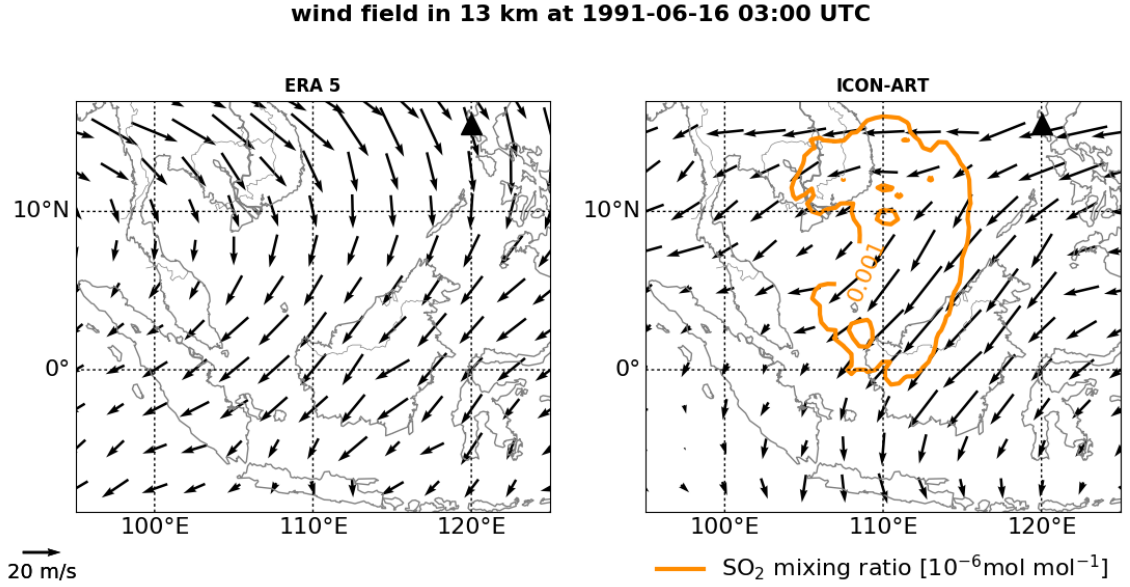

Figure 5.2: Wind field at 13 km on the 16th of June 1991 at 03:00 UTC. The black triangle marks the location of Mt. Pinatubo. ERA 5 re-analysis data (left) and ICON-ART simulation (right), the orange lines displays the SO_2 isoline.

ERA 5 data. Above 10°N the wind directions differ. Whereas the ERA 5 data shows north-western winds the ICON-ART simulation calculates eastern winds, transporting the eruption plume to the west. This movement moreover agrees with the satellite data in figure 5.1. Regarding the maximum values in figure 5.1, the simulated concentrations are more than 7.5 times higher than the measured ones. The measurements peak at 600 DU, whereas the simulation calculates a maximum value of 4559 DU. An explanation for the differences could be the interference of ash with the SO_2 plume. At this point (15 h after the eruption) ash is still highly concentrated in the eruption plume and unbiased in the TOMS imaging. The comparison of the TOVS imaging and the simulation two days after the eruption in figure 5.3 shows that the simulated maximum concentration is still more

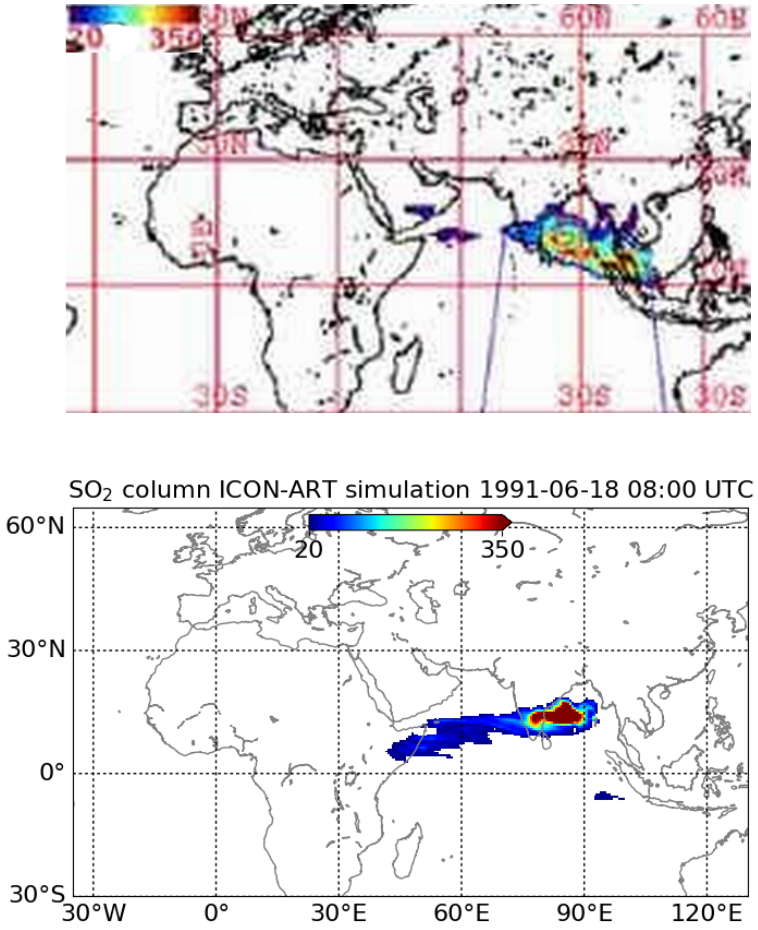

Figure 5.3: TOVS SO_2 column in DU, June 18 1991, 08:43 UTC and 07:25 UTC (top) (Guo et al., 2004a). Simulated SO_2 column in DU with ICON-ART, June 18 1991, 08:00 UTC (bottom).

than three times larger with a maximum value of 1143 DU. The calculated distribution peaks further west and has a slightly southward trend, whereas the measured SO_2 peaks further east with a northward trend. The TOVS images also show concentrations higher than 20 DU over the Arabian sea, that are simulated further south over Somalia. In figure 5.3 (bottom) the structures of a south-east branch are visible, that formed from the southern branch in figure 5.1 (bottom). Overall the simulated SO_2 plume is less transported to the west and has a more concentrated peak.

Figure 5.4 compares the SO_2 column one week after the eruption. The TOMS instrument measured values up to 150 DU, the simulated maximum is 156 DU, which is in good agreement. The approximating of the concentrations in measurements and simulations can be explained by decreasing interference of ash with the UV imaging, since even fine ash only has a lifetime of a few weeks. Another explanation could be, that the simulated SO_2 decays faster, resulting in a faster building of sulfate aerosols. Regarding the distribution and location of the SO_2 plume, figure 5.4 (top) shows that the plume spreads over the Indian ocean along the equator reaching Sudan in the west. In contrary to figure 5.3, the simulated plume spreads over North Africa, which indicates a faster transport and wider distribution of the plume. Also, the plume spreads further north, which could be explained

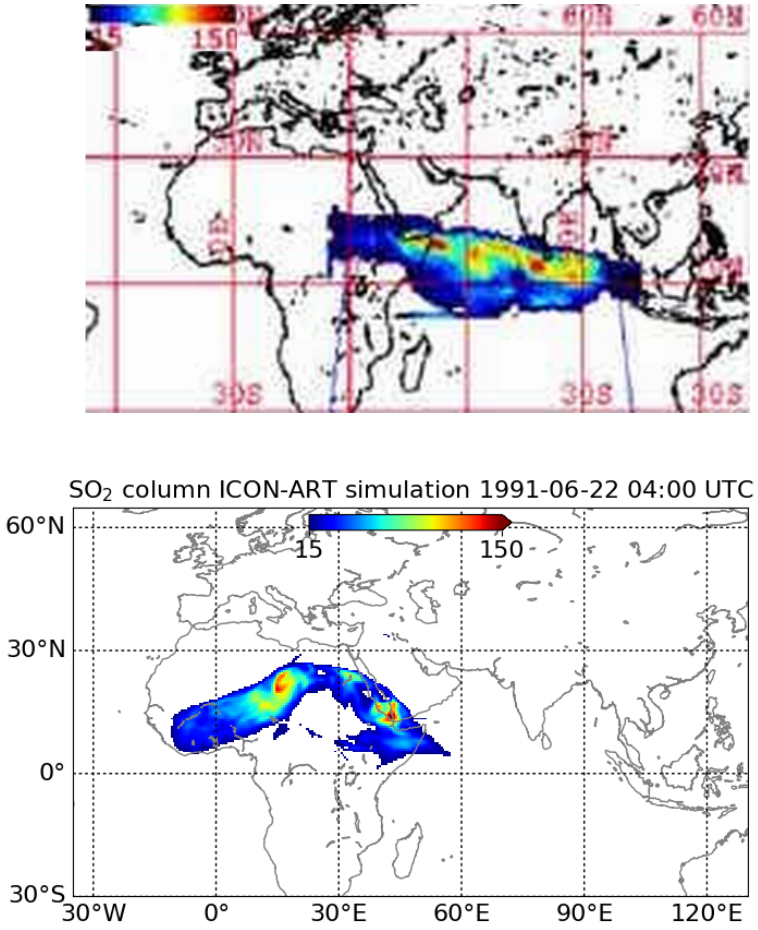

Figure 5.4: TOMS SO_2 column in DU, June 22 1991, 08:34 UTC and 03:44 UTC (top) (Guo et al., 2004a). Simulated SO_2 column in DU with ICON-ART, June 22 1991, 04:00 UTC (bottom)

by the Quasi Biennial Oscillation (QBO) that during this time was in its easterly phase, and therefore encourages a southward transport but is not regarded in the ICON-ART simulation. Although the QBO is calculated in the ERA-Interim data (Shepherd et al., 2018) the QBO is not further calculated in the ICON-ART simulation.

5.1.2 Sulfate formation

In order to validate the particle formation of SO_4, the simulations will be compared with studies published by Aquila et al. (2012). This study simulated the dispersion of the Mt. Pinatubo plume with the GEOS-5 General Circulation Model used for atmospheric analysis, weather forecast and climate simulation and predictions. The model includes a solar and thermal radiation model, an explicit stratospheric chemistry, aerosol transport, chemical production of SO_4 and gravitational settling of aerosols. It does not include the QBO or the influences of aerosols on the stratospheric chemistry. The Mt. Pinatubo eruption is initialized with 20 Tg SO_2 between 16 km and 18 km. Figure 5.5 shows the published simulation results by Aquila et al. (2012) and figure 5.6 shows the ICON-ART simulation. When analyzing same pressure level, the ICON-ART simulation shows different horizontal distributions, due to different height distributions. The difference in height

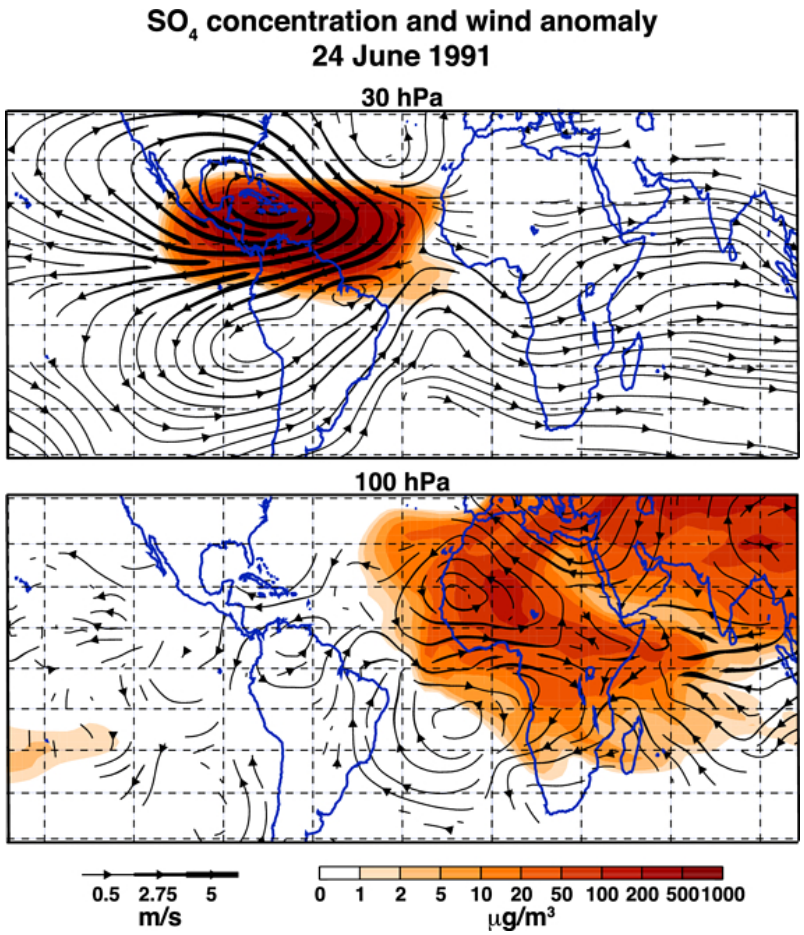

Figure 5.5: SO_4 concentration and wind anomalies induced by the aerosol radiative effects, according to Aquila et al. (2012). At the 24th of June 1991 in 30 hPa and 100 hPa

can be explained by the variety of initializations. The ICON-ART eruption is initialized between 15 km and 23.5 km, compared to 16 km to 18 km by Aquila et al. (2012).
Comparing figure 5.5 (30 hPa pressure level) to figure 5.6 (15 hPa pressure level), the SO_4 mixing ratio in the ICON-ART simulation is about 1.5 times higher than the results by Aquila et al. (2012). This might be driven by the calculated chemistry mechanisms. The GEOS-5 calculates an explicit stratospheric chemistry, but in this study's setup ICON-ART calculates a simplified OH chemistry, that is originally designed for the troposphere. One lack of this chemistry mechanism for this work is, that the only sinks of OH are given by CH_4 and CO, not SO_2. But regarding the huge amounts of SO_2 emitted, it should be a limiting factor for OH. The more OH is present, the more OH will react with SO_2 and further form additional SO_4 particles. The location of the aerosol plume in figure 5.5 (30 hPa pressure level) is more concentrated compared to figure 5.6 (15 hPa pressure level). The ICON-ART simulation shows a more zonal distribution reaching from West Africa to Central America, but a less meridional distribution. In terms of concentration magnitudes both simulations agree.
Comparing figure 5.5 (100 hPa pressure level) with either pressure level (30 hPa or 100 hPa) in figure 5.6, neither shows exact accordance. Due to the different height distributions the ICON-ART simulation shows about ten times lower SO_4 concentrations in

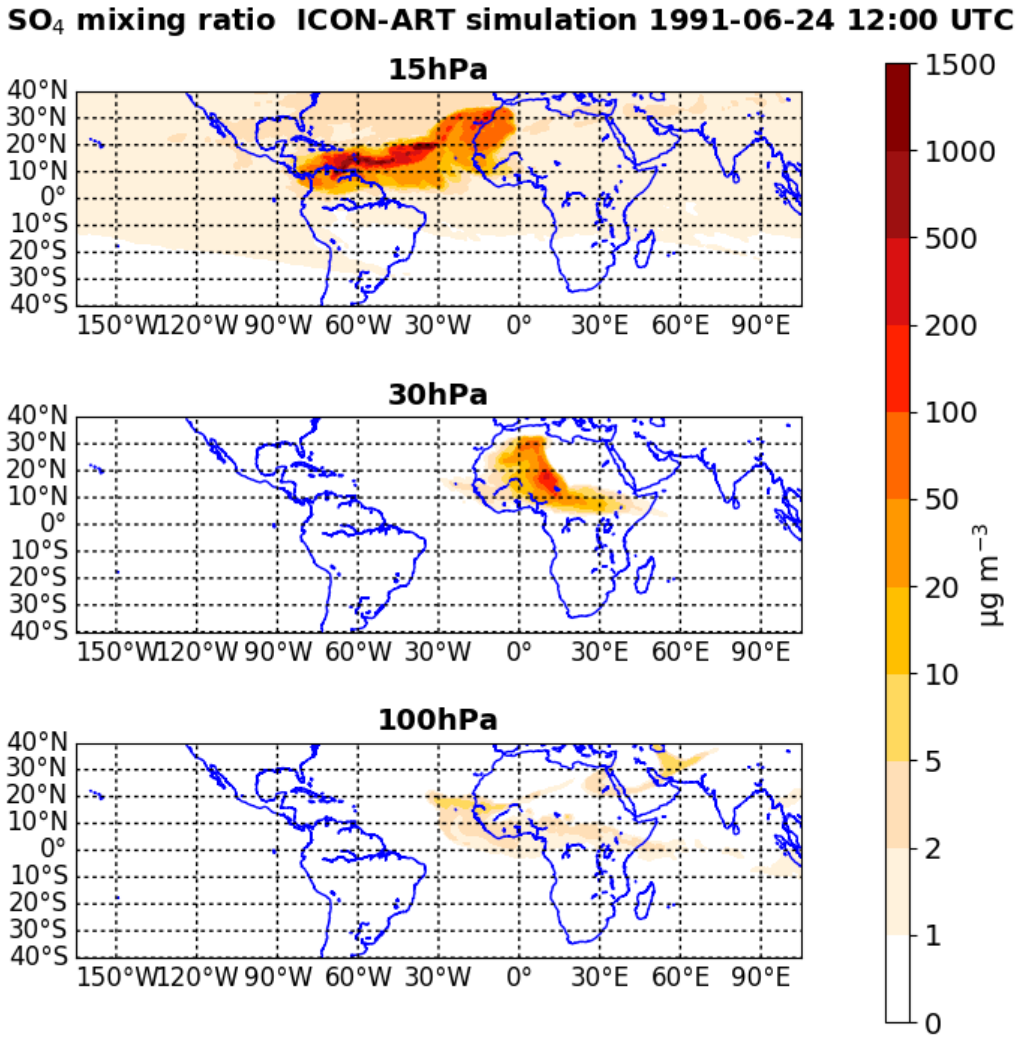

Figure 5.6: Simulated SO_4 with ICON-ART at the 4th of June 1991 at 12:00 UTC in 15 hPa, 30 hPa and 100 hPa

the 100 hPa level. The GEOS-5 simulation also shows a wider horizontal distribution spreading almost continuously over Africa and Western and South Asia. The eruption simulated with ICON-ART is also transported in these areas but not as uniformly. The aerosol plume in figure 5.5 (100 hPa) agrees in comparison with figure 5.6 (100 hPa) in concentration and distribution over western Africa, although the ICON-ART distribution is much more concentrated.

Nevertheless, besides the height differences, this comparison shows that ICON-ART simulation has the same order of magnitude in SO_4 concentration and the eruption plume spreads similar to the simulation done by Aquila et al. (2012), which is an agreeable validation.

5.1.3 Quantitative analysis of the sulfur aerosol radiative feedback

Independent of the deviation of the satellite data and simulation output discussed in 5.1.1 within the ten day simulation, it is important for this work to compare the newly im-

plemented radiative effects. This is done in the following. Ramachandran et al. (2000), analysed the "Radiative impact of the Mount Pinatubo volcanic eruption: Lower stratosphere response" by using the Geophysical Fluid Dynamics Laboratory SKYHI general circulation model (GCM) and doing a four-member ensemble of 2-year simulations. Because this work only simulated ten days after the eruption, only a quantitative analysis, that is independent from the exact location of the eruption plume, can be done.
Among others Ramachandran et al. (2000) states that:

(1) The long wave forcing of the SO_4 aerosol plume is positive and therefore warms the system.
(2) The solar forcing is negative and cools the system.
(3) The total net forcing is negative and therefore cools the system.

In the following the aerosol radiative effect of the eruption plume on the radiative fluxes is analysed. Therefore, the difference of the simulation case RAD minus case REF is calculated.
Figure 5.7 shows the difference (RAD-REF) of the long wave net flux as well as the SO_4 column in mg m^{-2}. The long wave spectrum in the model is defined by wavelengths from 4 μm to 100 μm and therefore does not consider the solar near infrared spectrum (wavelengths up to 2.5 μm). This means figure 5.7 considers only the terrestrial radiation. The four plots in figure 5.7 show the difference in long wave net flux at the surface and at the top of the atmosphere, both at daytime and at night. In total the difference is positive, meaning that in case RAD the system warms by long wave radiation, as stated in (1).
At the top of the atmosphere (plots (b) and (d)) the positive difference in the net flux is in good agreement with the SO_4 aerosol plume, outlined by the total column. As shown in figure 4.4 SO_4 absorbs long wave radiation very efficiently in either mode, so that the terrestrial radiation is absorbed by the aerosol plume in case RAD. Therefore less energy is radiated out of the system at the top of the atmosphere compared to case REF. This is defined as a positive change in the long wave net flux. The effect is independent from the diurnal cycle, because the Earth radiates constantly. Within the aerosol plume the maximum increase of the long wave net flux is up to 72 W m^{-2}. Nevertheless, the background noise reaches values over 200 W m^{-2}. This noise is induced by changes in cloud formation. ICON simulates the spreading of sound waves, and therefore small perturbations caused by the aerosol radiative effects affect the cloud formation. These perturbations can condition, that the cloud formation is slightly shifted. This further induces a negative difference where the cloud formed in case REF and a positive difference where the cloud formed in case RAD.
Regarding the same at the surface (plots (a) and (c)), changes in the long wave net flux correlating with the aerosol plume are only visible over land during the day (plot (a)). There the difference reaches values up to 39 W m^{-2}. This positive difference, means that in case RAD the net flux is increased. This increased net flux is most likely caused by a reduced irradiation. Sulfate particles, as displayed in figure 4.4, scatter ultraviolet

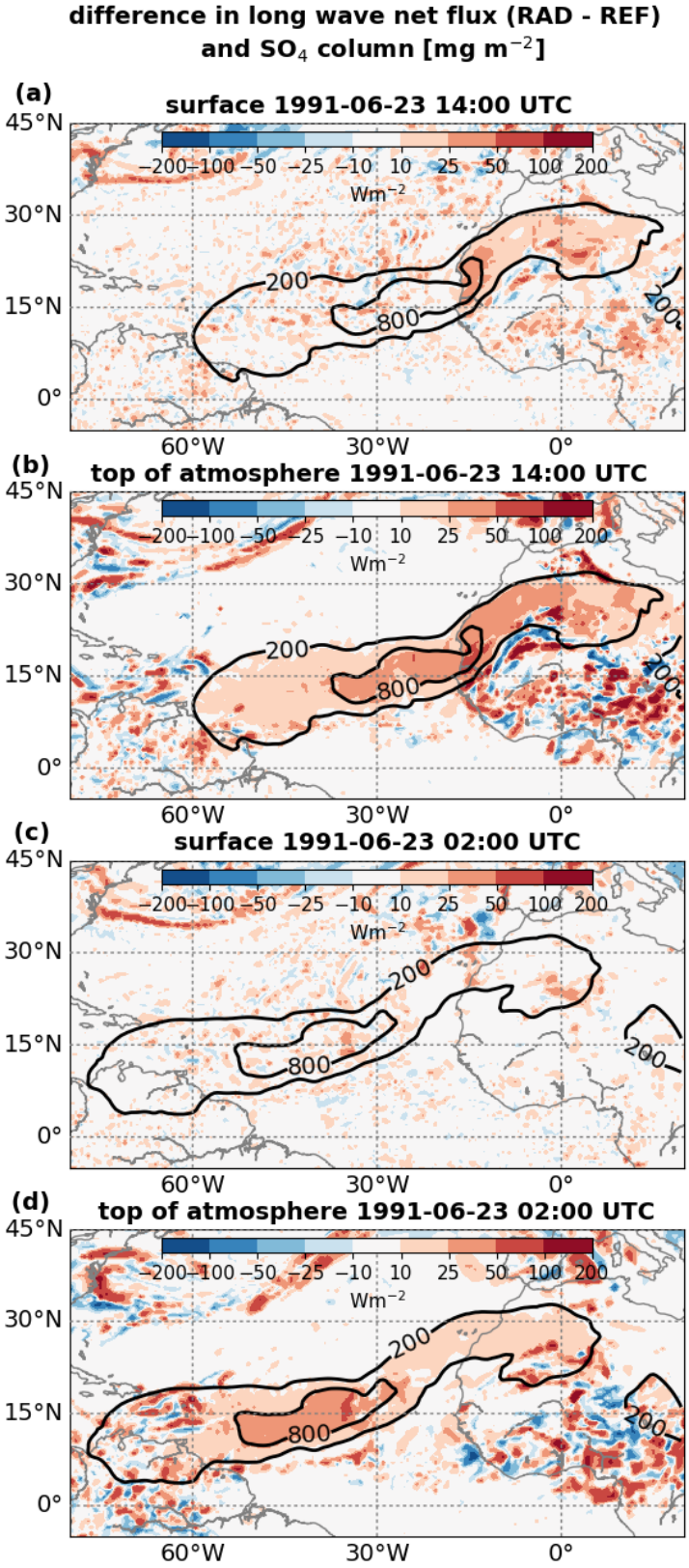

Figure 5.7: Difference of long wave net flux: case RAD - case REF and the SO_4 column in mg m^{-2}, at the surface and at top of the atmosphere. The upper two plots show the difference at the 23rd of June 1991 at 14:00 UTC (day) and the lower plots display the 24th of June 1991 02:00 UTC (night).

light efficiently, causing a cooling at the Earth's surface. Consequently, the long wave irradiation decreases. The Sahara surface and dust has a low heat capacity, which makes the Sahara long wave fluxes very sensitive to changes (Cook and Vizy, 2015) and for that reason makes this effect clear. The ocean with a significant higher heat capacity is not as sensitive to changes in radiation as the land surfaces.

As outlined, this difference in long wave radiation is due to the increased shortwave scattering and therefore an effect limited to the daytime, explaining why no effect is visible at night (plot (c)). In the given longitudinal-latitudinal section (80°W 20°E, 45°N 5°S) the mean difference in long wave net flux at the surface is 1.36 W m^{-2} compared to 3.43 W m^{-2} at the top of the atmosphere, therefore more than two times smaller.

As shown in figure 4.4 and discussed before, sulfur aerosols scatter shortwave radiation efficiently. Figure 5.8 displays the difference (RAD-REF) of the shortwave net flux, eight days after the eruption and during daytime. The net flux at the surface and the top of

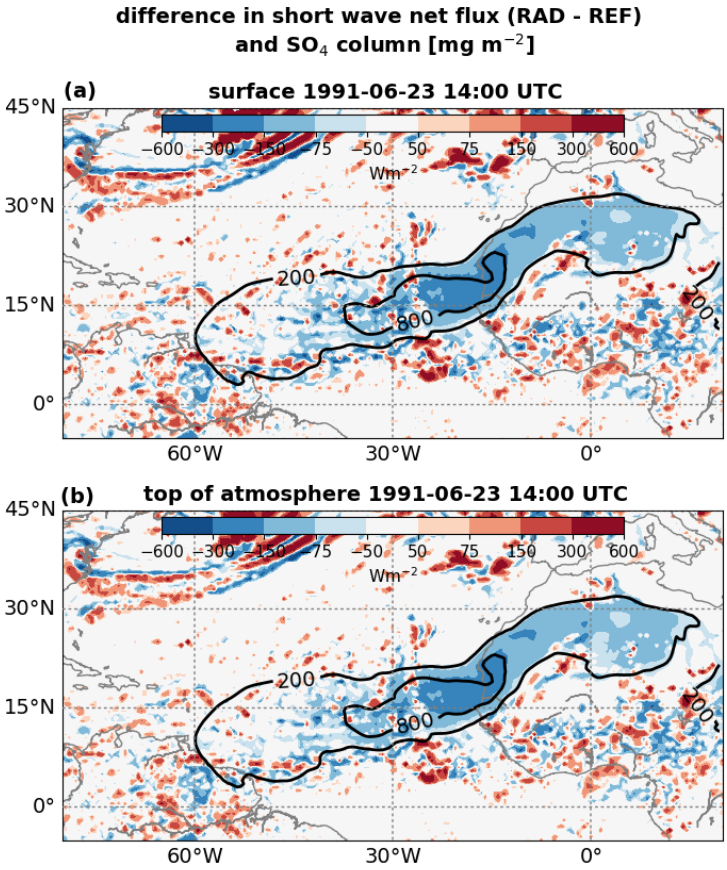

Figure 5.8: Difference of shortwave net flux: case RAD - case REF and the SO_4 column in mg m^{-2}, at the surface and at top of the atmosphere at 23rd of June 1991 14:00 UTC (day).

the atmosphere both show a negative forcing, correlating with the SO_4 aerosol column. The background noise is in the same size range and is in this case also caused by changes in cloud formation.

Due to the efficient scatter abilities of the sulfur aerosols in the shortwave, incoming solar

radiation is reduced at the surface (plot (a)), resulting in a negative forcing over -200 W m^{-2} that cools the system. The net shortwave forcing at the top of the atmosphere is also negative due to the amount of back scattered radiation and agrees with (2).

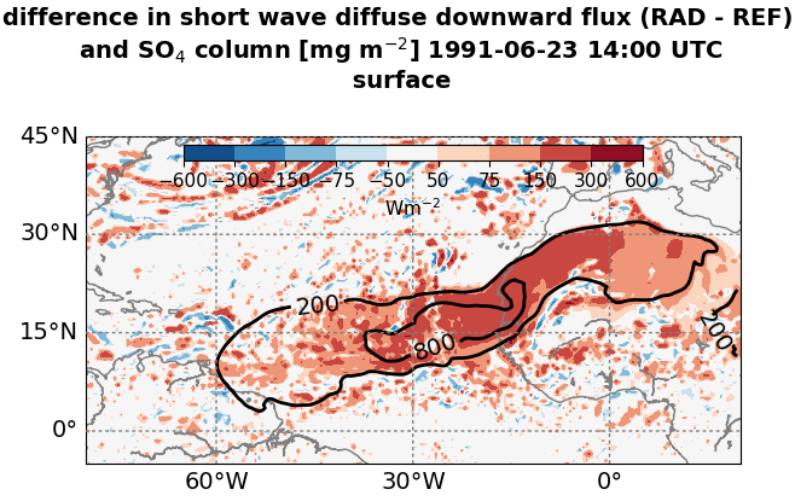

Figure 5.9: Difference of shortwave diffuse downward flux at the surface: case RAD - case REF and the SO_4 column in mg m^{-2} at 23rd of June 1991 14:00 UTC (day).

The scattering of solar radiation causes a reduction of the shortwave net flux but increases the diffuse radiation, as visible in figure 5.9, displaying the difference in shortwave diffuse downward flux at the surface. The area of increase in diffuse radiation in case RAD is in good agreement with the sulfur aerosol plume indicated by the SO_4 column. The aerosol scattering causes a forcing of up to 375 W m^{-2}. The background noise is in the same size range and is caused by differences in cloud formation.

Considering the total net flux in figure 5.10, the shortwave and long wave net fluxes have been added. The daytime plots ((a) and (b)) show that the negative shortwave forcing exceeds the long wave forcing during the day by up to 250 W m^{-2}. At night (plots (c) and (d)), with the lack of solar radiation, the total forcing is positive at the top of the atmosphere with up to 70 W m^{-2}. At the surface there is no significant change in net forcing during the day. The average forcing over day and night is with -16.9 W m^{-2} negative at the surface and negative at the top of the atmosphere with -14.53 W m^{-2}. This agrees with (3).

The changes in radiative fluxes indicate a warming of the aerosol plume by terrestrial long wave radiation. This warming takes mostly place in the lower stratosphere, where the aerosol plume is located. Due to the efficient scattering of solar or shortwave radiation the aerosol plume causes a reduced net forcing at the surface, which results in a cooling of the troposphere. These two effects are also described in Ramachandran et al. (2000) and therefore are a quantitative validation for the newly implemented radiative aerosol effects in the ICON-ART model.

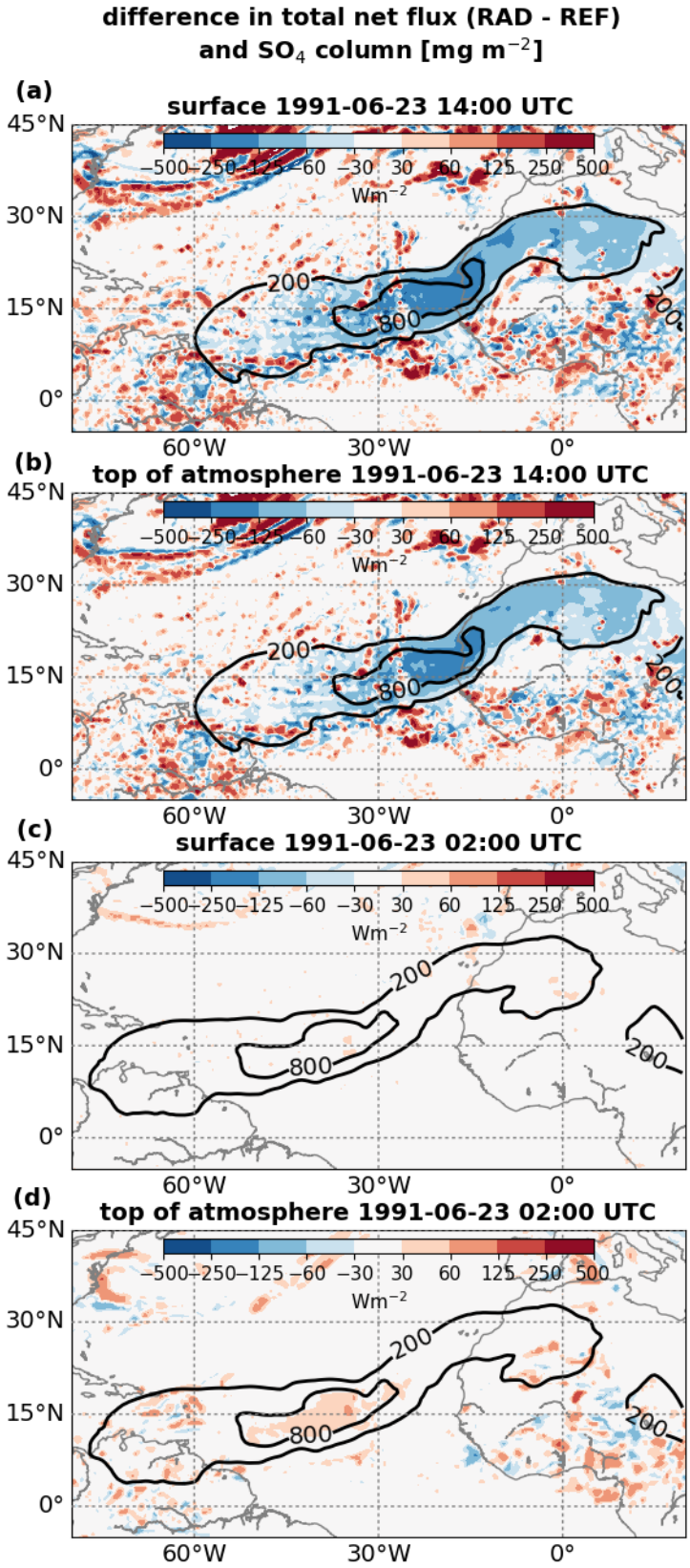

Figure 5.10: Difference of total net flux: case RAD - case REF and the SO_4 column in mg m^{-2}, at the surface and at top of the atmosphere. The upper two plots show the difference at the 23rd of June 1991 at 14:00 UTC(day) and the lower plots display the 24th of June 1991 02:00 UTC (night).

5.2 New particle formation

One objective of this thesis is the evaluation of new particle formation. In this setup of the Mt. Pinatubo eruption, in which insoluble ash and a gaseous tracer (SO_2) is emitted, the processes of interest are the nucleation of sulfate particles and the condensation on and coagulation with existing particles. As explained in section 2.2, SO_2 reacts to H_2SO_4

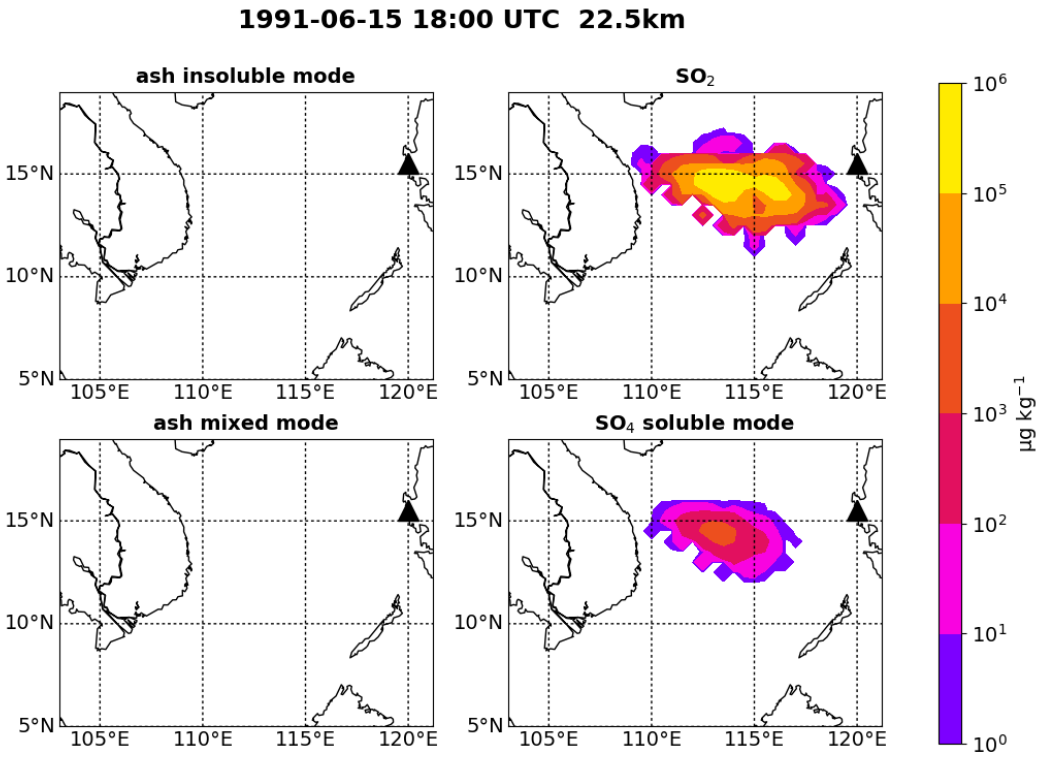

Figure 5.11: Mass mixing ratios of the ash insoluble mode, SO_2 , ash in the mixed, mode and SO_4 in the soluble mode 12 hours after the eruption at 25.5 km. The black triangle marks the location of Mt. Pinatubo.

that can then nucleate or condensate on existing particles. Figure 5.11 and 5.12 show the mass mixing ratios of ash in the insoluble and mixed mode, the SO_2 and the SO_4 12h after the eruption has started.

Displayed in figure 5.11 are the same mass mixing ratios in 25.5 km height. There the mass mixing values for ash in each mode are up to seven orders lower than SO_2 and SO_4, because ash is only emitted up to a height of 19 km. The lack of existing ash particles, with comparably low concentrations of 0.2 μg kg^{-1} in the insoluble mode and 0.4 μg kg^{-1} in the mixed mode, on which H_2SO_4 can condensate allows nucleation. The SO_4 particles in figure 5.11 and 5.12 are solely soluble particles nucleated from gaseous tracers. The special offset from the volcano to the eruption plume is larger for the sulfate particles than the sulfur dioxide and can be explained by the time it takes for the particles to form. Overall the shape of the SO_4 plume and the SO_2 plume are in good agreement. The SO_2 mixing ratio peaks at 4.12×10^5 μg kg^{-1} and the SO_4 at 1998.1μg kg^{-1}. The peak of the sulfur plume lays within the peak of the SO_2 plume, which further shows the correlation.

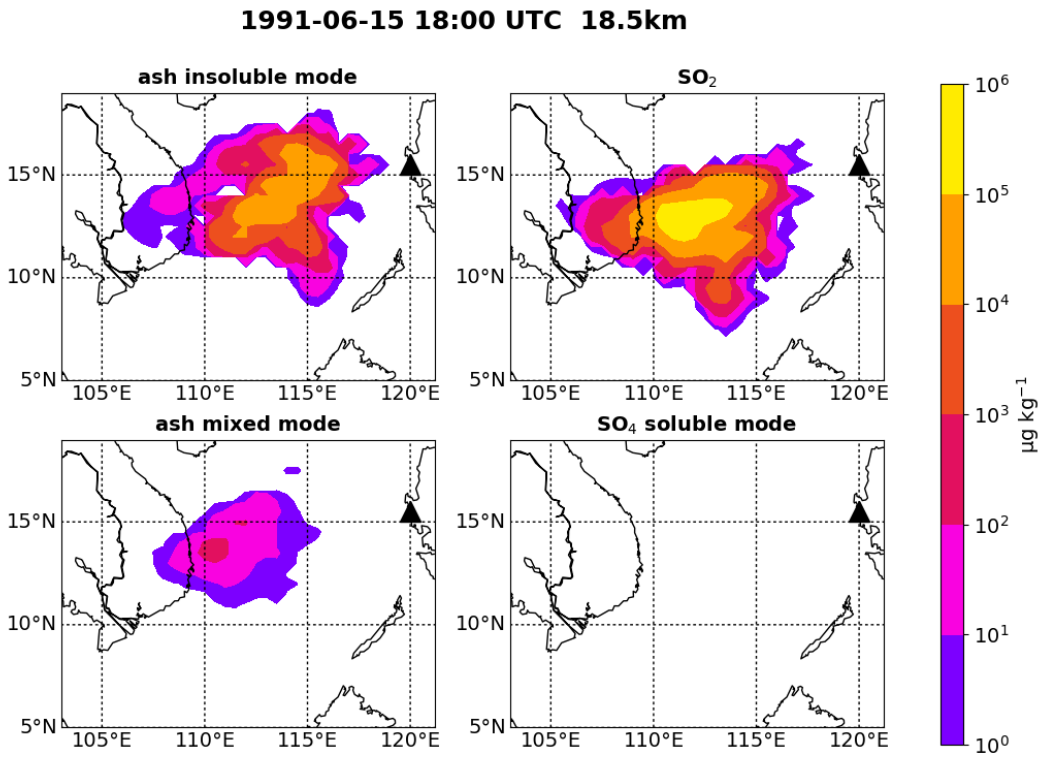

Figure 5.12: Mass mixing ratios of the ash insoluble mode, SO_2 , ash in the mixed, mode and SO_4 in the soluble mode 12 hours after the eruption at 18.5 km. The black triangle marks the location of Mt. Pinatubo.

Figure 5.12 displays the same tracers but in 18.5 km height, where insoluble ash is also emitted. The highest mixing ratio has SO_2 with a peak value of 1.93 $\times 10^5$ μg kg^{-1}. This maximum is less than half of the maximum value in figure 5.11. The insoluble ash mixing ratio reaches values up to 9.90 $\times 10^4$ μg kg^{-1}. In this height there are hardly any soluble sulfur particles present, displayed by comparably low concentrations of maximum 0.2 μg kg^{-1}. That condensation or coagulation is taking place is also outlined by the aged ash mixing ratio, that reaches values up 140.3 μg kg^{-1}. Particles are switched from the insoluble mode to the mixed mode when more than 5% of the mass is soluble.

5.3 Temporal evolution of total aerosol mass

For better understanding of the formation process, the total mass within the equatorial belt (35 °N and 35 °S) is calculated and its temporal evolution is displayed in figure 5.13. The first focus is on the formation process. The radiative effects will be discussed later.
The total mass of SO_2 in the equatorial belt is displayed in figure 5.13 (a) up to ten days after the eruption. In the first six hours the 18 Tg SO_2 are emitted. This is visible in the steep increase peaking at 19.2 Tg seven hours after the eruption started. After the peak the SO_2 total mass decreases in mean with 2.34×10^{10} g per hour in case RAD and with 1.30×10^{10} g per hour in case REF.
In the second plot figure 5.13 (b), the SO_4 soluble Aitken mode is displayed. Other than

the SO_2, the SO_4 Aitken mode total mass has no steep increase during the eruption. In this plot 24 h steps are visible for both runs, indicating a diurnal cycle. Looking at the 24 h steps the total mass increases up to 3.78 Tg, 178 h after the eruption in case RAD and up to 2.29 Tg, 151 h after the eruption in case REF. After the peaks, the total mass decreases, which means that more particles get shifted out of the mode than new particles are being formed. Even after the peak the diurnal signature can still be observed.
In figure 5.13 (c), the total mass of SO_4 in the accumulation mode is displayed. The total mass increases slowly in the first 72 h with an increase in the order of 10^8 g h^{-1}, compared to ca. 2.5 Tg h^{-1} further on. In case RAD there is a further, even steeper increase with 4.4 Tg h^{-1} 168 h after the eruption. Considering the total mass of SO_4 in the Aitken mode, one can see that the flattening of the Aitken mode correlates with the increase of the accumulation mode's total mass. This indicates a mode shift from the Aitken to the accumulation mode.
In figure 5.13 (d) the total mass of insoluble ash is shown. In total 100 Tg are emitted in six hours, which can be observed in the steep increase of the graph. Six hours after the eruption started the maximum of 104 Tg total mass in the equatorial belt is reached. Despite the quick rise the insoluble ash mass decreases within 15 hours to concentrations in the order of 10^{12}g. After that, poorly visible the concentrations continuously decrease, with 4.24×10^9 g h^{-1} in case RAD and 5.54×10^9 g h^{-1} in case REF.
The bottom plot in figure 5.13 (e) outlines the total mass of the ash in the mixed mode. Three hours after the eruption started the mixed ash mass grows up to 2.00×10^{10} g in case RAD and 8.04×10^9 g in case REF. Both runs peak 16 hours after the eruption started and then decrease with 1.26×10^7 g h^{-1} in case RAD and 1.13×10^8 g h^{-1} in case REF. The temporal offset is caused by the time it takes for the particles to form. The formation only takes place in the first 16 h, in which ash in the insoluble mode is still present in large amounts. In contrast to the insoluble ash, the ash in the mixed mode is three orders of magnitude lower, when it peaks in the first 24 hours, but two orders of magnitude higher after three days.
In terms of radiation the SO_2 decays faster in case RAD, when aerosol radiative effects are calculated (figure 5.13 (a)). The difference reaches over 2.1 Tg after 10 days. The gray difference line displays 24 h steps outlining a diurnal cycle.
The SO_2 difference is consistent with the positive differences in the SO_4 concentrations, which in total (Aitken plus accumulation mode) increases over time. Since SO_4 is not only formed by SO_2, the total SO_4 difference is 1.54 Tg higher than the SO_2 difference.
Looking at the Aitken mode (figure 5.13 (b)) the maximum difference appears about 180 h after the eruption with 1.74 Tg. Afterwards the concentration in in case RAD decrease and align with case REF. Reasons for these differences will be discussed later.
Within the accumulation mode (figure 5.13 (c)), seven days after the eruption, the RAD-REF differential of total mass reaches up to 3.27 Tg while correlating negatively (in quantity) with the Aitken mode differential. The more particles are present in the Aitken mode, the more can be shifted into the accumulation mode, which causes the difference to increase. Since the differences do not match qualitatively (the accumulation mode difference is 1.9 Tg higher), the radiative effect of aerosols must also lead to increased condensation.

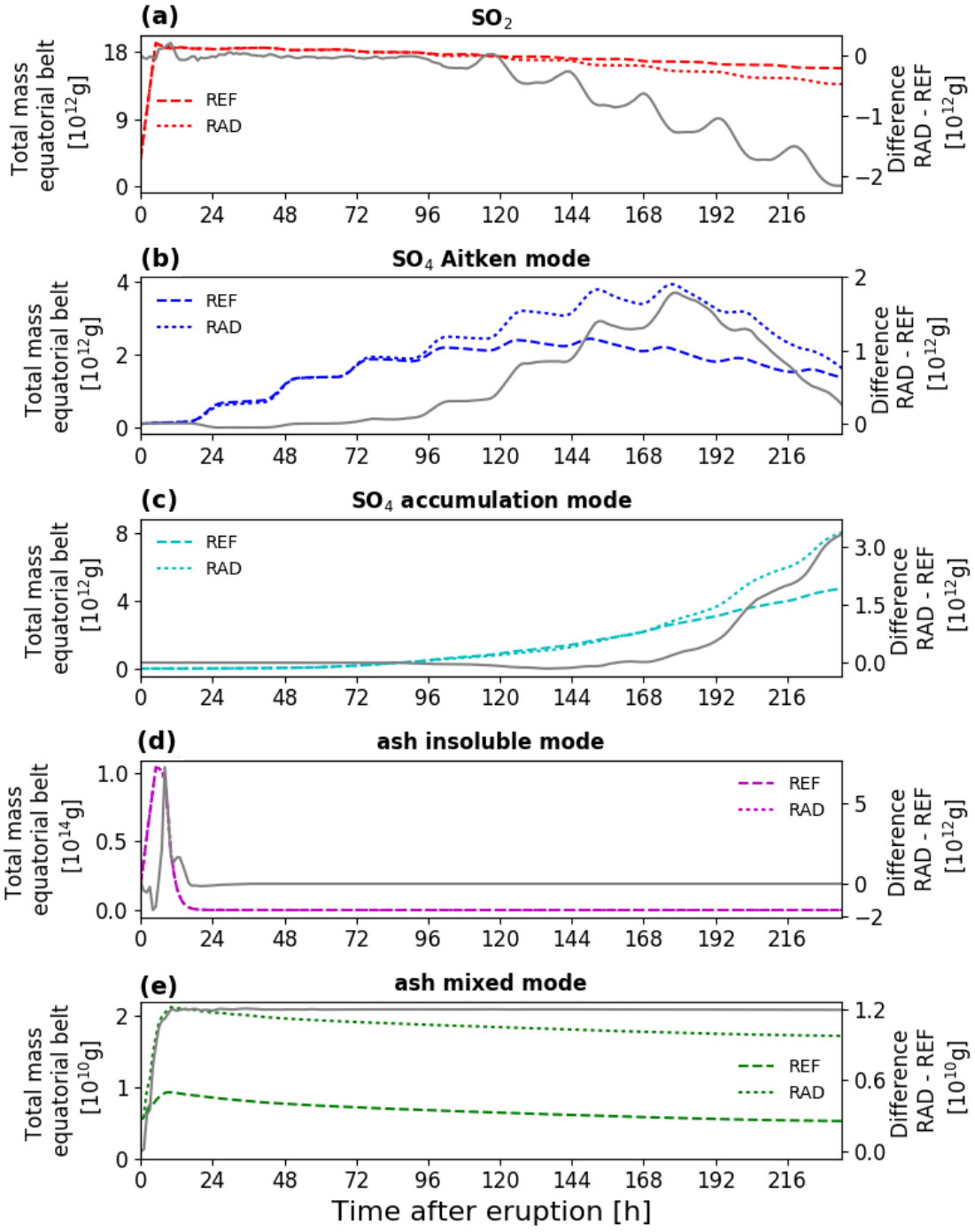

Figure 5.13: Temporal evolution of the total SO_2, SO_4 Aiken mode, SO_4 accumulation mode, ash insoluble mode, ash mixed mode mass calculated within the equatorial belt (35°N and 35°S) after the eruption. The dashed line indicated the simulation without radiative aerosol effects (case REF), the dotted line indicates the simulation calculating radiative effects of volcanic aerosols (case RAD) and the grey line displays the difference between both runs(RAD-REF).

The difference of case RAD and case REF in figure 5.13 (d) for insoluble ash, is two orders of magnitude lower than the total mass. During the eruption (first six displayed hours) the difference is negative up to -1.42×10^{12} g, meaning, that the total mass in case REF is higher. Two hours after the eruption finished, the total mass in case RAD is higher than

case REF, reaching a maximum difference of 7.15×10^{12} g. The difference declines in line with the total mass concentration and is small after 20 h. In the beginning of case REF the total insoluble ash mass is higher than in case RAD. This correlates with an increased formation of mixed ash in case RAD. In addition, the difference in the insoluble mode is about two orders of magnitude higher than in the mixed mode and therefore can not explain this alone.
In figure 5.13 (e), the difference between case RAD and case REF for the ash in the mixed mode develops between three and 12 hours after the eruption started, which correlates with the time in which ash and SO_2 are still in large amounts present. The difference stays constant around 1.2×10^{10} g.
Regarding the differences between both cases, in case RAD the particle formation is stronger. This is first visible in the SO_4 Aitken mode and further in the accumulation mode and in the formation of mixed mode ash articles.

5.4 Lifting of aerosol plume due to aerosol radiative effects

A further aspect of this thesis is to show how radiation effects the dynamics of the volcanic aerosol plume. As shown in Aquila et al. (2012), the radiative effects of aerosols induce a self-lofting of the eruption plume. To analyse this effect figure 5.14 displays the temporal evolution of the mass weighted height of the aerosol plume of the respective aerosol type. To calculate the mass weighted height of the aerosol plume the center of the mass formula is used:

$$z_s = \frac{\sum_n z_n m_n}{\sum_n m_n} \tag{5.1}$$

In this case z_s is the mass weighted height of the aerosol plume, n is the number of grid cells, in which the aerosol concentration exceeds the threshold to be classified as an aerosol plume, caused by the eruption. z_n and m_n are the height and the aerosol mass concentration in the respective grid cell.
For the soluble Aitken mode a threshold of 25 μg kg^{-1} is chosen. The result is shown in figure 5.14 (a). The red line displays case RAD, which considers the radiative aerosol effects, the blue line displays case REF, not considering the aerosol radiative effects. And the grey line shows the height difference between the both cases. In both simulations the aerosol plume starts with a mass center at around 22 km. In case REF z_s is relatively constant with 22.8 km, but slowly decreasing with approximately 1 m per hour. In case RAD a rise of the aerosol is visible, especially after 72 hours. After that the mass center of the SO_4 soluble Aitken mode rises with about 35 m per hour reaching a maximum height of 28.92 km at the end of the simulation. This leads to a maximum difference of 6.78 km in z_s and indicates the self-lofting of the eruption plume induced by the radiative aerosol effect. In case REF slow sedimentation is indicated by a decrease of the z_s.
As discussed in section 5.3 it takes a certain time for the accumulation mode particles to form. The aerosol plume reaches the chosen threshold of 30 μg kg^{-1} in case REF 48 hours

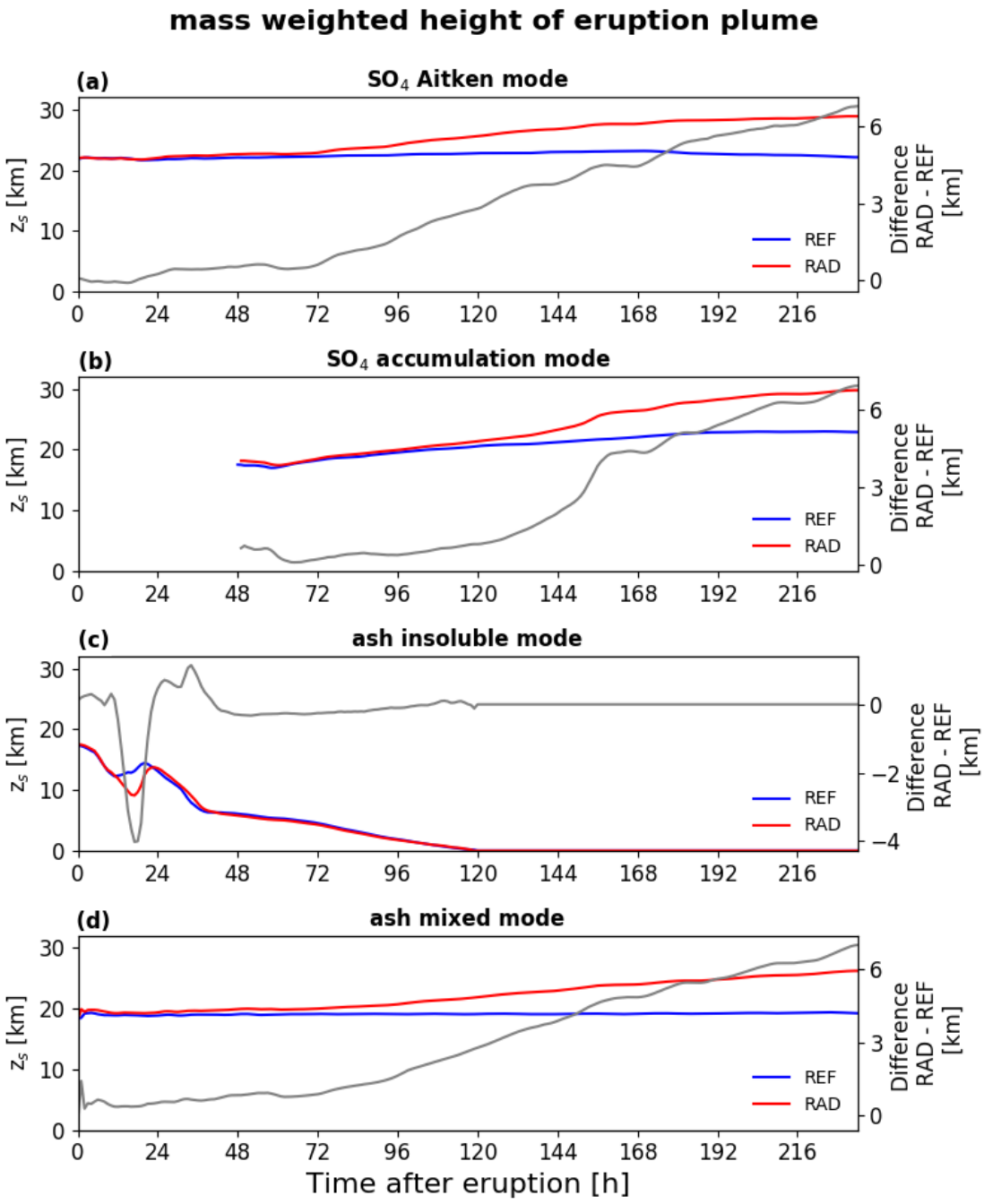

Figure 5.14: Temporal evolution of z_s of the eruption plume. Displaying SO_4 in the Aitken and accumulation mode and ash in the insoluble and mixed coarse mode after the eruption. The blue lines indicate the simulation without radiative aerosol effects (case REF), the red lines indicate the simulation calculating radiative effects of volcanic aerosols (case RAD) and the grey line the height difference between the (RAD-REF).

after the eruption with a z_s that equals 17.5 km and in case RAD after 50 hours with a z_s equal to 18.0 km and therefore around 500 m higher. z_s of the SO_4 accumulation mode plume increases over time. In case RAD (red line) with an average of 75 m per hour and in case REF (blue line) with 32 m per hour. Therefore the radiative effects induce a lifting twice as strong, resulting in a maximum difference of 6.38 km after 220 h. The rise of

both plumes indicates that increased particle formation takes place in the upper levels.
Regarding z_s of the insoluble ash in figure 5.14 (c), with a threshold of 0.007 μg kg^{-1}, the plot shows, that in contrast to the other aerosol plumes the insoluble ash plume is sinking in both cases. After the eruption z_s is in both cases similar with 17.36 km in case REF and 17.48 km in case RAD. In case REF z_s decreases down to 12.33 km for eleven hours and then increases for eight hours up to 14.48 km, before reaching the ground with 115 meters per hour after 120 hours. In case RAD z_s decreases down to 9.07 km within 16 hours, then increases up to 13.60 km 22 hours after the eruption and reaches zero 119 h after the eruption. The largest difference between both runs is between 11 and 12 hours after the eruption, reaching -4.02 km.
For the ash in the mixed mode a threshold of 0.01 μg kg^{-1} is chosen. For this threshold z_s starts for case REF with around 18.4 km and increases in mean with 1 m per hour. Case RAD starts with a z_s of around 19.5 km, and is therefore 1.1 km above, indicating that in case RAD the mixed particles are already formed in higher altitudes. During the first six hours after the eruption, while ash is still emitted, the heights vary. In case RAD z_s increases with 33.3 meters per hour, reaching a maximum height of 26.25 km at the end of the simulation, which is 6.99 km higher than in case REF. Similar to the z_s in the SO_4 Aitken mode the difference steeply increases after 72 hours, outlining an aerosol radiative effect, which induces the self-lofting.
Figure 5.15 displays the differences in mean mixing ratio (case RAD - case REF) within the equatorial belt, in order to give a more spacial resolved analysis of the changes induced by the radiative aerosol effect. The red contours indicate a positive difference, meaning, that case RAD contains higher concentrations. The blue contours indicate a negative difference, meaning case REF contains higher concentrations.
Figure 5.15 (a) displays the temporal evolution of differences for the SO_4 soluble Aitken mode. After 80 h the positive mean difference in a height of around 23 km is larger than 0.5 μg m^{-3} and increases over time and height for about 100 h. Afterwards the positive difference deceases. After 86 h a negative difference of -0.5 μg m^{-3} in a height of 20 km is reached, which further decreases with time, but not with height for about 75 hours. The positive difference in the upper levels indicates an uplift of the aerosol plume due to the aerosol radiative effects as also discussed in figure 5.14. The increasing differences over time indicate a further particle formation. The negative difference in the lower levels indicate a particle loss in case RAD, which underlines the uplift. With 3.07 μg m^{-3} maximum positive difference is more than twice as high as the negative difference with 1.47 μg m^{-3}. This could mean, that either more particles are formed in case RAD and/or there are still particles forming and being present in case RAD in the lower altitudes.
Regarding the differences in figure 5.15 (b), showing the accumulation mode, the displayed differences are only positive reaching a maximum value of 216.24 μg m^{-3}. The difference reaches values above 65 μg m^{-3} eight days after the eruption in 29 km and further increases with height and time. The negative differences reach values up to -19.37 μg m^{-3}, although not displayed in the plot. This shows that there is an uplift, although the positive difference outdoes the negative. Taking figure 5.13 to account, the high differences are caused by an increased particle formation in the accumulation mode in case RAD. The increase in the

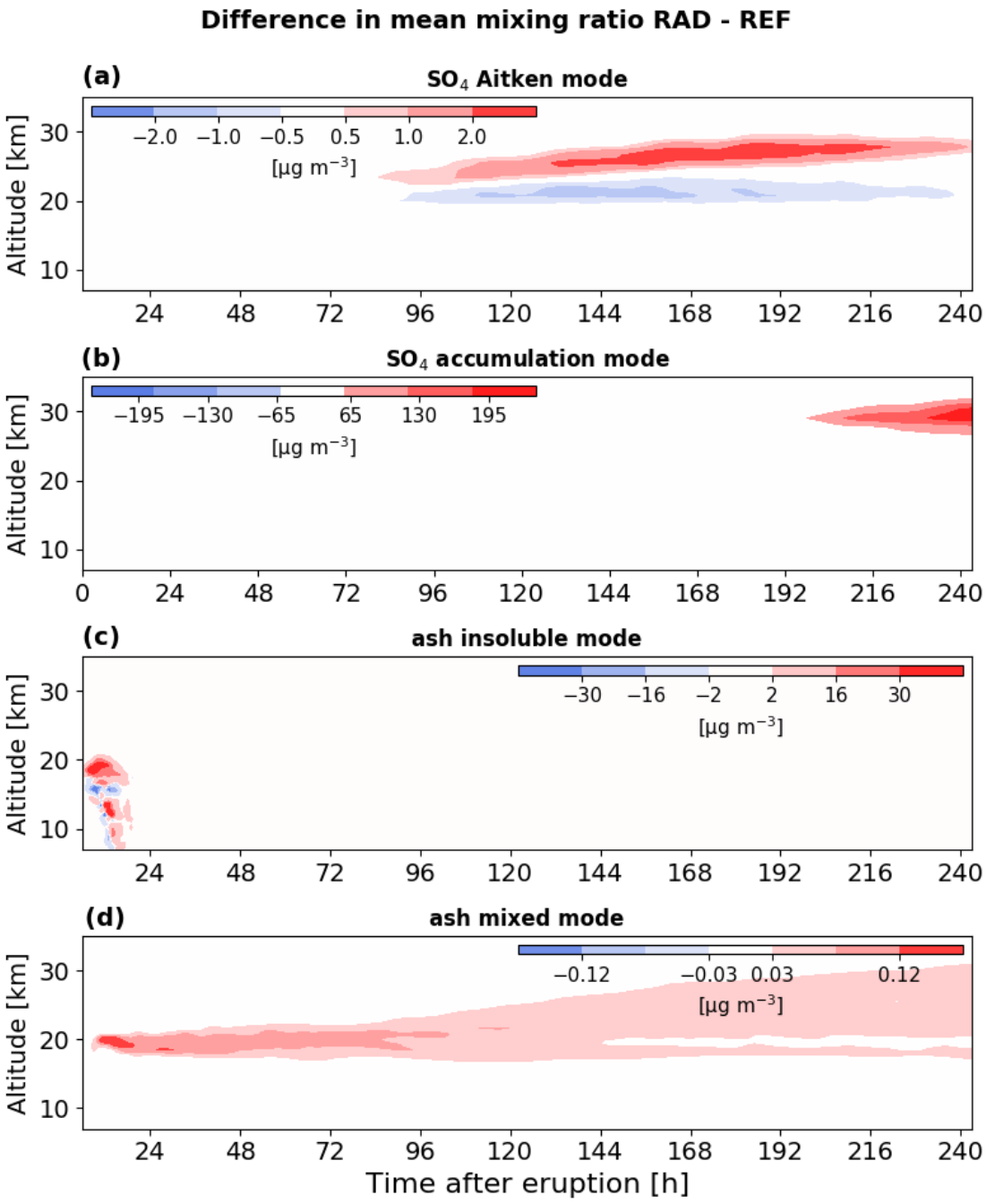

Figure 5.15: Temporal evolution of the mean mixing ratio difference in μg m^{-3} case RAD - case REF of SO_4 in the Aitken and accumulation mode and ash in the insoluble and mixed coarse mode calculated within the equatorial belt (35°N and 35°S) after the eruption.

accumulation mode correlates with the decrease in the Aitken mode concentration. This effect can also be seen in figure 5.13 and further outlines a shift from the Aitken into the accumulation mode.

Figure 5.13 (c) shows the average mixing ratio difference of the insoluble mode. Since the insoluble ash sediments quickly, changes are only detectable within the first 24 h. The structure of the insoluble ash is more complex than for SO_4, with positive differences of

up to 63.53 μg m^{-3} and negative ones of up to -77.41 μg m^{-3}. The negative differences are up to 20% higher than the positive differences. Above 16 km the differences are manly positive, so the concentrations in case RAD are higher, indicating an uplift. This is also shown by the negative difference between 16 and 14.5 km. Below that, differences are rather dependent on time than on height. Lower concentrations in case RAD four to six hours after the eruption and higher concentrations six to 19 hours after the eruption, indicate longer lifetimes for ash in the insoluble mode in case RAD in contrast to case REF.

Figure 5.15 (d) shows the differences in mean mixing ratio of ash in the mixed mode. Displayed is only a positive difference, because as shown in figure 5.13 the total mass of ash in the mixed mode within the equatorial belt is about twice as high in case RAD. With a maximum positive difference of 0.268 μg m^{-3} and a negative of -0.006 μg m^{-3} the positive difference is up to two orders of magnitudes higher. The plot shows the highest differences between four and 15 hours after the eruption, during the formation process, as described in section 5.3. Afterwards the formed mixed ash also experiences an uplift. The constant lower edge of the aerosol plume at a height around 17 km and the decrease in concentration over time, indicates that the ash mainly diffuses, rather than new particles form.

5.5 Changes in temperature

As shown in section 5.1.3, the SO_4 plume absorbs long wave radiation effectively. The absorption of radiation must result in a change of temperature. To further analyse this

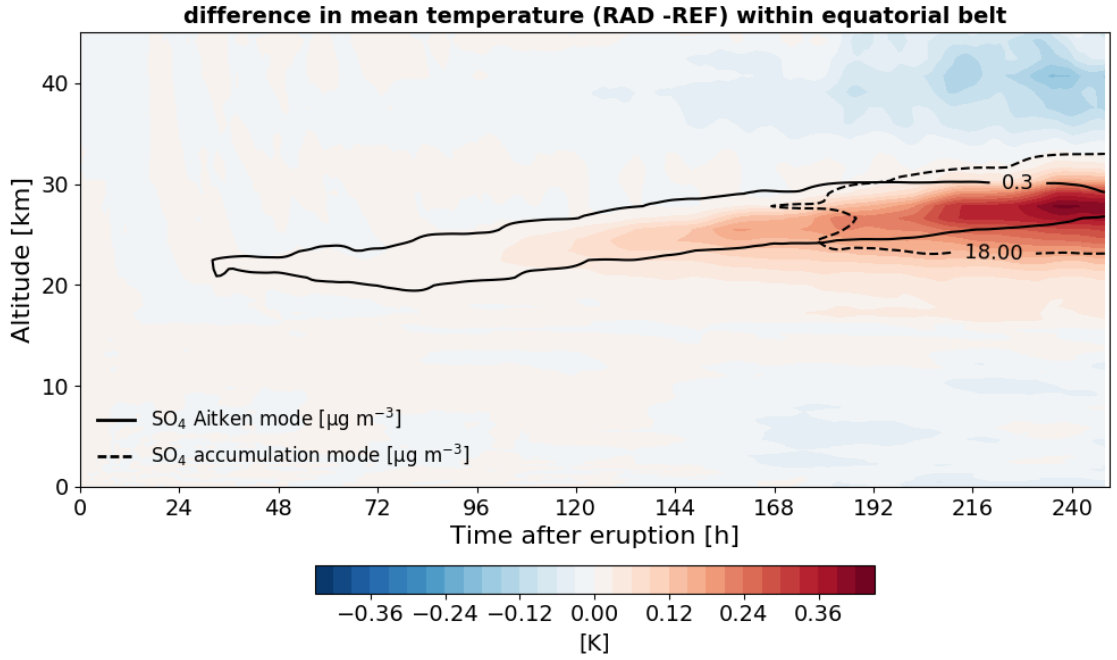

Figure 5.16: Temporal evolution of the mean temperature difference in Kelvin (RAD-REF) within the equatorial belt 35°N and 35°S) and SO_4 in the Aitken and accumulation mode in μg m^{-3} (case RAD).

the mean temperature within the equatorial belt is calculated and displayed in figure 5.16. To outline the correlation of temperature change with the aerosol plume the mean mixing ratio in μg m^{-3} for SO_4 in the soluble Aitken mode (solid black line) and the soluble accumulation mode (dashed black line) is given.
Twenty four hours after the eruption the mean temperature difference between 19 km and 23 km shows a positive difference, meaning that the temperature is higher in case RAD. The effect is small with only up to 0.03 K, but since it is in the same altitudes as the SO_4 aerosol plume, it can be interpreted as a warming induced by the aerosol radiative effect. The temperature in case RAD further increases over time, reaching a maximum difference of 0.42 K. At the end of the eruption, the area of increased temperature reaches from 16 km to 30 km altitude and correlates with the SO_4 aerosol concentration.
Five days after the eruption, above the aerosol plume the temperature difference is negative. Therefore is case RAD cooler than case REF. This cooling reaches an average decrease up to -0.19 K and is less than half of the maximum warming. After six days, the air below the radiative warming in the lower stratosphere is cooling down. The effect is with up to 0.06 K small.
Averaging over the whole equatorial belt gives a quantitative understanding of the temperature changes induced by the aerosol radiative effects. In order to get a more qualitative inside, the mean temperatures of the eruption plume in case RAD and REF are calculated and compared in figure 5.17. It is differed between the SO_4 eruption plume (Aitken + accumulation mode) and the ash plume, because of the different distributions and altitudes. Due to the quick sedimentation of insoluble ash, the mixed ash is taken as reference. The area of the eruption plume is defined as the area in which the SO_4 concentration reaches values over 30 μg kg^{-1} and respectively 0.001 μg kg^{-1} for the ash plume. Every hour the mean temperature of all grid points, which reached the threshold is calculated for case RAD, and the same grid points are also used for case REF. The result is displayed in figure 5.17. The same grid points are used to extract the aerosol radiative effect from possible temperature difference due to different locations, especially in altitude.
The red lines show the mean temperature for case RAD, the blue lines for case REF and the grey lines display the difference between both runs.
The sulfur plume in figure 5.17 starts with an eruption plume mean temperature of 212.7 K, the mean temperature then decreases down to a minimum value of 203.1 K (case RAD is in average 0.02 K warmer). Afterwards the mean temperature rises reaching a maximum temperature of 227.6 K and 226.9 K in case REF at the end of the simulation. The temperature rises in both cases. This can be explained with the self-lofting of the aerosol plume in warmer environments.
The aerosol radiative effect can be observed in the difference (RAD-REF) displayed with the grey line. Up to 56 hours after the eruption started, the difference varies between -0.36 K and 0.11 K, but is in mean -0.01 K, with no significant trend. After that, the difference rises, with an average of 0.005 K per hour. The maximum difference is after eight and a half days with 0.94 K. After five days there are 24 hours oscillations visible, indicating a diurnal cycle.
The ash plume mean temperature rises from 195.6 K at the beginning of the eruption

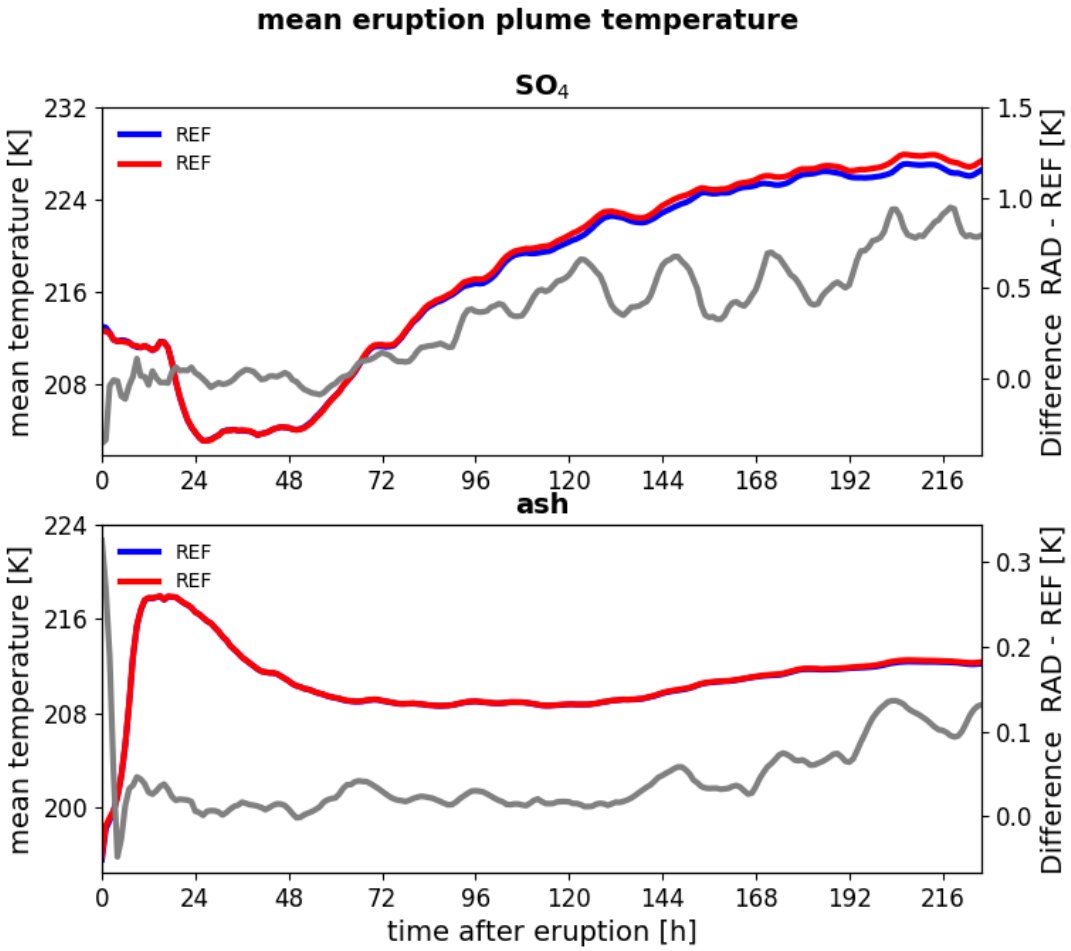

Figure 5.17: Temporal evolution of the mean temperature of the SO_4 plume (top plot) and the ash plume (bottom plot) in Kelvin case RAD (red line), case REF (blue line) and the difference (RAD-REF) in grey.

up to 218.2 K 15 hours after the eruption. Then, the mean temperature decays down to 208.9 K about two and a half days after the eruption. Six days after the eruption the mean plume temperature rises again up to 212.4 K. The temperature difference are rather small, compared to the SO_4 plume temperature. The mean difference is 0.005 K and the maximum difference is 0.33 K at the beginning of the simulation. Besides the largest difference, that occurred during the eruption, the difference increases again after six days and correlates with the mean rise in temperature. The differences again show a diurnal cycle.

6 Discussion

6.1 Particle formation

As section 5.2 shows, the soluble particle formation is predominant in higher altitudes, at least during the first 12 h after the eruption. The particles form by nucleation, as the correlation between figure 5.13 and 6.1 (will be discussed in the following section 6.2) shows. Nucleation describes the process of spontaneous cluster formation in a supersaturated environment. The probability of this happening rises with an absence of already existing particles, on which gases condensate and therefore reduce the substances available for nucleation. Furthermore, the saturation pressure for condensation is lower than for nucleation, implying, that the gases first condensate on pre-existing particles before nucleating. Therefore, in this simulation setup is nucleation is only possible above 19 km within the first 12 hours, where no ash is emitted.
Below 19 km the ageing of ash is detectable. As explained in section 4.3 coagulation and condensation lead to mixed phase particles, in this case ash and sulfur. Not only can the absence of soluble particles be interpreted as no nucleation occurring, but also the instant coagulation of the small nucleated particles with the coarse ash. The high mixing ratios indicate a high coagulation probability, which would underline this hypothesis. Although the predominance of ash particles on which sulfuric acid can condensate indicates that condensation represents the significant effect. The rapid sedimentation of insoluble ash limits the ageing process of ash as displayed in figure 5.13. This limitation allows increased sulfur formation 24 h after the eruption.

6.2 SO_2 to SO_4 conversion

In section 5.3 the decrease of the total SO_2 mass and the increase of the total SO_4 is described and displayed via figure 5.13. For SO_2 and SO_4 the detected diurnal cycle can be explained by the following process: during the day O_3 is photolysed and further OH is build. OH reacts with SO_2. The SO_2 reduction happens rather fast and the lifetime of OH is short, so that this reaction cannot take place during night, when no OH is build by photolytic reactions. The produced H_2SO_4 has a low saturation pressure, so that it nucleates and forms new small sulfur particles. Condensation on the existing Aitken mode particles leads to the growth of particle, that can further lead to a size shift from the Aitken mode to the accumulation mode. Coagulation with particles of different size modes also leads to mode shifts as explained in section 4.3.
The decrease in the Aitken mode total mass (figure 5.13) correlates with the increase in the accumulation mode total mass and indicates a mode shift. Even after the peak in

the Aitken mode a diurnal cycle is visible, indicating that nucleation is still taking place, although it is exceed by the mode shift.

To further investigate the mode shift, the total number concentrations of SO_4 in the soluble Aitken and the accumulation mode within the equatorial belt are analysed and displayed in figure 6.1. First, the curves show similar trends compared to the total mass in figure 5.13. This means, that for the Aitken mode the increase in mass correlates with the increase in number concentration and therefore implies, that new particles are formed in both cases (RAD and REF).

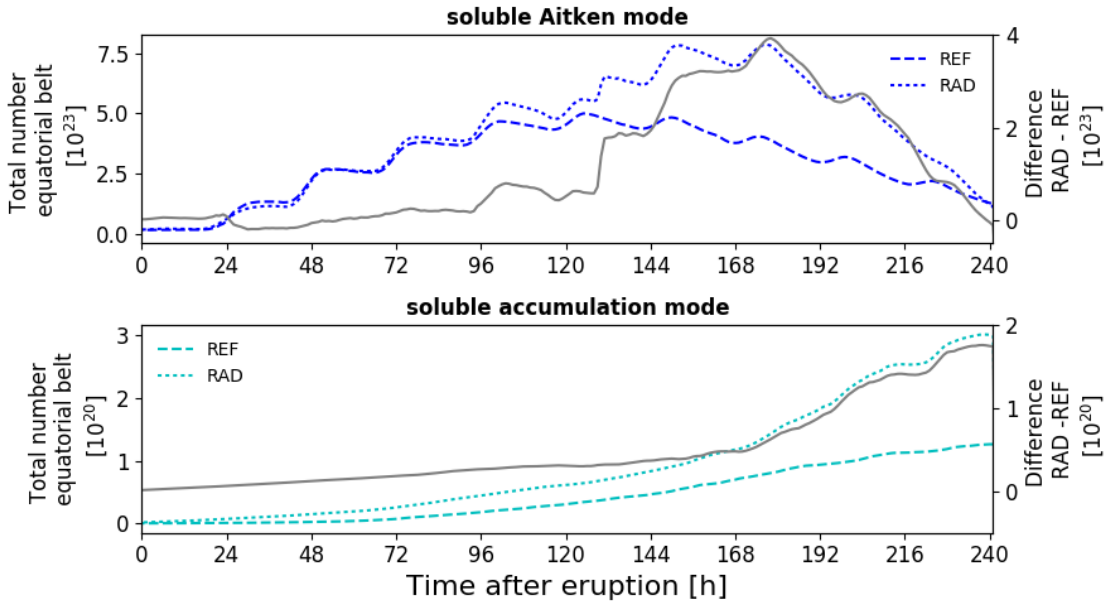

Figure 6.1: Temporal evolution of the total number of SO_4 Aiken mode and SO_4 particles calculated within the equatorial belt (35°N and 35°S) after the eruption. The dashed line indicated the simulation without radiative aerosol effects (case REF), the dotted line indicates the simulation calculating radiative effects of volcanic aerosols (case RAD) and the grey line displays the difference between both cases (RAD-REF).

Regarding the total mass the Aitken and accumulation mode are in a comparable size range (Tg), although the total mass of the accumulation mode reaches values twice as high as the Aitken mode. Looking at the total numbers of particles, the Aitken mode total number (values up to 7.9×10^{23} for case RAD and 5.0×10^{23} for case REF) is three orders of magnitude higher than the total numbers for the accumulation mode (with maximum values of 3.0×10^{20} in case RAD and $1.34\times10^{5}\mu$g kg^{-1} in case REF). The differences in total number, but not in total mass are due to the different size ranges of the modes. The Aitken mode with a median diameter initialized at 0.01×10^{-6} m is one magnitude smaller than the initialized median diameter of the accumulation mode with 0.2×10^{-6} m. This means, that in order to reach the same mass, more particles need to be present in the Aitken mode versus the accumulation mode.

Transferring this on a mode shift due to particle growth and coagulation, first would result in a number and mass increase in the accumulation mode, whereas coagulation only increases the mass. As mentioned in section 4.3 coagulation of an Aitken and accumulation

mode particle results in an accumulation mode particle. Since the growth in number in the accumulation mode is three orders of magnitude smaller than the loss within the Aitken mode, it can be assumed that the increase in mass is mainly caused by coagulation. Furthermore, coagulation within the Aitken mode can also explain the numerical loss, since coagulating particles in the same mode cause a reduction number but no in mass.

6.3 Ash sedimentation

Section 5.3 shows that most of the ash in the insoluble mode is removed within 24 hours after the eruption. Figure 6.2 displays the total ash mass (insoluble and mixed phase) calculated by ICON-ART. The fine ash in the ICON-ART simulation is a modal distribution with a median diameter of 2.4 μm and a standard deviation of 1.8μm. The black dots represent fine Ash (1–12 μm) retrieval results for the Mt. Pinatubo volcanic plume, using AVHRR satellite imagery, done by Guo et al. (2004b). The ash concentrations are calculated by using the Brightness Temperature Difference.

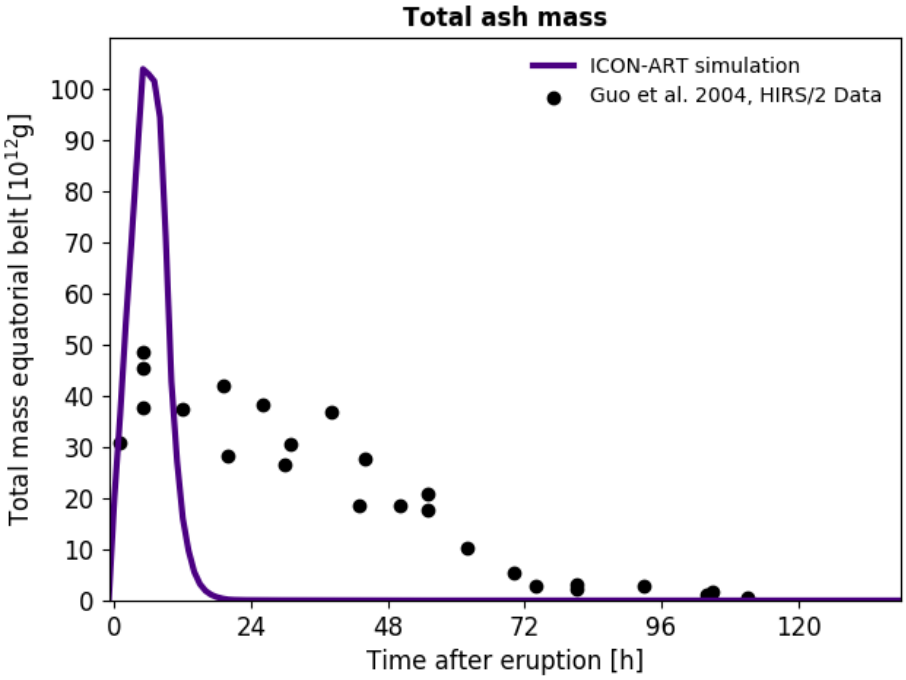

Figure 6.2: Temporal evolution of the total mass of ash. The total ash mass of insoluble and mixed phase ash calculated with ICON-ART within the equatorial belt (35°N and 35°S) is displayed with the solid indigo line. The black dots display the total ash mass according to Guo et al. 2004

Both results are not in good agreement. The ICON-ART simulation reaches values twice as high as the measured ash masses. One problem with the AVHRR satellite imagery is, that during the first 20 hours after the eruption large parts of the ash plumes remain opaque to the satellite. This is caused by the high optical thickness of the plume. Regarding the decay of the ash in the simulation most of the ash is removed within 24 hours after the eruption, but the measurements show still over 1 Tg ash after 100 hours. The

satellite imaging includes particles with 1 μm diameter, that are smaller than the median diameter of the simulation, and therefore it could be the very small particles that make the decay slower.

In the ICON-ART model, the removal of aerosols mainly takes place by washout. The ash is emitted in altitudes between 15 km and 19 km and should be located above the areas where precipitation occurs. Figure 6.3 displays the development of the ash distribution for

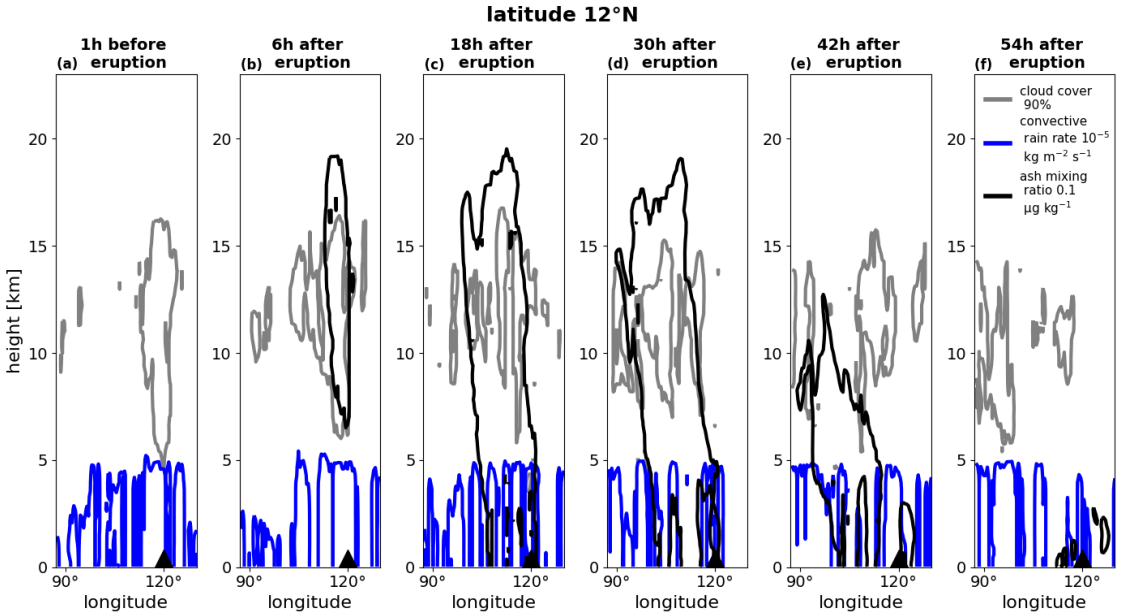

Figure 6.3: Vertical cut at 12°N latitude showing the cloud cover 90% isoline in grey, the rain rate 1×10^{-5} kg m^{-2}s^{-1} in blue and the ash mixing ratio of 0.1 μg g^{-1} in black for different time steps (1 hour before the eruption and 6 hours, 18 hours, 30 hours, 42 hours and 56 hours after the eruption.

different time steps. In plot (b), it is visible that the ash is emitted in a cloudy area. The clouds, that seem to correlate with the ash particles, are offsets of the typhoon Yunya, that passed the Mt. Pinatubo 70 km east. This also explains the heavy rain fall in figure 6.3. The convective rain goes up to 5 km altitude and less than 18 hours after the eruption parts of the ash plume has sunk low enough to get washed out quickly. This explains the fast decay of ash in the simulation. Between 30 and 42 hours after the eruption, a drop of approximately 7 km of the ash can be observed. This shows that, even if the ash is not washed out, it sediments quickly. Fifty-four hours after the eruption ash is only visible in rain free areas below 5 km. Concluding, that the quick decay in the ash mass is caused by fast sedimentation and washout.

The number concentration and median diameter of the insoluble mode indicate, that coagulation leads to a fast aggregation of the ash particles, which accelerates the sedimentation process. The impact of coagulation within the first day after the eruption is displayed in figure 6.4. The upper plot shows the total mass within the equatorial belt. As explained in section 5.3, the total mass of the run with coagulation decreases fast. The run without coagulation decays much slower, with in mean 1.53×10^{11} g per hour. In the run with coagulation the total number reaches a maximum of 4.5×10^{17}, that is two orders of

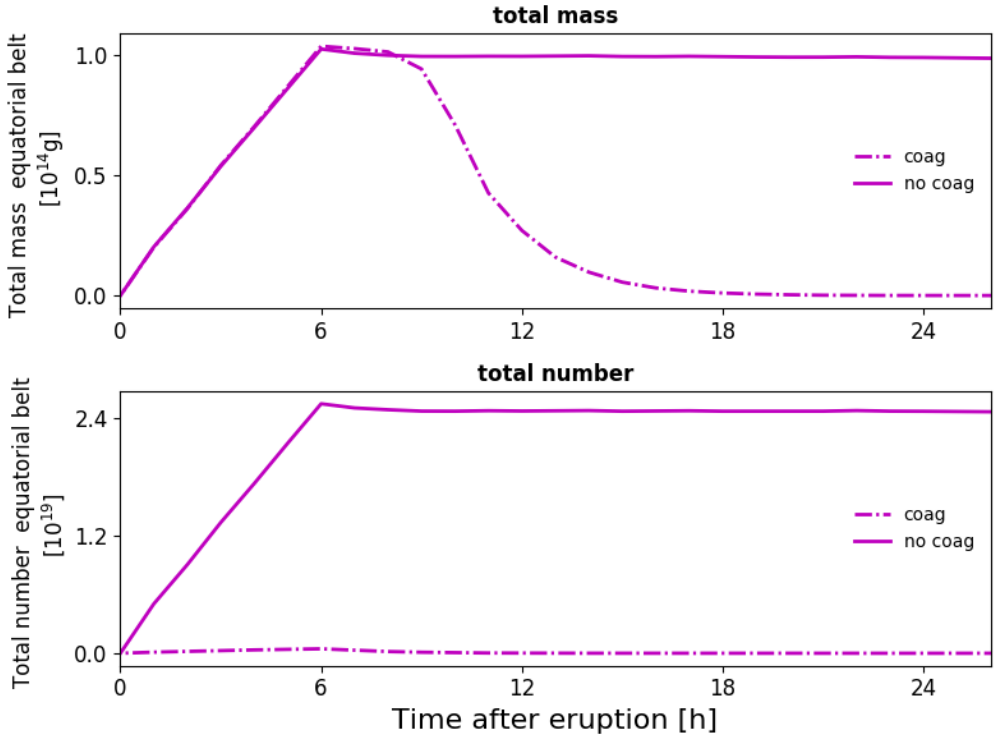

Figure 6.4: Temporal evolution of the total mass (top) and total number (bottom) of insoluble ash within the equatorial belt. The solid line represents the run calculating coagulation and the dashed-dotted line the run without calculating coagulation.

magnitude lower than the run without coagulation (maximum of 2.5×10^{19}). This implies that coagulation has a strong impact. Considering the large amounts of particles that get emitted and then result high concentrations, the probability of colliding particles must be high.

Figure 5.13 shows, that the formation of the mixed ash is limited to the time at which large amounts of insoluble ash are present, while mixed ash can only form through coagulation with or condensation on insoluble ash. Therefore, the quick removal of insoluble ash particles also limits the formation of aged ash, resulting in comparably low concentrations for the mixed ash mode. The lower concentrations in the mixed mode indicate less coagulation and therefore slower particle growth and sedimentation.

6.4 Increased particle formation and aggregation in case RAD

As analysed in section 5.3, the simulation calculating the aerosol radiative effects shows increased particle formation and aggregation compared to case REF. Not only in the SO_4 Aitken mode, which outlines enhanced nucleation, but also in the SO_4 accumulation and mixed ash mode, which indicates enhanced condensation and/or coagulation. In the model nucleation only depends on the temperature and the relative humidity as shown in equation 4.20. With a rising relative humidity the critical concentration sinks, meaning, that more H_2SO_4 can condensate. Whereas with a rising temperature the critical concentration also

increases. As displayed in figure 5.17, the mean temperature of the eruption plume rises in case RAD, which should result in a decrease in particle formation. Since this is not the case, there must be another dominant effect, that causes supersaturation. The H_2SO_4 concentration, which determines if there is supersaturation and whether nucleation or condensation can take place, is as explained in equation 4.24 produced and limited by the OH concentration, which is furthermore depending on the O_3 concentration and the photolysis rate j_{O_3}.

Figure 6.5 displays the averages of the SO_4 mixing ratio, the temperature, the ozone concentration and the photolysis rate in the area of the eruption plume, nine days after the eruption. To determine, which area is covered by the eruption plume, a threshold of 1 DU of the SO_2 column is chosen. For areas exceeding the threshold, the mean value is calculated in every height level and the mean values below, within and above the plume are displayed in figure 6.5.

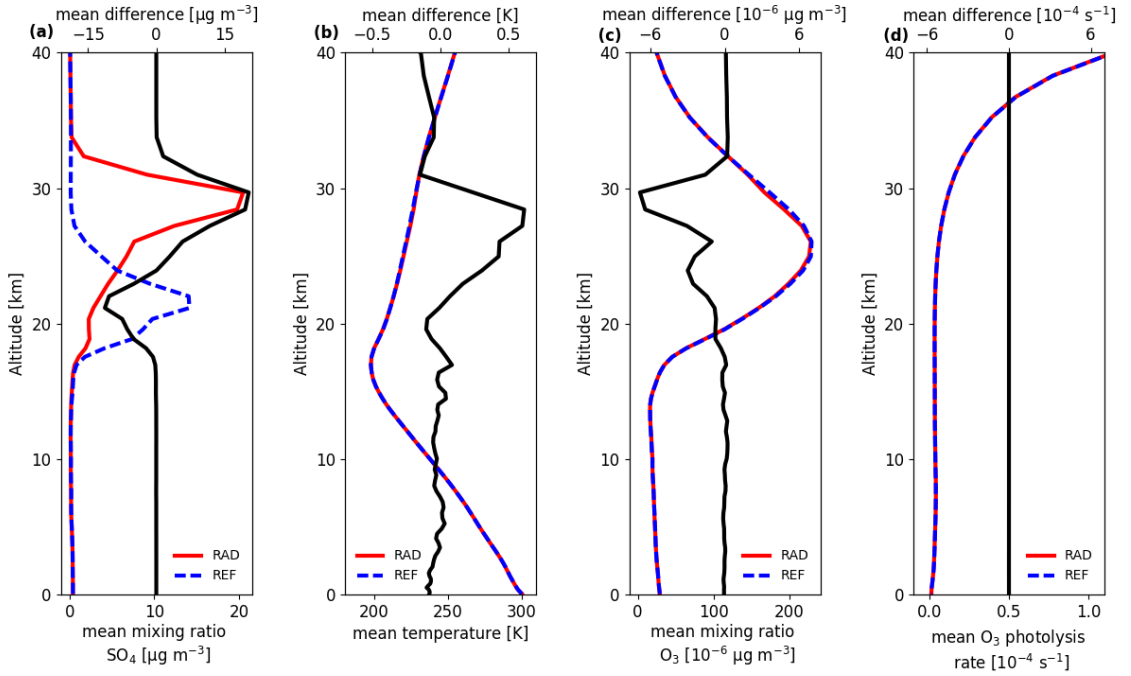

Figure 6.5: Vertical profiles of the mean values in the eruption plume at 06-24-1991, 12:00 UTC. Displayed are the SO_4 soluble mean mixing ratio in μg m^{-3} (Aitken and accumulation mode), mean temperature in Kelvin, O_3 concentration in μg m^{-3} and the O_3 photolysis rate in s^{-1}. The red lines display the result in case RAD, the blue lines case REF and the black lines the difference (RAD-REF).

Figure 6.5 (a) shows the SO_4 profile, case RAD (red line) peaks with a mean mixing ratio of 20.17 μg m^{-3} in a height of 29.7 km. Case REF (blue line) peaks with a mean maximum of 14.42 μg m^{-3} in 21.8 km and is therefore 7.9 km below the peak in case RAD. Further the maximum in case RAD exceeds case REF by 5.75 μg m^{-3}. This outlines once more the uplift and increased particle formation induced by the aerosol radiative effect.

The mean temperature profiles in figure 6.5 (b) show similar shapes in both cases. The mean temperature decreases with height from 300 K at the ground up to the tropopause

with about 198 K. In the stratosphere the temperature increases up to 257 K at 40 km, due to ozone absorption of UV radiation. Regarding the mean difference, the maximum positive difference is at 28.4 km with 0.62 K and the altitudes of increased mean temperature difference correlate with the SO_4 plume concentrations in case RAD. On the ground the mean temperature decreases by 0.89 K.
Figure 6.5 (c) displays the vertical profile of ozone. Again, both runs show a similar trend. The ozone concentration increases from 14.5 km onward and peaks at 26 km with concentrations of 229×10^{-6} μg m^{-3} before decreasing again. The difference between case RAD and case REF is two orders of magnitude lower than the concentrations in the altitudes from 20 km to 32 km. The heights of maximum difference correlate with the SO_4 concentrations. The negative differences imply that the O_3 concentration decreases due to the SO_4 plume in case RAD. Physically, this can be explained by two factors. The first one describes the effective scattering of the sulfur aerosols in the UV regime, which can cause enhanced absorbing by ozone and therefore increase the photolysis. This effect is not calculated in the model. Further the chemical reduction and production of ozone can be affected by the high SO_2 concentrations. The production and reduction of ozone in the stratosphere simplified given in the equations 6.1 to 6.4, where X stands for a catalyst like OH, NO, Cl, Br. Equation 6.1 states, that oxygen is necessary for the building of ozone.

$$3O_2 + h\nu \rightarrow 2O_3 \tag{6.1}$$

$$X + O_3 \rightarrow O_2 + XO \tag{6.2}$$

$$O_3 + h\nu \rightarrow O_2 + O \tag{6.3}$$

$$O + XO \rightarrow XO_2 \tag{6.4}$$

Regarding the production of sulfuric acid as explained in section 2.2, it is shown that oxygen is also necessary for the formation of H_2SO_4. Due to the high SO_2 concentrations it is possible that OH reacts with a sulfur dioxide molecule before O_2 can be photolytically split. Since the difference in mean ozone concentration is two orders of magnitude smaller than the concentration, this seems to be a rather small effect. Taking into account, that lower ozone concentrations would result in lower OH production, this cannot explain the increased particle formation in case RAD.
Figure 6.5 (d) shows the vertical profile of the mean ozone photolysis rate in the eruption plume area. Both runs show again a similar trend. Starting comparably low with values around 4×10^{-6} s^{-1} up to 24 km and then steeply rising to 1.1×10^{-4}s^{-1} in 40 km. The increase with altitude is caused by the dependence of the photolysis rate on the photon flux. The difference between both runs is rather small with less than three orders of magnitude. The direct influence of the volcanic aerosols on the photolysis rate is not considered in the model. The only way, the eruption can influence the photolysis rate is through modification of cloud formation, since the effects of clouds on the photolysis rate are implemented in the model.
The increase of the photolysis rate and the O_3 concentration with height seems to be the

major reason for the increasing particle formation in case RAD, since the volcanic plume rises over time.

Table 6.1: Comparison z_s of the Aitken mode and corresponding O_3 photolysis rate in case RAD and case REF at different times

time [days after eruption]	z_s RAD [km]	z_s REF [km]	mean j_{O_3} RAD [$10^{-6}s^{-1}$]	mean j_{O_3} REF [$10^{-6}s^{-1}$]
1	22.31	21.85	3.73	3.59
2	22.72	22.01	3.96	3.79
3	23.31	22.36	4.18	3.80
4	24.62	22.65	4.97	3.90
5	25.96	22.82	5.88	4.00
6	27.04	23.03	7.24	4.00
7	27.89	23.13	8.60	4.11
8	28.33	22.60	9.39	3.87
9	28.66	22.41	9.84	3.82
10	28.83	22.15	10.30	3.79

Table 6.4 shows the mass weighted height of the Aitken mode and the corresponding mean photolysis rate of this height at different altitudes. With increasing heights in case RAD the photolysis rate also increases. The variations in case REF are rather small (between 1.2 km in height and 0.52×10^{-6} s^{-1} in photolysis rate). After ten days, at the end of the simulation, the mass weighted height in case RAD is highest and the height difference is at its maximum. At this time the difference in photolysis rate is also at its peak. With a value of 10.3×10^{-6} s^{-1} in case RAD, the photolysis rate rose 2.7 times higher than case REF. Taking to account that the O_3 concentrations are high between 20 km and 30 km, one can assume that with rising photolysis rate more OH is produced, leading to more SO_4 particle formation in case RAD.

6.5 Lifting of aerosol plume

Section 5.4 shows the uplift of the aerosol plume induced by aerosol radiative effects. Increased temperatures are one reason for this uplift, as shown in section 5.5. This uplift should also affect the dynamics and therefore be visible in the vertical wind. The mean vertical wind in the eruption plume is calculated in the same way as the mean plume temperature. In this case a threshold of 6×10^{-7} mol mol^{-1} for the SO_2 mixing ratio is chosen. The SO_2 threshold covers the SO_4 plume and even further. The result is displayed in figure 6.6. Both simulations show a 24 h oscillation, correlating with the diurnal cycle, but hardly any trends. In case RAD the mean vertical velocity rises with 0.015 mm s^{-1} per hour and has a mean value of 1.97 mm s^{-1} . In case REF the mean velocity is sinking

with 0.002 mm s^{-1} per hour with a mean value of -0.60 mm s^{-1}. With 0.018 mm s^{-1} per hour the mean difference shows a positive trend. Six days after the eruption the diurnal cycle is clearly visible in the difference, indicating an increased uplift of the eruption plume during the day and a faster sinking during night in case RAD.
Taking the mean velocities into account, the height difference of eruption plumes should not reach more than 1.8 km. Figure 5.14 shows an increase in z_s of more than 6 km. Therefore it seems that increased particle formation in the upper levels strongly contributes to the height difference.

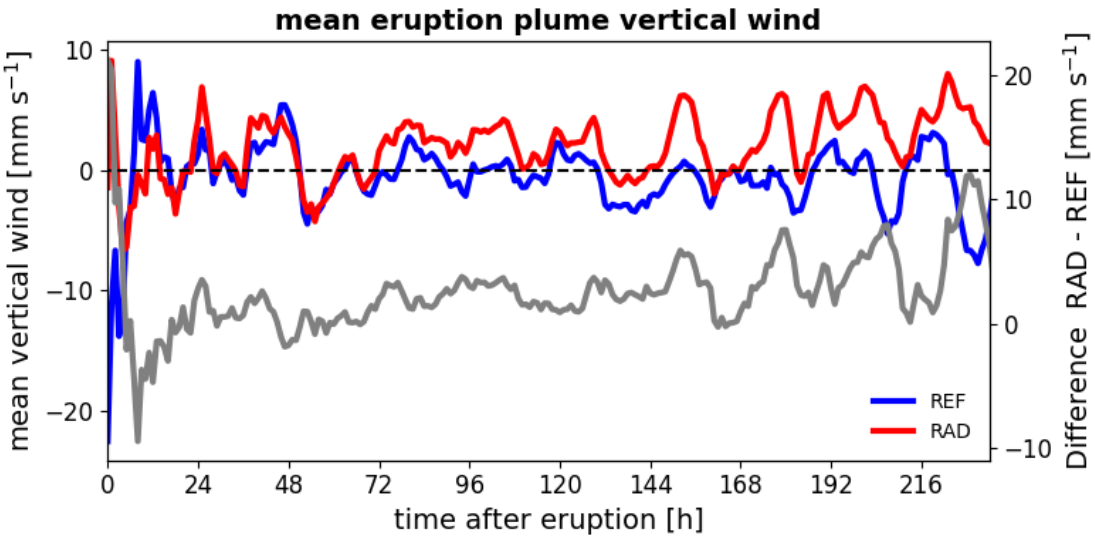

Figure 6.6: Temporal evolution of the mean vertical wind in mm s^{-1} of the SO_2 plume. Case RAD (red line), case REF (blue line) and the difference (RAD-REF) in grey.

6.6 Changes in temperature

This model set up does not include the exit temperature of the volcanic emissions, the temperature changes displayed show only the radiative aerosol effect, but as discussed in section 5.5, this effect influences the temperature. The warming of the aerosol plume in the lower stratosphere is due to absorption of long wave radiation by the sulfur particles and shown in figure 5.16. Above and below the plume the mean temperature decreases. The tropospheric cooling can be explained by two effects. First, the efficient scattering of the sulfur aerosols in the ultraviolet and visible regime, which reduces the amount of UV and VIS radiation reaching the troposphere. Second, the reduction of solar near infrared radiation due to absorption. The aerosols may not absorb efficient in this wavelength regime, nevertheless this effect contributes to the tropospheric cooling according to Ramachandran et al. (2000). The cooling above the plume is a result of the decreased terrestrial longwave radiation. Figure 5.17 shows a decrease of the SO_4 mean temperature after about a day. This could be explained by the ash sedimentation. The absence of ash in the lower and therefore also colder levels allows nucleation. The threshold for the soluble SO_4 plume is then reached in colder environments and contributes to the mean

temperature. This effect is not dominant in the height difference, because there the height was mass weighted, and the concentrations in the lower altitudes should be comparably low.
The further increase after 24 hours after the eruption, which extends to about 20 K towards the end of the simulation, can be explained with the uplift of the plume. The positive vertical temperature gradient in the stratosphere causes an increasing warmer environment with altitude. An uplift of the eruption plume is therefore followed by an increase in temperature. The increase of 20 K is induced by the uplift, and therefore only an indirect aerosol radiative effect. The direct warming is displayed through the grey difference line. The diurnal cycle, visible after five days shows the influence of solar radiation. The warming at daytime can be explained by the solar near infrared, that is partly absorbed by the SO_4 and therefore impacts the temperature within the aerosol plume. The mean increase in difference with time outlines that the effect grows over time and can be explained with the SO_4 concentration, which also increase with time.
The mean plume temperature of ash shows a different temporal profile than sulfur. In the beginning of the simulation the temperature is rising, this can be explained on the one hand, because in this phase the concentration is highest, before spreading. On the other hand is insoluble ash still highly concentrated in the same area and therefore has a strong radiative effect. This also explains the steep decrease after 24 h when most insoluble ash has already been removed. As shown in figure 4.4, ash absorbs solar radiation even more efficiently than SO_4, which explains the diurnal cycle, even if the concentrations are three orders of magnitude lower than in the SO_4 plume.

7 Summary

This thesis examines and quantifies the primary aerosols, secondary particle formations, aged particles and their radiative effects of the Mt. Pinatubo major eruption from 1991 with the numerical model ICON-ART. This study includes the nucleation process of sulfuric acid and the aging of volcanic ash.

First, the simulation is compared to the satellite images by Guo et al. (2004a). For the first five days the satellite images show up to 7.5 times lower maximum concentrations of the SO_2 column but the concentrations narrow towards the end of the simulation. Up to five days the distribution and transport of the simulated SO_2 plume is slower, but afterwards it increases and exceeds the satellite images.

In order to validate the ICON-ART simulation output in terms of secondary particle formation, the results are compared to model studies done by Aquila et al. (2012). This shows that the formation of SO_4 lies within an acceptable range about one week after the eruption and therefore validates the sulfur particle formation process in ICON-ART.

This thesis shows that the formation of ash in the mixed mode is limited to the time in which large amounts of insoluble ash are present. The aged ash has a longer atmospheric lifetime than the insoluble ash, due to smaller concentrations and therefore slower aggregation. The insoluble ash is removed within 24 h after the eruption. This simulation result does not agree with the measurements. The fast removal is caused by coagulation, and therefore aggregation of the particles. This causes the quick sedimentation.

The nucleation of sulfuric acid is increased in areas without pre-existing particles, which in this study mainly ash. The nucleation depends on the diurnal cycle and increases with height, because it is depending on the ozone photolysis. Condensation and coagulation lead to particle growth and result in a shift in the accumulation mode.

This thesis further approached the aerosol radiative effects of volcanic aerosols. To do so, the optical properties of sulfur aerosols and volcanic ash have been implemented in the ICON-ART model. The simulations show a positive long wave net forcing at the top of the atmosphere induced by the SO_4 plume. The aerosols absorb the terrestrial radiation, which causes a warming in the plume and consequently in the lower stratosphere. The shortwave net flux is reduced by the sulfur plume due to effective scattering, causing a negative forcing of up to 200 W m^{-2}. The scattering further increases the shortwave diffuse fluxes. In total, the shortwave effect exceeds the long wave net flux, causing a decrease in temperature at the surface below the eruption plume.

The eruption plume experiences an uplift induced by the aerosol radiative effect. This uplift is also referred to as self-lofting of the plume. Height differences of up to 6.78 km in the mass weighted height of the eruption plume are reached for sulfur aerosols and aged ash. This effect is not solely caused by a dynamic change in vertical wind velocity

but mainly by increased particle formation in the upper levels. In higher levels the photolysis rate increases, more ozone is split and more OH is produced. This increases the sulfuric acid production and therefore makes more condensation and nucleation possible. The uplift of the eruption plume through the aerosol radiative effects causes an increased particle formation in the SO_4 soluble Aitken mode, later resulting in an increase in the accumulation mode and in the aged ash compared to a reference run, without aerosol radiative effects.

Outlook

In this thesis the simulated time frame was ten days, to simulate longer time series and regard the spreading of the aerosol plume, it would be from advantage to implement the Quasi Biennial Oscillation. The QBO is so far not implemented in the ICON model but influences the dynamics of the tropical stratosphere and therefore the spreading of the aerosol plume.
Nucleation and condensation of sulfuric acid plays a key role in this work. The reaction of SO_2 to H_2SO_4 further determines the sulfur particle formation. Therefore the calculated chemistry mechanism is from great importance. In this thesis a simplified OH mechanism is calculated, which is developed for the troposphere, but can be adapted for the lowermost stratosphere. The eruption plume reaches heights up to 30 km and therefore it would be interesting to see how the results differ from a model that calculates an explicit stratospheric chemistry. With the 'Chemistry As A Boxmodel Application/ Module Efficiently Calculating the Chemistry of the Atmosphere' (CAABA/MECCA) it is possible to calculate a comprehensive chemistry mechanism with tropospheric and stratospheric chemistry. MECCA and the infrastructure was integrated to ICON-ART by Jennifer Schröter and will be adapted for volcanic chemistry by Julia Bruckert. This will enable to calculate an explicit stratospheric chemistry with ICON-ART and can outline possible disadvantages of the simplified OH mechanism in the stratosphere.
Further this model setup does not include the aerosol impact on the photolysis rate. According to Jacobson (1998) the scattering of ultraviolet light on aerosol increases the photolysis rate of UV absorbing gases, which should result in an even more increased particle formation. To evaluate this effect could be a topic of future studies.
In this model setup the aerosols do not act as cloud condensation nuclei or ice nuclei. Future studies can focus of the influence of the volcanic aerosols and the cloud and ice formation and analyse resulting changes in radiative fluxed and precipitation.
In this thesis the implemented optical properties for aged ash are consisting of an insoluble core with a fixed soluble cover. This is a reasonable first assumption. Nevertheless the soluble cover can vary with time, due to condensation and coagulation. The size and composition of the cover has a strong impact on the optical properties of the particle. In order to get the best fit for the optical properties statistical analysis of different diameters and different compositions of the cover will be done by Lukas Muser and Dr. Gholamali Hoshyaripour, to improve the optical properties of aged ash.

The fast removal of the insoluble ash is, as discussed, caused by coagulation and the fast aggregation of the ash. Varying the median diameter and emitting not only in the coarse but also in the accumulation mode could counteract the fast removal. A second approach is to adjust the emission profile. Expending the emission vertically and horizontally would decrease the ash concentration within one grid cell and reduce the coagulation probability. According to Textor et al. (2004) water vapor can make out 50% to 90% of a volcanic eruption's volume. In this eruption setup the emitted substances are SO_2 and volcanic ash. Therefore, it would be an interesting aspect to analyse the impact water vapor has on the particle formation and composition and if this influences the radiative effects.

Bibliography

Abbe, C., 1901: The physical basis of long-range weather forecasts. *Monthly Weather Review*, **29 (12)**, 551–561.

Accetta, J. S. and D. L. Shumaker, 2004: *The Infrared and Electro-Optical Systems Handbook Volume 2*. Infrared Information Analysis Center Environmental Research Institude of Michigan, 3–127 pp.

Aquila, V., L. D. Oman, R. S. Stolarski, P. R. Colarco, and P. A. Newman, 2012: Dispersion of the volcanic sulfate cloud from a Mount Pinatubo–like eruption. *Journal of Geophysical Research: Atmospheres*, **117 (D6)**, 6892–6908.

Bautista, C. B., 1996: The Mount Pinatubo disaster and the people of Central Luzon. *Fire and mud: Eruptions and lahars of Mount Pinatubo, Philippines*, 151–161.

Bjerknes, V., 1904: Das Problem der Wettervorhersage, betrachtet vom Standpunkten der Mechanik und der Physik. *Meteor. Z.*, **21**, 1–7.

Bluth, G. J., S. D. Doiron, C. C. Schnetzler, A. J. Krueger, and L. S. Walter, 1992: Global tracking of the SO2 clouds from the June, 1991 Mount Pinatubo eruptions. *Geophysical Research Letters*, **19 (2)**, 151–154.

Bolin, B., 1955: Numerical Forecasting with the Barotropic Model 1. *Tellus*, **7 (1)**, 27–49.

Charney, J. G., R. Fjörtoft, and J. Von Neumann, 1990: Numerical integration of the barotropic vorticity equation. *The Atmosphere—A Challenge*, Springer, 267–284.

Cook, K. H. and E. K. Vizy, 2015: Detection and analysis of an amplified warming of the Sahara Desert. *Journal of Climate*, **28 (16)**, 6560–6580.

DeFoor, T. E., E. Robinson, and S. Ryan, 1992: Early lidar observations of the June 1991 Pinatubo eruption plume at Mauna Loa Observatory, Hawaii. *Geophysical research letters*, **19 (2)**, 187–190.

Derimian, Y., O. Dubovik, D. Tanre, P. Goloub, T. Lapyonok, and A. Mortier, 2012: Optical properties and radiative forcing of the Eyjafjallajökull volcanic ash layer observed over Lille, France, in 2010. *Journal of Geophysical Research: Atmospheres*, **117 (D20)**.

Gassmann, A. and H.-J. Herzog, 2007: A consistent time-split numerical scheme applied to the nonhydrostatic compressible equations. *Monthly Weather Review*, **135 (1)**, 20–36.

Goody, R. M. and Y. L. Yung, 1995: *Atmospheric Radiation: Theoretical Basis*. Oxford university press, 288–383 pp.

Graft, H., I. Kirchner, A. Robock, and I. Schult, 1993: Pinatubo eruption winter climate effects: Model versus observations. *Climate Dynamics*, **9 (2)**, 81–93.

Gudmundsson, M. T., R. Pedersen, K. Vogfjörd, B. Thorbjarnardóttir, S. Jakobsdóttir, and M. J. Roberts, 2010: Eruptions of Eyjafjallajökull Volcano, Iceland. *Eos, Transactions American Geophysical Union*, **91 (21)**, 190–191.

Guo, S., G. J. Bluth, W. I. Rose, I. M. Watson, and A. Prata, 2004a: Re-evaluation of SO2 release of the 15 June 1991 Pinatubo eruption using ultraviolet and infrared satellite sensors. *Geochemistry, Geophysics, Geosystems*, **5 (4)**, 1525–2027.

Guo, S., W. I. Rose, G. J. Bluth, and I. M. Watson, 2004b: Particles in the great Pinatubo volcanic cloud of June 1991: The role of ice. *Geochemistry, Geophysics, Geosystems*, **5 (5)**, 1525–2027.

Herzog, M. and H.-F. Graf, 2010: Applying the three-dimensional model ATHAM to volcanic plumes: Dynamic of large co-ignimbrite eruptions and associated injection heights for volcanic gases. *Geophysical Research Letters*, **37 (19)**, L19 807.

Hoblitt, R., 1996: The preclimactic eruptions of Mount Pinatubo, June 1991. *Fire and Mud: Eruptions and lahars of Mount Pinatubo, Philippines*, 457–511.

Jacobson, M. Z., 1998: Studying the effects of aerosols on vertical photolysis rate coefficient and temperature profiles over an urban airshed. *Journal of Geophysical Research: Atmospheres*, **103 (D9)**, 10 593–10 604.

Junge, C. E., C. W. Chagnon, and J. E. Manson, 1961: A world-wide stratospheric aerosol layer. *Science*, **133 (3463)**, 1478–1479.

Kerminen, V.-M. and A. S. Wexler, 1994: Particle formation due to SO2 oxidation and high relative humidity in the remote marine boundary layer. *Journal of Geophysical Research: Atmospheres*, **99 (D12)**, 25 607–25 614.

Kiehl, J. T. and K. E. Trenberth, 1997: Earth's annual global mean energy budget. *Bulletin of the American Meteorological Society*, **78 (2)**, 197–208.

Kirchner, I., G. L. Stenchikov, H.-F. Graf, A. Robock, and J. C. Antuña, 1999: Climate model simulation of winter warming and summer cooling following the 1991 Mount Pinatubo volcanic eruption. *Journal of Geophysical Research: Atmospheres*, **104 (D16)**, 19 039–19 055.

Lee, K. and H. Chen, 1984: Coagulation rate of polydisperse particles. *Aerosol Science and Technology*, **3 (3)**, 327–334.

McCormick, M. P., L. W. Thomason, and C. R. Trepte, 1995: Atmospheric effects of the Mt Pinatubo eruption. *Nature*, **373 (6513)**, 399.

Mlawer, E. J., S. J. Taubman, P. D. Brown, M. J. Iacono, and S. A. Clough, 1997: Radiative transfer for inhomogeneous atmospheres: RRTM, a validated correlated-k

model for the longwave (Paper 97JD00237). *Journal of Geophysical Reasearch*, **102**, 16–663.

Newhall, C. G. and R. S. Punongbayan, 1996: *FIRE and MUD: Eruptions and Lahars of Mount Pinatubo, Philippines*. `https://pubs.usgs.gov/pinatubo/index.html`, last accessed: 31.10.2019.

Newhall, C. G. and S. Self, 1982: The volcanic explosivity index (VEI) an estimate of explosive magnitude for historical volcanism. *Journal of Geophysical Research: Oceans*, **87 (C2)**, 1231–1238.

Niemeier, U., C. Timmreck, H.-F. Graf, S. Kinne, S. Rast, and S. Self, 2009: Initial fate of fine ash and sulfur from large volcanic eruptions. *Atmospheric Chemistry and Physics*, **9 (22)**, 9043–9057.

Orlando, J. J., G. S. Tyndall, and G. P. Brasseur, 1999: *Atmospheric chemistry and global change*. Oxford University Press, 117–154,195–203 pp.

Petty, G. W., 2006: *A first course in atmospheric radiation*. Sundog Pub.

Ramachandran, S., V. Ramaswamy, G. L. Stenchikov, and A. Robock, 2000: Radiative impact of the Mount Pinatubo volcanic eruption: Lower stratospheric response. *Journal of Geophysical Research: Atmospheres*, **105 (D19)**, 24 409–24 429.

Rampino, M. R. and S. Self, 1982: Historic eruptions of Tambora (1815), Krakatau (1883), and Agung (1963), their stratospheric aerosols, and climatic impact. *Quaternary Research*, **18 (2)**, 127–143.

Randles, C., L. Russell, and V. Ramaswamy, 2004: Hygroscopic and optical properties of organic sea salt aerosol and consequences for climate forcing. *Geophysical Research Letters*, **31 (16)**.

Raschendorfer, M., 2001: The new turbulence parameterization of LM. *COSMO newsletter*, **1**, 89–97.

Read, W., L. Froidevaux, and J. Waters, 1993: Microwave limb sounder measurement of stratospheric SO2 from the Mt. Pinatubo Volcano. *Geophysical Research Letters*, **20 (12)**, 1299–1302.

Reinert, D., D. Prill, H. Frank, M. Denhard, and G. Zängl, 2019: Database Reference Manual for ICON and ICON-EPS. *Deutscher Wetterdienst Business Area "Research and Development"*.

Rieger, D., M. Bangert, I. Bischoff-Gauss, J. Förstner, K. Lundgren, D. Reinert, J. Schröter, H. Vogel, G. Zängl, R. Ruhnke, et al., 2015: ICON–ART 1.0–a new online-coupled model system from the global to regional scale. *Geoscientific Model Development*, **8 (6)**, 1659–1676.

Riemer, N., 2002: Numerische Simulationen zur Wirkung des Aerosols auf die troposphärische Chemie und die Sichtweise. Ph.D. thesis, Universität Karlsruhe, Kaiserstraße 12, 76128 Karlsruhe.

Roedel, W., 2013: *Physik unserer Umwelt: Die Atmosphäre*. 219–274,369–400 pp.

Russell, P., J. Livingston, R. Pueschel, J. Bauman, J. Pollack, S. Brooks, P. Hamill, L. Thomason, L. Stowe, T. Deshler, et al., 1996: Global to microscale evolution of the Pinatubo volcanic aerosol derived from diverse measurements and analyses. *Journal of Geophysical Research: Atmospheres*, **101 (D13)**, 18 745–18 763.

Self, S., J.-X. Zhao, R. E. Holasek, R. C. Torres, and A. J. King, 1993: The atmospheric impact of the 1991 Mount Pinatubo eruption.

Sheng, J.-X., F. Arfeuille, B. P. Luo, P. Heckendorn, D. Weisenstein, E. Rozanov, M. Schraner, S. Brönnimann, L. W. Thomason, and T. Peter, 2013: Modeling the stratospheric warming following the Mt. Pinatubo eruption: uncertainties in aerosol extinctions. *Atmospheric Chemistry and Physics*, **13 (22)**, 11 221–11 234.

Sheng, J.-X., D. K. Weisenstein, B.-P. Luo, E. Rozanov, F. Arfeuille, and T. Peter, 2015: A perturbed parameter model ensemble to investigate Mt. Pinatubo's 1991 initial sulfur mass emission. *Atmospheric chemistry and physics*, **15 (20)**, 11 501–11 512.

Shepherd, T. G., I. Polichtchouk, R. J. Hogan, and A. J. Simmons, 2018: Report on Stratosphere Task Force. *European Centre for Medium Range Weather Forecasts, Shinfield Park, Reading, Berkshire RG2 9AX, England.*

Textor, C., H.-F. Graf, C. Timmreck, and A. Robock, 2004: *Emissions from volcanoes*. Springer, 269–303 pp.

Timmreck, C., 2012: Modeling the climatic effects of large explosive volcanic eruptions. *Wiley Interdisciplinary Reviews: Climate Change*, **3 (6)**, 545–564.

Vogel, B., H. Vogel, D. Bäumer, M. Bangert, K. Lundgren, R. Rinke, and T. Stanelle, 2009: The comprehensive model system COSMO-ART–Radiative impact of aerosol on the state of the atmosphere on the regional scale. *Atmospheric Chemistry and Physics*, **9 (22)**, 8661–8680.

Walter, C., 2019: Simulationen der Ausbreitung von Vulkanasche unter expliziter Berücksichtigung der optischen Eigenschaften der Aschepartikel. Ph.D. thesis.

Weimer, M., J. Schröter, J. Eckstein, K. Deetz, M. Neumaier, G. Fischbeck, L. Hu, D. B. Millet, D. Rieger, H. Vogel, et al., 2017: An emission module for ICON-ART 2.0: implementation and simulations of acetone. *Geoscientific Model Development*, **10 (6)**, 2471–2494.

Woods, A. W. and K. Wohletz, 1991: Dimensions and dynamics of co-ignimbrite eruption columns. *Nature*, **350 (6315)**, 225.

Zängl, G., D. Reinert, P. Rípodas, and M. Baldauf, 2015: The ICON (ICOsahedral Non-hydrostatic) modelling framework of DWD and MPI-M: Description of the non-hydrostatic dynamical core. *Quarterly Journal of the Royal Meteorological Society*, **141 (687)**, 563–579.

Danksagung

An dieser Stelle, möchte ich mich gerne meinen Dank aussprechen, an alle die mich bei dieser Arbeit unterstützt haben.
Zuerst möchte ich Herrn Professor Christoph Kottmeier für die Übernahme des Referenten und für die Kritik und Ratschläge danken. Sowie für das Probelesen der Arbeit und das Feedback.
Ebenso möchte ich mich bei Frau Professor Corinna Hoose für die Übernahme der Korreferentenrolle bedanken, so wie für konstruktive Kritik und neue Denkanstöße bei meinem Hauptseminar Vortrag und beim Probelesen der Arbeit.
Mein weiterer Dank geht an meinen Betreuer, Herrn Dr. Bernhard Vogel, für die gute Betreuung und die Aufnahme in seine Arbeitsgruppe und zahlreiche Ratschlage und Diskussionen, die diese Arbeit voran gebracht haben. Eben so wie für das Probelesen der Arbeit.
Ein ganz besonderer Dank geht an die gesamte Arbeitsgruppe „Spurenstoffmodellierung und Klimaprozesse“, die immer offen für Fragen und Diskussionen war und mir mit konsturktiver Kritik sehr geholfen hat.
Hervorheben möchte ich gerne noch Herrn Dr. Ali Hoshyaripour, für die Mie- Rechnungen der Aerosole, ohne die diese Arbeit nicht möglich gewesen wäre und der mir sehr beim Problemen und Fragen zur Seite stand. Vielen Dank!
Weiter möchte ich mich bei Frau Dr. Heike Vogel bedanken, für die Aufbereitung der Initialisierungsdaten aber vor allem für die gute Betreuung und motivierende Gespräche.
Ein großes Dankeschön geht an Lukas Muser, der mir als Ansprechpartner bei Fragen und Problemen immer geholfen hat. Dazu gehörthen neben technischen Problemen auch fachliche Diskussionen, Auswetungsprobleme und Interpretation der Daten.
Bei Sven Werchner möchte ich mich ganz herzlich, für die Hilfe besonders bei technischen Problemen bedanken.
Für das Korrekturlesen möchete ich mich bei meinem Vater Michael Muth und meinem Schwager Martin Habersack bedanken!
Thanks, to my Canadian friend Mike Leger, who took the time to correct my grammar and spelling!
Noch ein besonderer Dank geht an meine Familie, besonders an meine Eltern, die mir das Studium ermöglicht und mich immer unterstützt haben. Auch möchte ich mich herzlich bei meinem Mitbewohnern und Freunden für die schöne Zeit und bedanken und dass sie immer für mich da waren und sind.

Erklärung

Ich versichere wahrheitsgemäß, die Arbeit selbstständig angefertigt, alle benutzten Hilfsmittel vollständig und genau angegeben und alles kenntlich gemacht zu haben, was aus Arbeiten anderer unverändert oder mit Abänderungen entnommen.
Ich versichere wahrheitsgemäß, die Arbeit selbstständig verfasst, alle benutzten Hilfsmittel vollständig und genau angegeben und alles kenntlich gemacht zu haben, was aus Arbeiten anderer unverändert oder mit Abänderungen entnommen wurde sowie die Satzung des KIT zur Sicherung guter wissenschaftlicher Praxis in der jeweils gültigen Fassung beachtet zu haben.

Karlsruhe, den 03. 12. 2019

Name

Appendix

Lookup tables for Mie-calculations

	ash insoluble accumulation mode			ash insoluble coarse mode		
waveband number	EXT	SSA	ASY	EXT	SSA	ASY
1	0.05259	0.04006	0.07560	0.13660	0.47743	0.53160
2	0.10150	0.06169	0.11793	0.15261	0.45472	0.64872
3	0.19431	0.03602	0.13537	0.13696	0.36681	0.74838
4	0.10277	0.08923	0.17575	0.14750	0.52128	0.75548
5	0.11910	0.27222	0.23553	0.17679	0.56743	0.69469
6	0.51961	0.14415	0.17171	0.16921	0.41511	0.78330
7	0.54460	0.10740	0.19280	0.16103	0.40189	0.81618
8	0.32293	0.05327	0.28594	0.13106	0.36723	0.86939
9	0.09055	0.27489	0.39678	0.15017	0.66563	0.88900
10	0.09215	0.39957	0.41799	0.16522	0.71916	0.87300
11	0.16407	0.61227	0.48750	0.18030	0.73765	0.84893
12	0.23015	0.74961	0.53270	0.18447	0.76397	0.82494
13	0.29160	0.77353	0.55838	0.18296	0.75205	0.82388
14	0.32684	0.79408	0.57102	0.18324	0.75175	0.82031
15	0.41156	0.81133	0.59803	0.18130	0.73536	0.82378
16	0.65373	0.70444	0.65298	0.17188	0.60566	0.88148
17	0.65373	0.70444	0.65298	0.17188	0.60566	0.88148
18	0.76660	0.98066	0.66194	0.17242	0.91288	0.73400
19	0.97555	0.98649	0.67549	0.16678	0.92251	0.73960
20	1.18041	0.98804	0.69161	0.16826	0.92039	0.74079
21	1.40476	0.99049	0.70039	0.16364	0.92658	0.75837
22	1.61062	0.99121	0.70707	0.16259	0.92277	0.76940
23	1.67312	0.99125	0.71120	0.16075	0.92170	0.77663
24	1.79298	0.99064	0.69139	0.15459	0.91454	0.79756
25	1.67589	0.98988	0.69478	0.15298	0.91610	0.81412
26	1.60644	0.98669	0.68957	0.15129	0.90148	0.81912
27	1.49926	0.98156	0.71290	0.14943	0.87338	0.83439
28	1.44206	0.96690	0.73915	0.14866	0.81503	0.85476
29	1.43603	0.96146	0.75347	0.14726	0.79107	0.86322
30	0.41156	0.81133	0.59803	0.18130	0.73536	0.82378

	ash mixed accumulation mode			ash mixed coarse mode		
waveband number	EXT	SSA	ASY	EXT	SSA	ASY
1	0.04731	0.00121	0.02033	0.13980	0.44070	0.43815
2	0.08720	0.00219	0.03435	0.18195	0.41573	0.54352
3	0.18097	0.00147	0.03976	0.17791	0.29348	0.63807
4	0.08664	0.00370	0.05253	0.17467	0.48220	0.67138
5	0.07276	0.01553	0.07783	0.24752	0.59125	0.61619
6	0.41004	0.01049	0.05806	0.27436	0.37717	0.64937
7	0.50196	0.00741	0.06094	0.25671	0.35010	0.70029
8	0.34081	0.00334	0.08656	0.18340	0.28690	0.81249
9	0.06058	0.02217	0.13482	0.17857	0.65709	0.84838
10	0.05038	0.03974	0.14586	0.20659	0.73068	0.83660
11	0.05903	0.10533	0.18695	0.27097	0.78002	0.81791
12	0.05723	0.20916	0.22016	0.30053	0.81763	0.79809
13	0.06806	0.25186	0.24072	0.31043	0.80947	0.79584
14	0.07189	0.28820	0.25214	0.31451	0.81319	0.79269
15	0.08792	0.34065	0.27669	0.32047	0.80185	0.79380
16	0.21365	0.26309	0.32117	0.31410	0.67223	0.84011
17	0.21365	0.26309	0.32117	0.31410	0.67223	0.84011
18	0.11732	0.92185	0.37086	0.30629	0.94769	0.71778
19	0.17783	0.95695	0.40449	0.31355	0.95384	0.70060
20	0.26975	0.96946	0.44083	0.30923	0.95300	0.71839
21	0.42464	0.98170	0.48075	0.29940	0.95510	0.71416
22	0.70725	0.98774	0.52533	0.28861	0.95282	0.73644
23	0.85086	0.98920	0.54137	0.29394	0.95254	0.73492
24	1.93800	0.99394	0.60919	0.28390	0.94829	0.74936
25	3.09623	0.99572	0.64623	0.27662	0.94652	0.77653
26	4.70122	0.99619	0.66742	0.26733	0.93797	0.80033
27	6.01615	0.99572	0.68337	0.26428	0.91810	0.80926
28	7.48345	0.99380	0.69213	0.25868	0.87297	0.82814
29	7.89588	0.99278	0.68718	0.25618	0.85401	0.83712
30	0.08792	0.34065	0.27669	0.32047	0.80185	0.79380

	ash giant mode		
waveband number	EXT	SSA	ASY
1	0.09196	0.47706	0.69978
2	0.08886	0.47017	0.80666
3	0.08055	0.45239	0.86242
4	0.08660	0.51921	0.85759
5	0.08265	0.49079	0.85526
6	0.08085	0.47412	0.89361
7	0.07844	0.46897	0.90978
8	0.07462	0.46946	0.90971
9	0.08577	0.60722	0.92811
10	0.08552	0.62725	0.91188
11	0.07874	0.61125	0.90146
12	0.07773	0.63904	0.88755
13	0.07711	0.62906	0.89420
14	0.07705	0.63021	0.89407
15	0.07636	0.61772	0.90232
16	0.07445	0.53426	0.94428
17	0.07445	0.53426	0.94428
18	0.07504	0.83957	0.81511
19	0.07422	0.85418	0.81220
20	0.07310	0.84836	0.81600
21	0.07338	0.85832	0.82369
22	0.07252	0.85347	0.82932
23	0.07114	0.85058	0.83346
24	0.07081	0.84459	0.84748
25	0.06996	0.84246	0.85078
26	0.06923	0.81888	0.85824
27	0.06934	0.77834	0.87292
28	0.06860	0.69958	0.89689
29	0.06856	0.67458	0.90543
30	0.07636	0.61772	0.90232

	SO_4 soluble Aiken mode			SO_4 soluble accumulation mode		
waveband number	EXT	SSA	ASY	EXT	SSA	ASY
1	0.02871	0.00000	0.00004	0.02872	0.00015	0.00056
2	0.01809	0.00002	0.00020	0.01815	0.00148	0.00313
3	0.06639	0.00002	0.00035	0.06673	0.00144	0.00564
4	0.06385	0.00001	0.00044	0.06418	0.00095	0.00706
5	0.04190	0.00004	0.00060	0.04228	0.00279	0.00970
6	0.10976	0.00005	0.00089	0.11113	0.00313	0.01440
7	0.20250	0.00006	0.00117	0.20611	0.00393	0.01905
8	0.39568	0.00004	0.00115	0.40169	0.00245	0.01783
9	0.40459	0.00002	0.00125	0.40688	0.00137	0.01880
10	0.13125	0.00004	0.00170	0.13265	0.00261	0.02563
11	0.13642	0.00013	0.00228	0.13971	0.00775	0.03447
12	0.19499	0.00014	0.00317	0.20027	0.00864	0.04591
13	0.19894	0.00023	0.00400	0.20658	0.01348	0.05672
14	0.21817	0.00029	0.00463	0.22810	0.01665	0.06442
15	0.23121	0.00036	0.00529	0.24350	0.02028	0.07217
16	0.30845	0.00040	0.00702	0.32553	0.02121	0.08948
17	0.30845	0.00040	0.00702	0.32553	0.02121	0.08948
18	0.10585	0.00741	0.01005	0.11875	0.22991	0.12143
19	0.00833	0.06974	0.01492	0.03493	0.74581	0.16762
20	0.00529	0.20538	0.02098	0.05899	0.92057	0.21427
21	0.00373	0.45469	0.02577	0.08270	0.97199	0.24542
22	0.00538	0.92180	0.04151	0.20152	0.99749	0.32461
23	0.01560	0.96070	0.06290	0.45240	0.99870	0.39060
24	0.02586	0.99968	0.08424	0.70334	0.99999	0.45659
25	0.09897	1.00000	0.14913	1.77808	1.00000	0.56569
26	0.24575	1.00000	0.21072	3.06857	1.00000	0.62403
27	0.60659	1.00000	0.28762	5.00644	1.00000	0.66664
28	1.43449	1.00000	0.36437	7.36070	1.00000	0.68228
29	4.08078	1.00000	0.46741	10.25832	1.00000	0.68491
30	0.22117	0.00014	0.00272	0.22676	0.00849	0.03920